Comas, M.C., Zahn, R., Klaus, A., et al., 1996
Proceedings of the Ocean Drilling Program, Initial Reports, Vol. 161

5. SITE 975[1]

Shipboard Scientific Party[2]

HOLE 975A

Date occupied: 0100, 14 May 1995

Date departed: 0730, 14 May 1995

Time on hole: 6 hr, 30 min

Position: 38°53.795′N, 4°30.587′E

Drill pipe measurement from rig floor to seafloor (m): 2427.6

Distance between rig floor and sea level (m): 10.93

Water depth (drill pipe measurement from sea level, m): 2416.7

Total depth (from rig floor, m): 2437.1

Penetration (m): 9.5

Number of cores (including cores having no recovery): 1

Total length of cored section (m): 9.5

Total core recovered (m): 9.92

Core recovery (%): 104.0

Oldest sediment cored:
Depth (mbsf): 9.5
Nature: Clay
Age: Pleistocene

HOLE 975B

Date occupied: 0730, 14 May 1995

Date departed: 0145, 16 May 1995

Time on hole: 1 day, 18 hr, 15 min.

Position: 38°53.786′N, 4°30.596′E

Drill pipe measurement from rig floor to seafloor (m): 2426.4

Distance between rig floor and sea level (m): 10.93

Water depth (drill pipe measurement from sea level, m): 2415.5

Total depth (from rig floor, m): 2743.5

Penetration (m): 317.1

Number of cores (including cores having no recovery): 34

Total length of cored section (m): 317.1

Total core recovered (m): 298.98

Core recovery (%): 94.3

Oldest sediment cored:
Depth (mbsf): 317.1
Nature: Gypsum
Age: late Miocene

HOLE 975C

Date occupied: 0145, 16 May 1995

Date departed: 1015, 18 May 1995

Time on hole: 2 days, 8 hr, 30 min

Position: 38°53.795′N, 4°30.596′E

Drill pipe measurement from rig floor to seafloor (m): 2426.1

Distance between rig floor and sea level (m): 10.99

Water depth (drill pipe measurement from sea level, m): 2415.1

Total depth (from rig floor, m): 2739.8

Penetration (m): 313.7

Number of cores (including cores having no recovery): 34

Total length of cored section (m): 313.7

Total core recovered (m): 307.66

Core recovery (%): 98.1

Oldest sediment cored:
Depth (mbsf): 313.7
Nature: Gypsum
Age: Miocene?

HOLE 975D

Date occupied: 1015, 18 May 1995

Date departed: 0330, 19 May 1995

Time on hole: 17 hr, 15 min.

Position: 38°53.805′N, 4°30.605′E

Drill pipe measurement from rig floor to seafloor (m): 2426.1

Distance between rig floor and sea level (m): 11.02

Water depth (drill pipe measurement from sea level, m): 2415.1

Total depth (from rig floor, m): 2576.0

Penetration (m): 149.9

Number of cores (including cores having no recovery): 16

Total length of cored section (m): 149.9

Total core recovered (m): 157.03

Core recovery (%): 104.8

Oldest sediment cored:
Depth (mbsf): 149.9
Nature: Clay
Age: Pliocene

Principal results: Site 975 is located on the South Balearic Margin between the Balearic Promontory (Menorca and Mallorca Islands) and the Algerian Basin. The site was drilled at the edge of a small basin perched on the east-dipping slope of the Menorca Rise, at 2415 m water depth. Upon ap-

[1] Comas, M.C., Zahn, R., Klaus, A., et al., 1996. *Proc. ODP, Init. Repts.,* 161: College Station, TX (Ocean Drilling Program).

[2] Shipboard Scientific Party is given in the list preceding the Table of Contents.

proaching the site location, seismic reflection was conducted to verify the position of the drilling site.

The primary objective for Site 975 was to retrieve a continuous sedimentary sequence for the Pliocene–Pleistocene on the Menorca Rise. The complete stratigraphic section obtained then could be used to document the history of surface- and deep-water variations in the western Mediterranean. The site is a central tiepoint along the trans-Mediterranean drilling transect that allows us to document environmental conditions in the western Mediterranean during the same times that sapropels formed in the eastern Mediterranean.

Triple APC and double XCB coring were chosen to ensure continuous sediment recovery at Site 975. The two deep XCB holes recovered 317.1 m in Hole 975B and 313.7 m in Hole 975C.

The stratigraphic sequence at Site 975 ranges from uppermost Pleistocene–Holocene (NN21B, MPL6) to uppermost Miocene (NN12, *G. conomiozea* Zone). The sediments contain abundant and well-preserved Pleistocene to lower Pliocene foraminiferal and nannofossil assemblages. Sedimentation rates were 68.28 m/m.y for the Pleistocene–Holocene, 48.9 m/m.y. for the upper Pliocene, and 53.8 m/m.y. for the lower Pliocene. In addition to biostratigraphy, individual cores were correlated between the four holes using magnetic susceptibility, GRAPE, and 550-nm spectrophotometer data.

Sediments at Site 975 have been divided into three lithostratigraphic units:

Unit I (Hole 975A, 0.0–9.5 mbsf; Hole 975B, 0.0–305.2 mbsf; Hole 975C 0.0–306.3 mbsf; Hole 975D, 0.0–149.9 mbsf) consists of Pliocene to Pleistocene nannofossil or calcareous clay, nannofossil or calcareous silty clay, and nannofossil ooze. Carbonate content of these sediments varies between 30% and 70% (average 47%) and increases slightly with depth. The terrigenous sediment fraction includes clay minerals, quartz, and minor amounts of feldspar and accessory minerals. Color banding and bioturbation are common throughout Unit I, but are especially prominent below 150 mbsf. Graded and laminated foraminifer-rich sandy or silty layers were found throughout the unit.

Thirty-eight sapropels of Pleistocene to Pliocene age containing up to 2.8% total organic carbon (TOC) occurred in Unit I. Organic C/N ratios of the sapropels average 12.7, implying that the sapropels likely contain algal material that partially degraded as it settled to the seafloor. Rock-Eval analyses of sapropels selected from Hole 975B suggest that their organic matter consists of a mixture of partially oxidized Type II algal material and Type III land-plant material.

Lithostratigraphic Unit II (Hole 975B, 305.2–307.0 mbsf; Hole 975C, 306.3–306.9 mbsf) consists of Pliocene–Miocene? light-colored carbonate-rich sediments. The major lithologies are finely interlaminated to thinly interbedded gray micrite and greenish gray, micritic silty clay. Rare thin beds of graded calcareous silty sand contain abundant foraminifers and bioclasts. Sedimentary structures and composition strongly suggest an intertidal origin for sediments of Unit II.

Lithostratigraphic Unit III (Hole 975B, 307.0–317.1 mbsf; Hole 975C, 310.7–313.7 mbsf) comprises 4.4 and 1.6 m of late Miocene evaporites at Hole 975B and Hole 975C, respectively. The major lithology is light olive-gray to moderate olive-brown gypsum that occurs as nodular, finely laminated, and coarse crystals in a micrite matrix. The evaporites of Unit III comprise two broad cycles that begin with a clay or micrite-rich clay interval, overlain by thinly bedded gypsiferous chalk.

The sediments of Unit I were deposited in an open-marine environment. The gradual upward decrease in carbonate content may reflect a shift from dominantly hemipelagic to pelagic conditions from the Pliocene to the Pleistocene. The boundary between Unit I and Unit II likely marks the change from a shallow intertidal environment during the uppermost Miocene? to open-marine conditions during the Pliocene. The wavy laminations of the micritic intervals in Unit II are indicative of algal or microbial mat layering. The evaporite sequence of Unit III is consistent with deposition in a supratidal environment. Unit III can be correlated with the top of the Messinian evaporite sequences (just below the "M"-reflector) known elsewhere in the Mediterranean.

Two meter-scale slump folds occur in the upper Pliocene and lower Pleistocene sections (114.5 mbsf and 143 mbsf) in Hole 975B. Slumping may have been related to the gentle east-northeast dip of the entire Neogene and Pleistocene sequence, which is visible in seismic profiles at this location. Steeply dipping conjugate fractures in laminated micritic silty clay and micrite in lithostratigraphic Unit II appear to have been affected by pressure dissolution, producing stylolites. Neither of these features is likely to have any regional tectonic significance. The lack of tectonic deformation and the paucity of slump structures suggest that Site 975 was tectonically inactive during Pliocene–Pleistocene times.

A strong magnetic overprinting made it difficult to determine primary magnetization at Site 975. The magnetic overprint is characterized by high intensities of natural remanent magnetizations (NRM; 50 mA/m), high coercivity, strong positive inclinations close to the present field (60°), and a pervasive radial remagnetization (PRR) that occurs mostly between 40 and 140 mbsf. The distorted magnetic signal correlates to sections containing sapropel layers. This may point to diagenetic effects on the magnetic mineral assemblage, which are possibly associated with organic matter decomposition and concomitant changes in pore-water redox conditions.

Thermal conductivity increases only very slightly with depth, with mean values of 1.25 W/(m·K) at the surface and to 1.5 W/(m·K) at 300 mbsf. *P*-wave velocity also increases with depth from 1.5 km/s at the surface to 1.8 km/s at 300 mbsf. Velocity increases abruptly to 4.8 km/s at 310 mbsf in the evaporitic sequence in the lowest parts of Holes 975B and 975C.

Downhole temperature data were measured at five depths in Hole 975C and were combined with thermal conductivity data, indicating a heat flow of 81 mW/m^2.

Interstitial water profiles are strongly influenced by the presence of the evaporitic sequence at the base of Site 975. Interstitial calcium and sulfate profiles both exhibit a gentle decrease from just below the sediment/water interface to 46.55 mbsf, and both then increase to near-linear gradients toward the base of the hole. Dissolution of gypsum in the Messinian evaporites provides a source for the calcium and sulfate and explains why sulfate depletion does not occur at this site, even though bacterial sulfate reduction is the main diagenetic process. The sulfate gradient suggests that organic matter degradation below 5.55 mbsf occurs mainly by sulfate reduction. Between the sediment/water interface and 5.55 mbsf, organic matter degradation occurs by aerobic degradation and manganese reduction, as evidenced by the manganese mobilization peak at 5.55 mbsf. Calcium and, particularly, strontium may also originate from interactions of Messinian brines with biogenic carbonates. High interstitial lithium concentrations suggest the presence of late-stage brines in the evaporites.

Samples containing at least 1% TOC were selected from Hole 975B for extraction and analysis of long-chain alkenone biomarkers and calculation of sea-surface paleotemperatures. Sea-surface paleotemperatures have fluctuated over a 7°C range in the Balearic Sea during the Pleistocene. The sea-surface temperatures during the Pleistocene varied between 16° and 23°C, and are consistently about 2°C cooler than those estimated at times of sapropel deposition in the eastern Mediterranean, as determined during Leg 160.

Hole 975C was logged between 42.0 and 309.0 mbsf using the quad combo, Formation MicroScanner (FMS), and geochemical tool strings. The resistivity profile is very homogeneous throughout the section with values increasing from 0.7 Ωm at the top of the hole to 1.0 Ωm at the bottom. Caliper data from the quad combo and the FMS show erratic variations in hole diameter from 150 mbsf downward, when drilling was switched from APC to XCB coring.

Two major results were achieved at Site 975. First, 38 sapropel layers were recovered at this site. Site 975 thus extends the geographic limit of documented sapropel occurrence further west, from the Tyrrhenian Sea to the central western Mediterranean basin. Discovery of sapropels at Site 975 warrants revision of the paleoceanographic concepts that relate the formation of sapropels to paleoceanographic changes in the eastern Mediterranean. Second, a well-preserved sequence of uppermost Messinian evaporites and early Pliocene hemipelagic to pelagic sediments has been retrieved in two holes at Site 975. The high-quality XCB cores will make it possible to study in detail the environmental transition from restricted to open-marine conditions during late Miocene–early Pliocene times.

BACKGROUND AND OBJECTIVES

Site 975 is located on the Menorca Rise between the Balearic Promontory (Menorca and Mallorca Islands) and the South Balearic-Algerian Basin (Fig. 1). The site was drilled at the edge of a small basin perched on the east-dipping slope of the Menorca Rise, at 2415 m water depth (Fig. 2). The site was selected on the basis of seismic data collected in 1984 by the *Bannock* (Cruise BAL-84; Curzi et al., 1985). Site 975 was positioned at the intersection of the *Bannock* line Bal-9 and the two single-channel seismic profiles acquired by the *JOIDES Resolution* (Fig. 3).

The South Balearic Basin comprises a narrow abyssal plain which links the Alboran Sea with the Algerian Basin. It is underlain by an oceanic crust, which thins toward the Balearic Rise. Toward the Eastern Alboran Basin to the west, the oceanic crust gives way to a thin continental crust. The abyssal plain around the Balearic Margin contains the "Lower" and "Upper" Messinian evaporite sequences (Hsü, Montadert, et al., 1978). These sequences pinch out on the northern and southern margins of the basin, disappearing toward the Alboran Basin to the west.

Previous DSDP drilling on the Balearic Rise (Legs 13 and 43) was designed to yield information on the depositional history and paleobiogeography of the Messinian and pre-Messinian sediments, as well as to determine the age and subsidence history of the Balearic and Algerian Basins (Ryan, Hsü, et al., 1973; Hsü, Montadert, et al., 1978). DSDP Site 124 was positioned in a small basin on the western flank of a presumed buried basement ridge on the Balearic Rise (Fig. 1). The sedimentary sequence cored at Site 124 consisted of 365 m of Pliocene–Pleistocene sediments. However, this sequence was not continuously cored because significant terrigenous input was expected to hamper stratigraphic work in the upper sediment column. About 57 m of upper Miocene evaporitic beds, including dolomite, gypsum, and anhydrite layers, were cored farther down before penetration became impossible due to drill-bit failure in solid anhydrites. Thus, although Site 124 drilling failed to reach acoustic basement, it confirmed that the seismic reflector called "Horizon M" corresponds to the unconformable contact between upper Miocene evaporites and lower Pliocene pelagic sediments (Shipboard Scientific Party, 1973).

DSDP Site 372 was drilled on the eastern Balearic Margin (Fig. 1), where the acoustic basement is faulted from pre-Miocene rifting and is overlain by Miocene sediments (Mauffret et al., 1978). Site 372 penetrated 150 m of Pliocene–Pleistocene sediments before upper Miocene gypsum and dolomitic nannofossil marls were reached. Again, the upper sediment column was not continuously cored because the primary target was to reach pre-evaporitic sediments. As at Site 124, Site 372 failed to reach acoustic basement because of drill-bit failure. However, on the basis of sedimentation rates, an extrapolated age of earliest Miocene to Oligocene was obtained for the earliest sediments deposited on the Menorca Rise (Hsü, Montadert, et al., 1978).

The primary objective for Site 975 was to continuously core the Pliocene–Pleistocene sedimentary sequence to obtain a complete stratigraphic section that would allow us to document the history of surface- and deep-water variation in the western Mediterranean. To achieve this goal, the site was positioned in a small sub-basin on the Menorca continental rise, which was expected to be both filled with ponded sediments and depleted of sandy turbidites. Initial inspection of a 9-m-long gravity core, taken during our pre-site survey at the position of Site 975, showed no major signs of disturbance, supporting our contention that the proposed drill site was indeed suitable for conducting high-resolution paleoceanographic work.

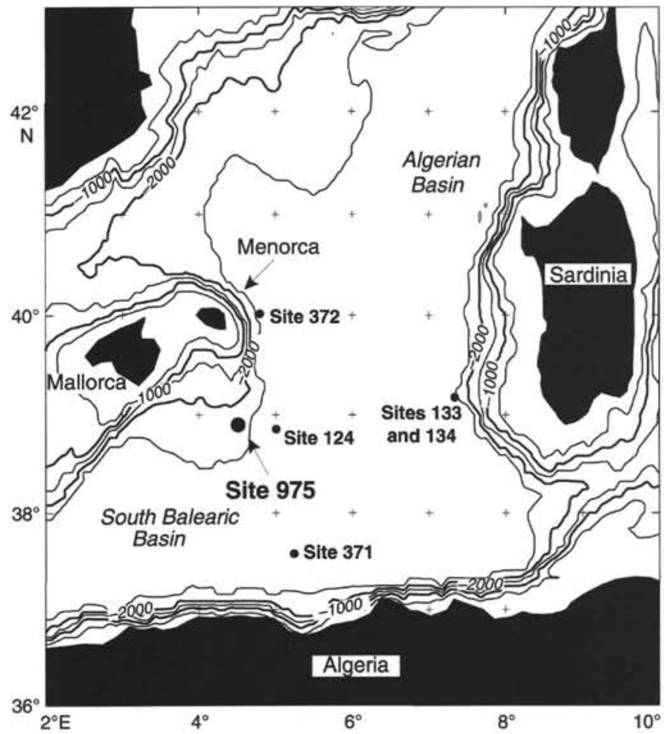

Figure 1. Location of ODP Site 975 and previously drilled DSDP sites on the South Balearic Margin.

Site 975 is in a key position to monitor the history of inflowing Atlantic waters as they flow to the east, and of outflowing Mediterranean waters on their way west to the Alboran Sea. As such, it is a central tiepoint along the trans-Mediterranean drilling transect that will allow us to correlate environmental conditions during times of sapropel formation in the eastern Mediterranean with conditions in the western Mediterranean during the same time intervals. The intended total penetration was 350 mbsf at Site 975, thought to be the depth of the "M"-reflector, which the earlier DSDP drilling results have shown to mark the top of the Messinian (Fig. 3).

OPERATIONS

Transit, Site 974 to Site 975 (MedSap-6A)

The 380-nmi sea voyage to Site 975 required 47 hr at an average speed of 8.1 nmi/hr. We conducted a pre-site seismic survey over Site 975 that lasted about 6 hr. We deployed a beacon at 38°15.612′N, 4°44.990′E on 0100 hr, May 14. Deployment of a second beacon was at 0300 hr, May 14. The elevation of the DES above sea level was 10.93 m for Holes 975A and 974B, 10.99 m for Hole 975C, and 11.02 m for Hole 974D.

Hole 975A

We spudded Hole 975A at 0700 hr, May 14, at 38°53.795N, 04°30.587 E. The bit was positioned at 2428.0 mbrf and Core 975A-1H recovered 9.92 m (104.4% recovery; Table 1; see also detailed coring summary on the CD-ROM, back pocket, this volume). Be-

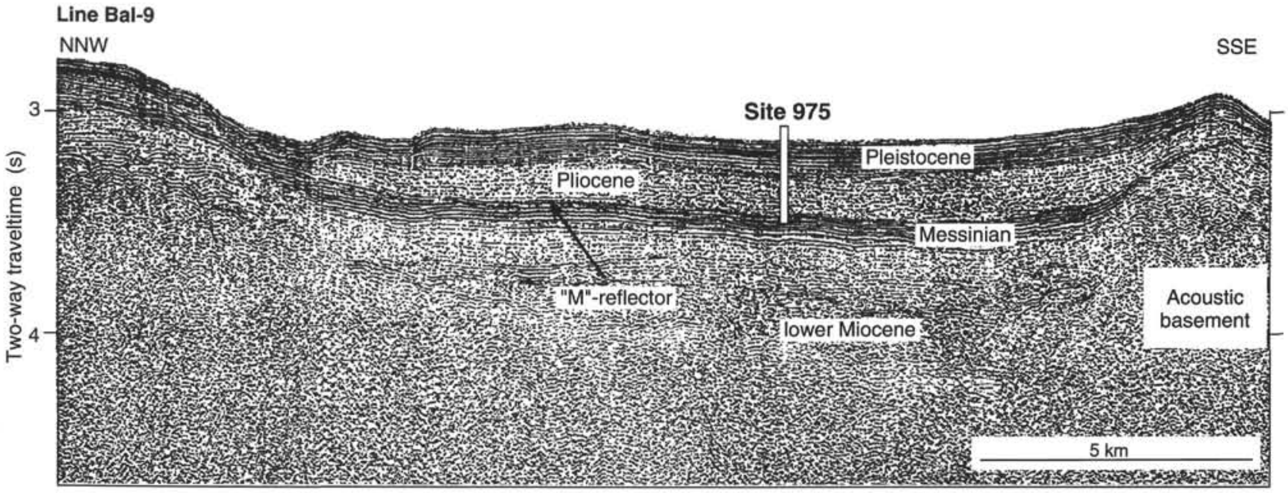

Figure 2. Single-channel seismic profile Bal-9 across the southern flank of the Menorca Rise (Curzi et al., 1985). Site 975 was designed to penetrate through the Pliocene–Pleistocene sediments to the depth of the Messinian "M"-reflector. Two seismic lines crossing the site were shot to refine the position of Site 975 (see Fig. 3).

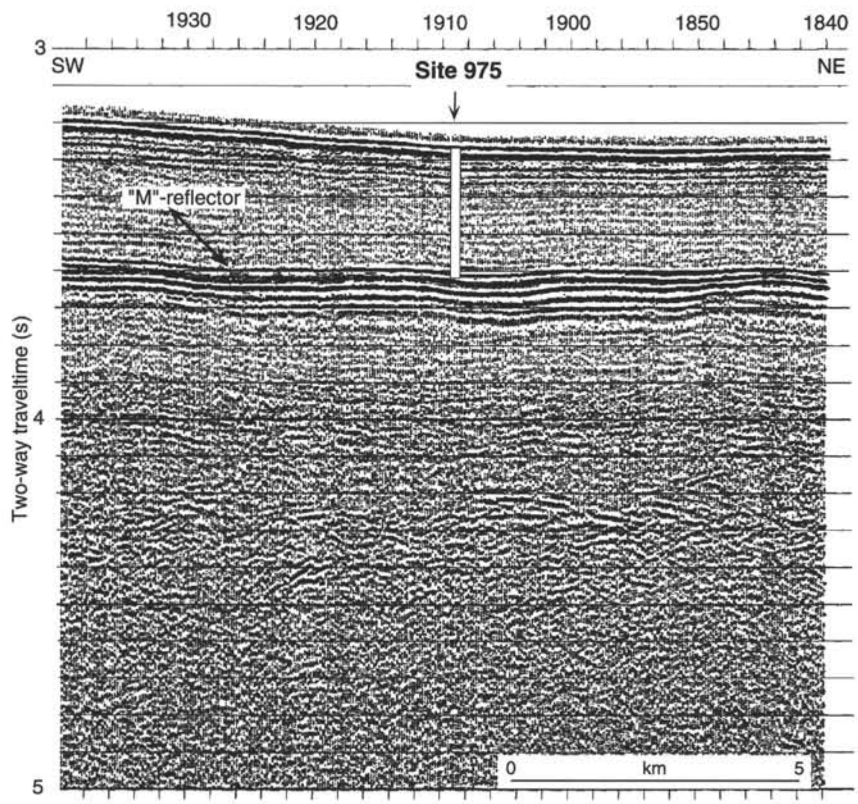

Figure 3. Single-channel seismic profile that was shot while approaching the site (80-in^3 air gun source). The acoustic "M"-reflector was reached at a sub-bottom depth of 305.2 mbsf and 306.3 mbsf in Holes 975B and 975C, respectively.

cause this core overshot the mudline, an exact seafloor depth could not be calculated, and the hole was terminated. The bit cleared the seafloor at 0730 hr, May 14.

Hole 975B

We raised the bit 7 m to 2421.0 mbrf and spudded Hole 975B at 0745 hr, May 14. Core 975B-1H recovered 4.1 m of sediment; therefore, the seafloor was defined to be at 2416 mbsl. Cores 1H to 16H were taken to 2573 m (146.6 mbsf) and recovered 151.68 m (103% recovery). Cores 3H through 16H were oriented using the Tensor tool. While retrieving Core 6H, the sandline broke before the core was brought onto the rig floor. The core barrel was dropped twice during attempts to fish it and the sandline from inside the drill pipe. After the core was recovered and split, it was noted that the lower section of this core was disturbed. In addition, Core 7H also had some disturbance caused by Core 6H penetrating the top of Core 7H, as well as from the additional drill pipe motion during the 6 hr that Core 6H was being retrieved.

Cores 14H to 16H were partial strokes even though the cores were full when recovered. After an overpull of 60,000 lb was recorded for Core 16H, we switched to XCB coring. Cores 17X to 34X were taken

Table 1. Site 975 coring summary.

Core	Date (May 1995)	Time (UTC)	Depth (mbsf)	Length cored (m)	Length recovered (m)	Recovery (%)
161-975A-						
1H	14	0515	0.0–9.5	9.5	9.92	104.0
Coring totals:				9.5	9.92	104.0
161-975B-						
1H	14	0600	0.0–4.1	4.1	4.16	101.0
2H	14	0640	4.1–13.6	9.5	9.98	105.0
3H	14	0730	13.6–23.1	9.5	9.84	103.0
4H	14	0810	23.1–32.6	9.5	9.65	101.0
5H	14	0850	32.6–42.1	9.5	9.99	105.0
6H	14	1530	42.1–51.6	9.5	9.83	103.0
7H	14	1700	51.6–61.1	9.5	8.37	88.1
8H	14	1800	61.1–70.6	9.5	9.81	103.0
9H	14	1840	70.6–80.1	9.5	9.96	105.0
10H	14	1920	80.1–89.6	9.5	9.81	103.0
11H	14	2010	89.6–99.1	9.5	10.13	106.6
12H	14	2100	99.1–108.6	9.5	9.75	102.0
13H	14	2150	108.6–118.1	9.5	10.06	105.9
14H	14	2240	118.1–127.6	9.5	10.12	106.5
15H	14	2330	127.6–137.1	9.5	10.15	106.8
16H	15	0030	137.1–146.6	9.5	10.06	105.9
17X	15	0200	146.6–156.3	9.7	5.75	59.3
18X	15	0245	156.3–166.3	10.0	9.63	96.3
19X	15	0350	166.3–176.4	10.1	4.98	49.3
20X	15	0440	176.4–186.4	10.0	0.05	0.5
21X	15	0540	186.4–196.2	9.8	9.80	100.0
22X	15	0620	196.2–206.2	10.0	9.86	98.6
23X	15	0710	206.2–215.9	9.7	9.89	102.0
24X	15	0800	215.9–225.4	9.5	9.82	103.0
25X	15	0850	225.4–235.1	9.7	9.84	101.0
26X	15	0940	235.1–244.8	9.7	9.87	102.0
27X	15	1100	244.8–254.5	9.7	9.26	95.4
28X	15	1220	254.5–264.1	9.6	9.81	102.0
29X	15	1320	264.1–273.6	9.5	9.93	104.0
30X	15	1425	273.6–283.3	9.7	9.91	102.0
31X	15	1530	283.3–292.8	9.5	9.97	105.0
32X	15	1630	292.8–302.4	9.6	9.95	103.0
33X	15	1900	302.4–310.0	7.6	4.86	63.9
34X	15	2230	310.0–317.1	7.1	4.13	58.1
Coring totals:				317.1	298.98	94.3
161-975C-						
1H	16	0055	0.0–2.4	2.4	2.43	101.0
2H	16	0130	2.4–11.9	9.5	10.02	105.5
3H	16	0220	11.9–21.4	9.5	9.52	100.0
4H	16	0300	21.4–30.9	9.5	10.00	105.2
5H	16	0330	30.9–40.4	9.5	9.89	104.0
6H	16	0430	40.4–49.9	9.5	10.02	105.5
7H	16	0500	49.9–59.4	9.5	9.98	105.0
8H	16	0535	59.4–68.9	9.5	9.91	104.0
9H	16	0625	68.9–78.4	9.5	10.26	108.0
10H	16	0700	78.4–87.9	9.5	9.87	104.0
11H	16	0735	87.9–97.4	9.5	10.11	106.4
12H	16	0830	97.4–106.9	9.5	10.09	106.2
13H	16	0905	106.9–116.4	9.5	10.20	107.3
14H	16	0945	116.4–125.9	9.5	9.91	104.0
15H	16	1040	125.9–135.4	9.5	10.17	107.0
16H	16	1120	135.4–144.9	9.5	10.16	106.9
17X	16	1310	144.9–154.4	9.5	9.82	103.0
18X	16	1415	154.4–164.1	9.7	9.82	101.0
19X	16	1520	164.1–173.7	9.6	9.89	103.0
20X	16	1630	173.7–183.4	9.7	9.82	101.0
21X	16	1745	183.4–192.9	9.5	9.77	103.0
22X	16	1845	192.9–202.5	9.6	9.79	102.0
23X	16	1945	202.5–212.2	9.7	9.92	102.0
24X	16	2030	212.2–221.7	9.5	9.84	103.0
25X	16	2130	221.7–231.4	9.7	9.90	102.0
26X	16	2220	231.4–241.0	9.6	9.39	97.8
27X	16	2320	241.0–251.0	10.0	9.79	97.9
28X	17	0020	251.0–261.0	10.0	9.94	99.4
29X	17	0125	261.0–270.9	9.9	0.15	1.5
30X	17	0225	270.9–280.8	9.9	9.73	98.3
31X	17	0320	280.8–290.8	10.0	10.01	100.1
32X	17	0415	290.8–300.7	9.9	9.69	97.9
33X	17	0620	300.7–310.7	10.0	6.17	61.7
34X	17	0845	310.7–313.7	3.0	1.68	56.0
Coring totals:				313.7	307.66	98.1
161-975D-						
1H	18	0925	0.0–7.4	7.4	7.41	100.0
2H	18	1015	7.4–16.9	9.5	9.82	103.0
3H	18	1050	16.9–26.4	9.5	9.70	102.0
4H	18	1125	26.4–35.9	9.5	9.67	102.0
5H	18	1200	35.9–45.4	9.5	9.79	103.0
6H	18	1240	45.4–54.9	9.5	9.75	102.0
7H	18	1315	54.9–64.4	9.5	10.04	105.7
8H	18	1350	64.4–73.9	9.5	10.10	106.3
9H	18	1430	73.9–83.4	9.5	10.09	106.2
10H	18	1510	83.4–92.9	9.5	10.03	105.6
11H	18	1600	92.9–102.4	9.5	10.17	107.0
12H	18	1645	102.4–111.9	9.5	10.06	105.9
13H	18	1730	111.9–121.4	9.5	10.10	106.3
14H	18	1815	121.4–130.9	9.5	10.16	106.9
15H	18	1900	130.9–140.4	9.5	10.08	106.1
16H	18	1945	140.4–149.9	9.5	10.06	105.9
Coring totals:				149.9	157.03	104.8

Note: See also detailed coring summary on the CD-ROM, back pocket, this volume.

from 146.6 to 317.1 mbsf. We cored 170.5 m with the XCB and recovered 147.3 m (86%). Several of the first few XCB cores (17X, 19X, and 20X) had lower recoveries. The total APC/XCB recovery in Hole 975B was 94%.

A hard layer was encountered at about 307.5 mbsf (2734 mbrf). This layer appears to correlate with a strong reflector in the seismic reflection data collected just prior to drilling at this location. Previous velocity analyses suggested that this reflector ("M"-reflector) was at a depth of 350 mbsf. Hole 975B was terminated after advancing to 317.1 mbsf (about 9.6 m into the hard gypsum material) to abide by Pollution Prevention and Safety Panel recommendations.

Hole 975C

We offset the ship 20 m to the north-northeast and spudded Hole 975C at 0230 hr on 16 May. Core 975C-1H recovered 2.43 m of sediment with the bit position at 2419.0 m; therefore, the seafloor was defined to be at 2415 mbsl. Cores 1H through 16H were taken to 2571 m (144.9 mbsf) and recovered 152.54 m (104% recovery). ADARA temperature measurements were made while taking Cores 3H, 6H, 9H, 12H, and 15H). Cores 14H through 16H were recorded as partial cores with overpull exceeding 45,000 lb.

Cores 17X through 34X were cut from 144.9 to 313.7 mbsf and recovered 155.12 m (92% recovery). The hard gypsum "M"-reflector was encountered at 2735.1 m (309 mbsf). Total APC/XCB recovery for Hole 975C was 307.66 m (98%).

We then conditioned the hole for logging with a short wiper trip. No drag was observed and only 7 m of fill were encountered in the bottom of the hole, indicating good hole conditions for logging. The hole was displaced with seawater. The bit was positioned at 2497.53 m (71.43 mbsf) to log and was raised approximately 20 m more just before the logging tools reentered the drill pipe, so that more of the upper portion of the borehole could be logged. Three tool strings were run in the following order: (1) quad combo, (2) FMS, and (3) geochemical. The logs were run to 2735, 2730, and 2723 mbrf, respectively. No significant operational or hole stability problems were reported by the logger. The log data indicated hole deviations <2°. There was a noticeable difference in hole diameters between the APC and XCB portions of the hole. Logging was finished at 1000 hr, May 18, and the bit cleared the seafloor at 1015 hr, May 18.

Hole 975D

We offset the ship 20 m north-northeast and spudded Hole 975D with the bit at 2424.0 mbrf at 1045, May 18. Core 975D-1H recovered 7.4 m of sediment; therefore, the seafloor was defined to be at 2415 mbsl. Cores 1H to 16H were taken to 149.9 mbsf and recovered 157.13 m (105% recovery). Cores 11H, 12H, and 16H were partial strokes with up to 50,000 lb overpull. The bit cleared the seafloor at 2245 hr, 18 May, and the BHA was secured for the transit to Site Alb-2 (Site 976) at 0330 hr, May 19. The 11-7/16-in security bit (S/N 478458) had negligible tooth wear, and the bearings were still in good shape despite having been used for 37.7 hr.

LITHOSTRATIGRAPHY

Four holes were drilled at Site 975 on the Menorca Rise, providing a complete stratigraphic section to a maximum depth of 317.1 mbsf in Hole 975B. Sediments at Site 975 have been divided into three lithostratigraphic units (Fig. 4, Table 2) based on downhole changes in composition and sedimentary structures.

Description of Lithostratigraphic Units

Unit I

Hole 975A, Core 975A-1H, 0–9.5 mbsf;
Hole 975B, Core 975B-1H through Section 33X-2, 131 cm, 0–305.2 mbsf;
Hole 975C, Core 975C-1H through Section 33X-4, 110 cm, 0–306.3 mbsf;
Hole 975D, Cores 975D-1H through 16H, 0–149.9 mbsf.

Lithostratigraphic Unit I consists of Pliocene to Pleistocene nannofossil or calcareous clay (~60% of the section), nannofossil or calcareous silty clay (~20%), and nannofossil ooze (~20%). The carbonate content of these sediments, as determined by coulometric analysis (see "Geochemistry" section, this chapter), generally ranges between 30% and 70% (average 47%) and slightly increases with depth (Fig. 4). Smear-slide analysis indicates that nannofossils are the major component of the carbonate fraction, although locally foraminifers and micrite may each compose up to 30% of the sediment. A few percent of silt- to fine-sand-sized foraminifers, many of which are filled with an opaque mineral (pyrite?), are dispersed throughout the sediment. In sediments from below about 240 mbsf in Unit I, the foraminifer content generally ranges from 10% to 30%. The terrigenous fraction of Unit I includes clay minerals (illite, kaolinite or chlorite, and smectite), quartz, and minor amounts of feldspar and accessory minerals. The predominant colors of Unit I sediments are olive gray and light olive gray; lighter shades tend to correlate with higher carbonate content. Color banding is common; the range of colors observed is given in Table 3.

Bioturbation is common throughout Unit I sediments (Figs. 5, 6), but is especially prominent at depths greater than 150 mbsf. Trace fossils identified include *Chondrites, Planolites, Zoophycos,* and *Arenicolites*(?). Burrow fill is generally siltier than surrounding sediment and is commonly pyritized, giving the sediment a mottled appearance.

Cyclic alternations of lighter (pale olive to light olive gray) nannofossil clay to nannofossil ooze, and darker (light olive gray) nannofossil clay, were noted in Unit I (Fig. 7). Where not bioturbated, darker intervals have sharp lower boundaries, but there is no noticeable grain-size change across these boundaries. In all cases, the upper boundaries of the darker intervals are bioturbated. In many examples, bioturbation extends through the entire darker interval. The bases of a few lighter intervals contain more silt- or sand-sized grains (primarily foraminifers) than either the underlying darker interval or the remainder of the lighter interval. These cycles vary in thickness on a centimeter to meter scale. They are evident throughout Unit I, but the increase in bioturbation at depths greater than about 150 mbsf, plus the overall increase in carbonate content, make recognition of apparent cyclicity more difficult with depth.

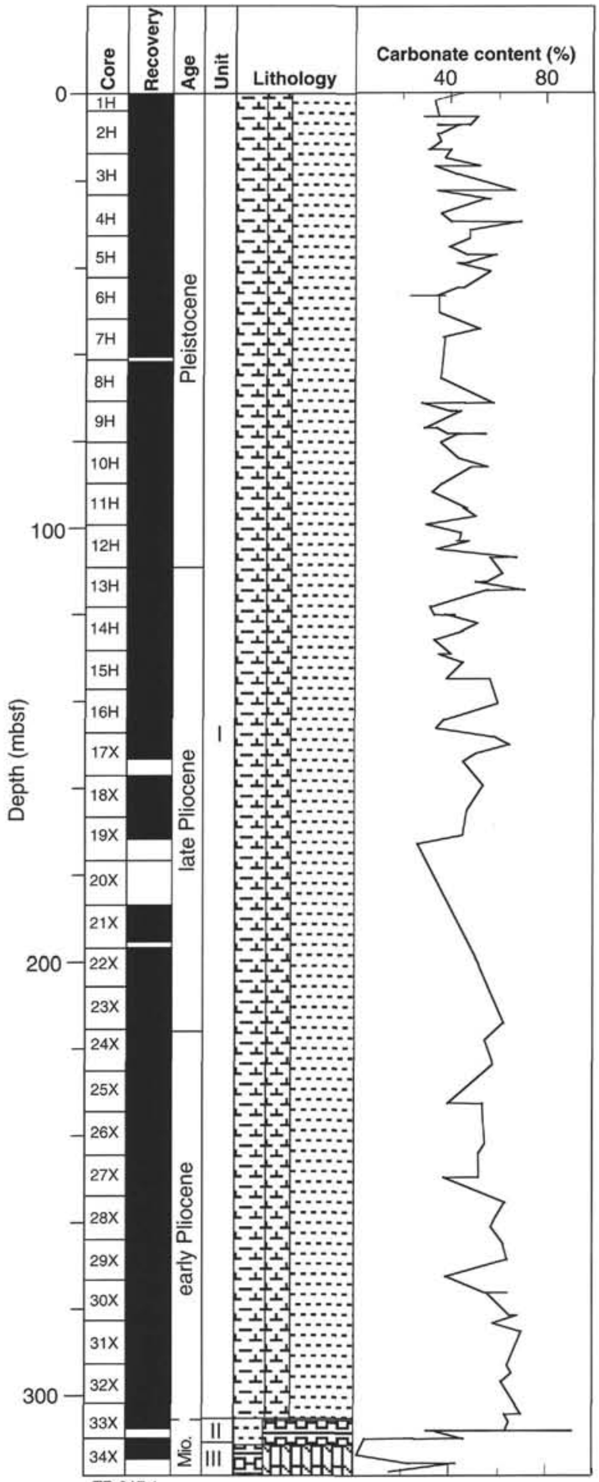

Figure 4. Generalized lithostratigraphic column with record of core recovery and carbonate content for Hole 975B. Carbonate content was determined by coulometric analysis (see "Organic Geochemistry" section, this chapter). Stratigraphy is representative of that recovered at all Site 975 holes. The lithostratigraphic symbols are explained in Figure 1 of the "Explanatory Notes" chapter, this volume.

Table 2. Summary of lithostratigraphic units for Site 975.

Unit	Age	Lithology	Sedimentary structures	Occurrence	Interval (mbsf)
I	Pleistocene to Pliocene–Miocene	Major: Nannofossil or calcareous clay and silty clay	Alternating dark and light bands, through Core 975B-18X	Core 975A-1H Core 975B-1H to Section 975B-33X-2, 131 cm	0.0–9.5 0.0–305.2
		Nannofossil ooze	Foraminifer-rich silt laminae, through Core 975B-18X	Core 975C-1H to Section 975C-33X-4, 110 cm Core 975D-1H to 16H	0.0–306.3 0.0–149.9
			Bioturbation, common throughout; large burrows especially noticeable in Cores 975B-18X through 33X Slumps in Cores 975B-13X and 975C-13X and 26X		
		Minor: Organic-rich layers	Color banding		
II	Pliocene–Miocene?	Major: Micrite and micritic silty clay	Thinly interbedded and finely laminated	Section 975B-33X-2, 131 cm, to Section 975B-33X-CC, 11 cm	305.2–307.0
		Minor: Calcareous silty sand	Thin beds; graded or laminated	Section 975C-33X-4, 110 cm, to Section 975C-33X-CC	306.3–306.9
III	Miocene	Major: Gypsum and gypsiferous chalk	Finely laminated, nodular, and coarse grained with micrite matrix	Section 975B-33X-CC, 11 cm, to Section 975B-34X-CC	307.0–317.1
		Minor:		Section 975C-34X-CC	310.7–313.7
		Clay to micrite-rich clay	Thin beds		
		Foraminifer-rich gypsum silty clay	Thin laminae in Section 975B-34X-CC		
		Anhydrite	Thin laminae in Section 975B-33X-CC		

Table 3. Color variation of the lithologies at Site 975.

Lithology	Colors
Nannofossil ooze	Light olive gray (5Y 6/1 and 5Y 5/2))
Nannofossil or calcareous clay to nannofossil silty clay	Light olive gray (5Y 5/2) Greenish gray (5GY 6/1) Olive gray (5Y 3/2 and 5Y 4/1) Dark yellowish brown (10YR 4/2) Light olive brown (5Y 5/6) Moderate yellowish brown (10YR 5/4) Moderate olive brown (5Y 4/4) Grayish olive (10Y 4/2)
Organic-rich layer	Olive black (5Y 2/1) Greenish black (5GY 2/1) Brownish black (5YR 2/1)
Micrite	Yellowish gray (5Y 8/1)
Micritic silty clay	Greenish gray (5GY 6/1)
Calcareous silty sand	Greenish gray (5GY 6/1) Light gray (N7)
Gypsum	Light olive gray (5Y 6/2 and 5Y 5/2) Moderate olive brown (5Y 4/4 and 5Y 5/4)
Clay to micrite-rich clay	Grayish green (5G 4/2)
Foraminifer-rich gypsum silty sand	Grayish green (5G 5/2)
Anhydrite	White (N9)

Rare laminae and thin beds (less than 3 cm thick) rich in silt and/or sand were found throughout Unit I (Figs. 8, 9). Some of these layers are normally graded; most have sharp lower contacts and bioturbated upper contacts. The silt and sand fractions of these sediments are dominated by foraminifers, many of which are filled with opaque minerals (pyrite?), shell fragments, or quartz.

Intervals of finely laminated nannofossil clay, nannofossil silty clay, and nannofossil ooze are separated by homogeneous, bioturbated intervals of similar lithologies in Cores 975B-27X through 30X and 975C-26X through 30X (Fig. 10). The laminations are parallel and have apparent dips (not produced by XCB-drilling) that range from 0°–38° (see "Structural Geology" section, "Explanatory Notes" chapter, this volume).

Several intervals of low- to high-angle dipping beds (interpreted as slumps) are present at Site 975 (see "Structural Geology" section, "Explanatory Notes" chapter, this volume). One is notable because it exhibits different structure in Holes 975B, 975C, and 975D. An interval of thinly color-banded, light olive gray and greenish gray nannofossil clay about 1 m in thickness is folded and contorted in Cores 975B-13H and 975D-13H (Fig. 11). At the same stratigraphic level in Core 975C-13H, a 1-m-thick interval of color-banded sediments is horizontally layered (Fig. 12). Because of the similar thicknesses of the horizontally layered and folded intervals, we attempted to establish whether the horizontal interval contained any type of stratigraphic repetition. Although none was obvious from visual inspection, color scanning of the horizontally banded section in Core 975C-13H at a 1-cm scale indicated the possibility of repetition of bands through recumbent isoclinal folding (see "Composite Depth" section, this chapter).

Thirty-seven organic-rich layers (ORLs; defined as containing organic carbon concentrations that are above background) of Pleistocene to Pliocene age were recovered in Unit I. The ORLs recovered at Site 975 are similar to those at Site 974 (Fig. 13, see "Lithostratigraphy" section, "Site 974" chapter, this volume). These ORLs are described as color banded, homogeneous, or composite, and they are classified as Types I through V according to their total organic carbon content (Tables 4, 5; see also "Lithostratigraphy" section in "Explanatory Notes" chapter, this volume). Correlation of individual organic-rich layers between holes at Site 975 is shown in Figure 14.

Significant abundances of calcite micrite (up to 15%–20%) occur sporadically throughout Unit I. Estimates of micrite in some smear slides from depths greater than about 200 mbsf reach 40%. Trace to minor amounts of dolomite are present, especially near the base of Unit I. Recrystallization of carbonate (possibly magnesian calcite) from underlying Unit II sediments (see below) may have provided the Mg^{2+} for secondary precipitation of this dolomite.

The boundary between Units I and II was placed at the base of a grayish olive, calcareous silty clay that overlies light olive gray, micritic nannofossil clay (Fig. 15). Bulk mineralogy of the silty-to-clay layer as determined by X-ray diffraction analysis is similar to that of

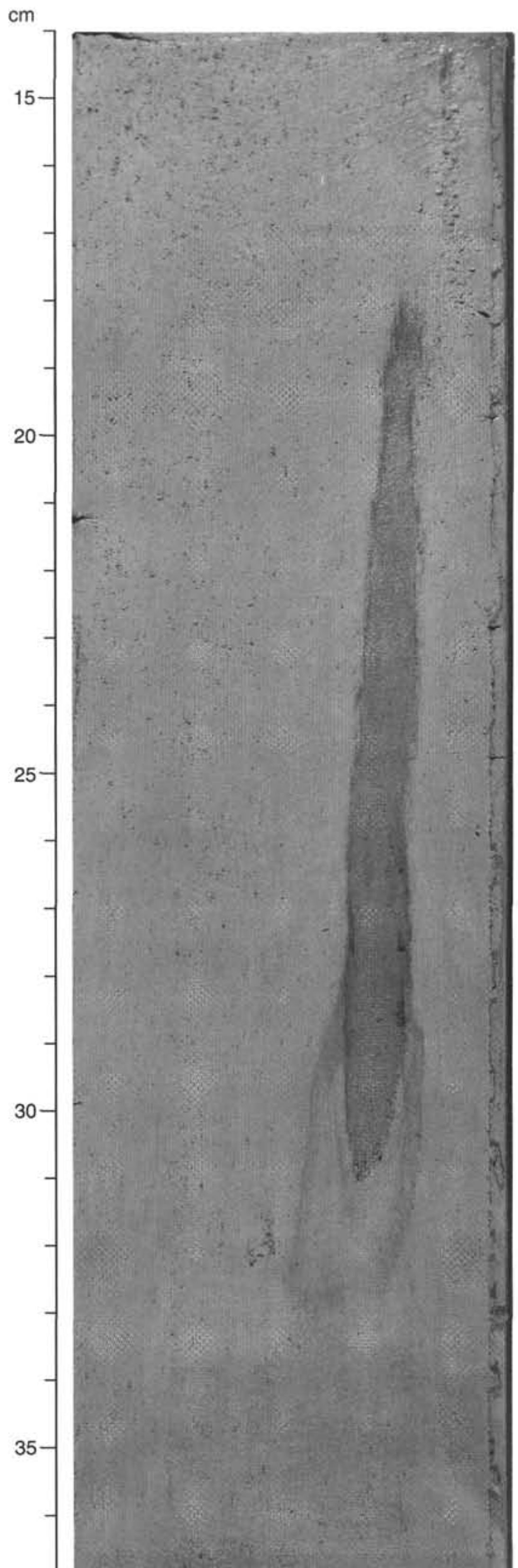

Figure 5. Large vertical burrow (*Arenicolites*?) from Section 975D-8H-3 (68 mbsf) in Unit I.

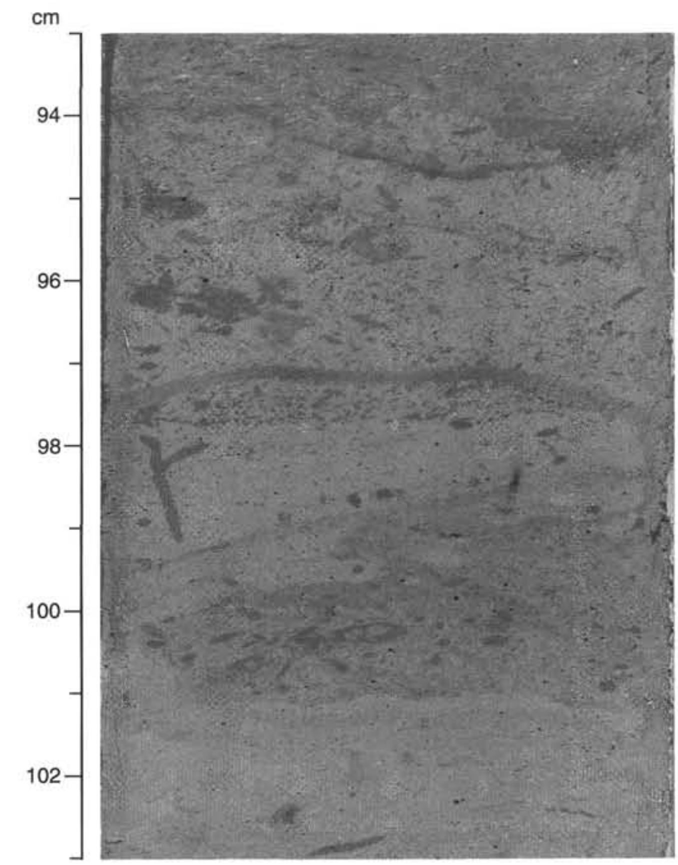

Figure 6. Heavily burrowed (*Planolites* and *Chondrites*) interval from Section 975B-30X-6 (282 mbsf) in Unit I.

the overlying nannofossil oozes (calcite, clay minerals, minor quartz, and trace amounts of dolomite), but relative abundances of quartz, clay minerals, and dolomite are much greater in this coarser-grained interval. In addition, the Unit I/II boundary marks a distinct textural change from the bioturbated nannofossil oozes and clays of Unit I to the finely laminated and interbedded micritic silts and clays downcore.

Unit II

Hole 975B, Sections 33X-2, 131 cm through 33X-CC, 11 cm, 305.2–306.97 mbsf;
Hole 975C, Sections 33X-4, 110 cm through 33X-CC, 306.3–306.9 mbsf.

Lithostratigraphic Unit II is a thin interval of Pliocene–Miocene sediments that overlies the Messinian evaporites of Unit III. Stratigraphic sections showing major and minor lithologies of Units II and III from Holes 975B and 975C are in Figure 16. The following description is based primarily on the sequence in Hole 975B, where a more complete section of Unit II was recovered (2.8 m vs. 0.6 m in Hole 975C). The two main lithologies of Unit II are yellowish gray micrite and greenish gray, micritic silty clay. These two main lithologies are interbedded with rare intervals of light gray to greenish gray calcareous silty sand. Mineralogy of the sediments was determined by smear-slide observations and X-ray diffraction analysis.

The micrite is composed of silt-sized, lens-shaped crystals of calcite and trace amounts of foraminifers, quartz, and clay minerals. Beds of relatively pure micrite range in thickness from a few milli-

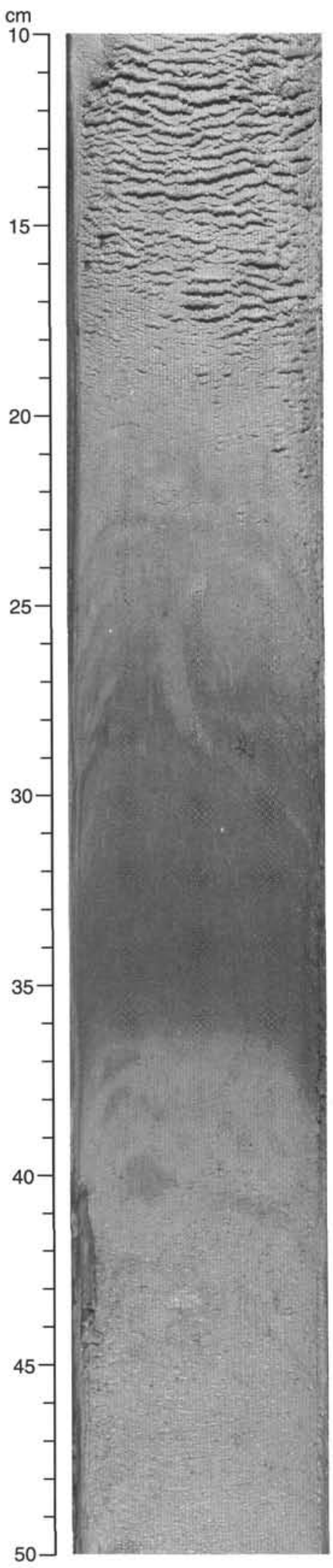

Figure 7. Example of a cycle of darker nannofossil clay overlain by lighter nannofossil ooze to nannofossil clay from Section 975C-4H-7 (31 mbsf). The upper boundary of the darker interval is bioturbated.

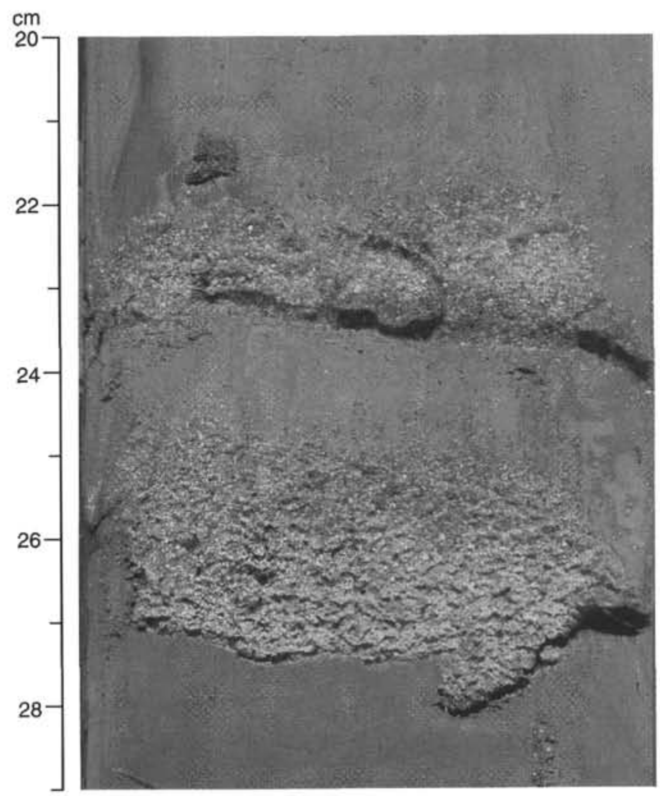

Figure 8. Two layers of calcareous sandy silty clay from Section 975C-10H-4 (83 mbsf). The upper layer contains 40% clay, 15% foraminifers, 28% nannofossils, 10% inorganic calcite, 2% quartz, and 5% accessory minerals according to smear-slide analysis.

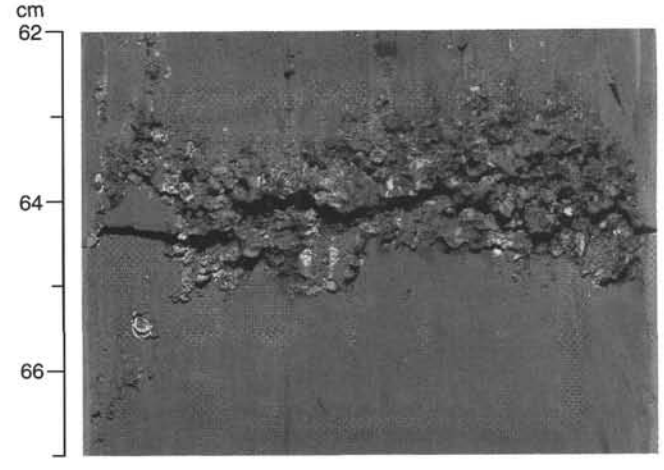

Figure 9. Sandy horizon from Section 975C-9H-6 (77 mbsf). The sand component is largely shell fragments and foraminifers, with lesser quartz.

meters to about 5 cm (light intervals in Fig. 17). These beds display fine wavy laminations, visible as alternations of slightly darker and lighter shades of yellowish gray (for example, intervals 975B-33X-3, 67–69 cm and 82–85 cm; Fig. 17). Faint greenish gray laminations are visible in some of the micrite beds, indicating admixture of some micritic silty clay.

The micritic silty clay contains major amounts of calcite, clay minerals, and quartz, minor amounts of dolomite, and traces of feldspar. A low percentage of nannofossils was seen in smear slides of

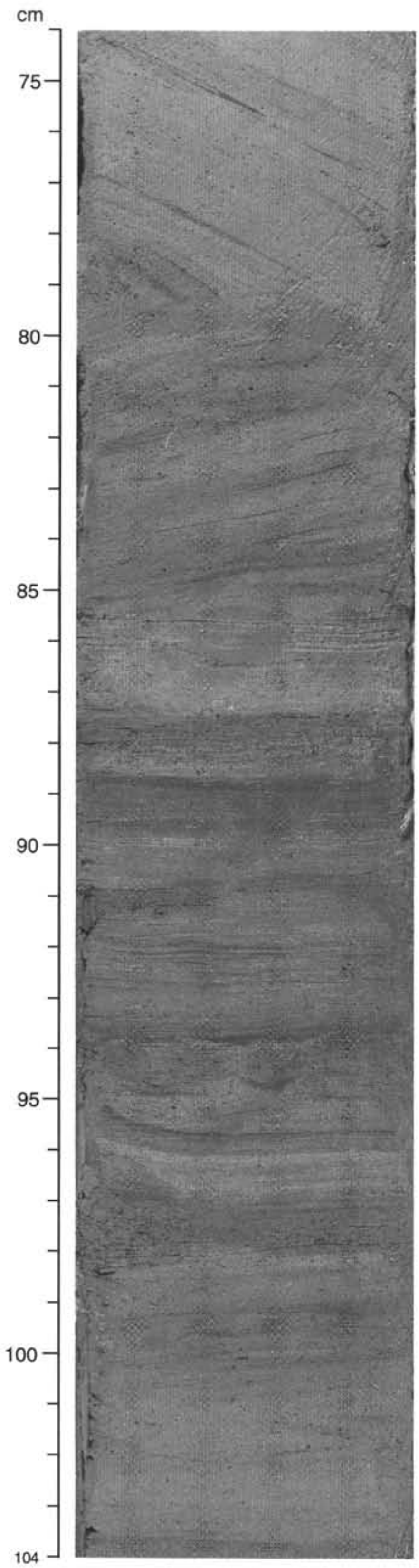

Figure 10. Finely laminated nannofossil ooze and nannofossil clay from Section 975B-30X-5 (280 mbsf). Both horizontal and steeply dipping laminations are present.

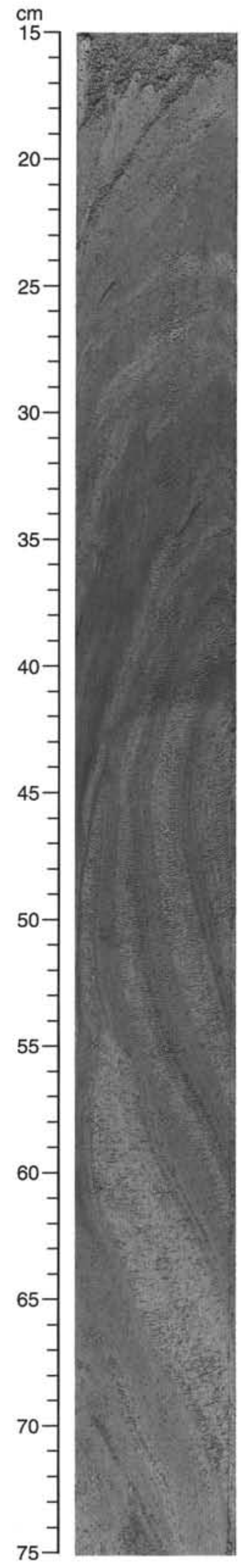

Figure 11. Folded color-banded interval from a slump in Section 975B-13H-4 (113 mbsf). This forms part of an east-facing fold-pair based on core coordinates.

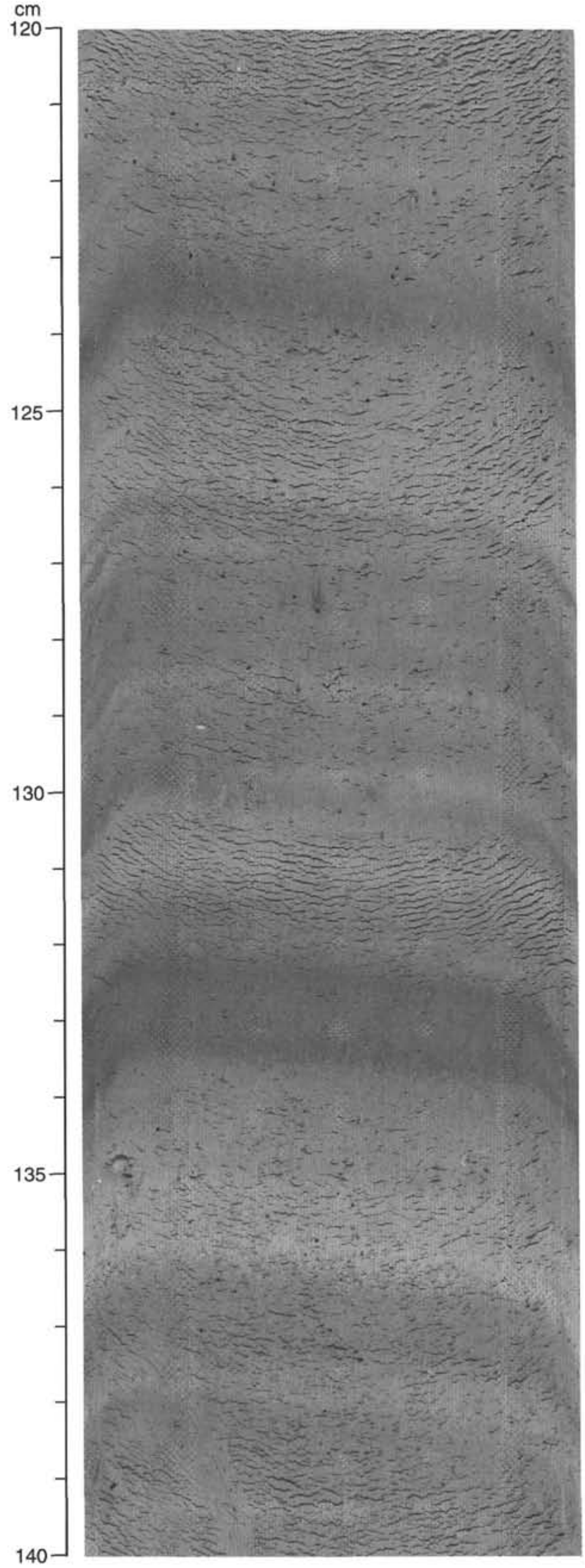

Figure 12. Horizontal color-banded interval from Section 975C-13H-5 (116 mbsf) thought to be stratigraphically equivalent to the interval in Figure 11.

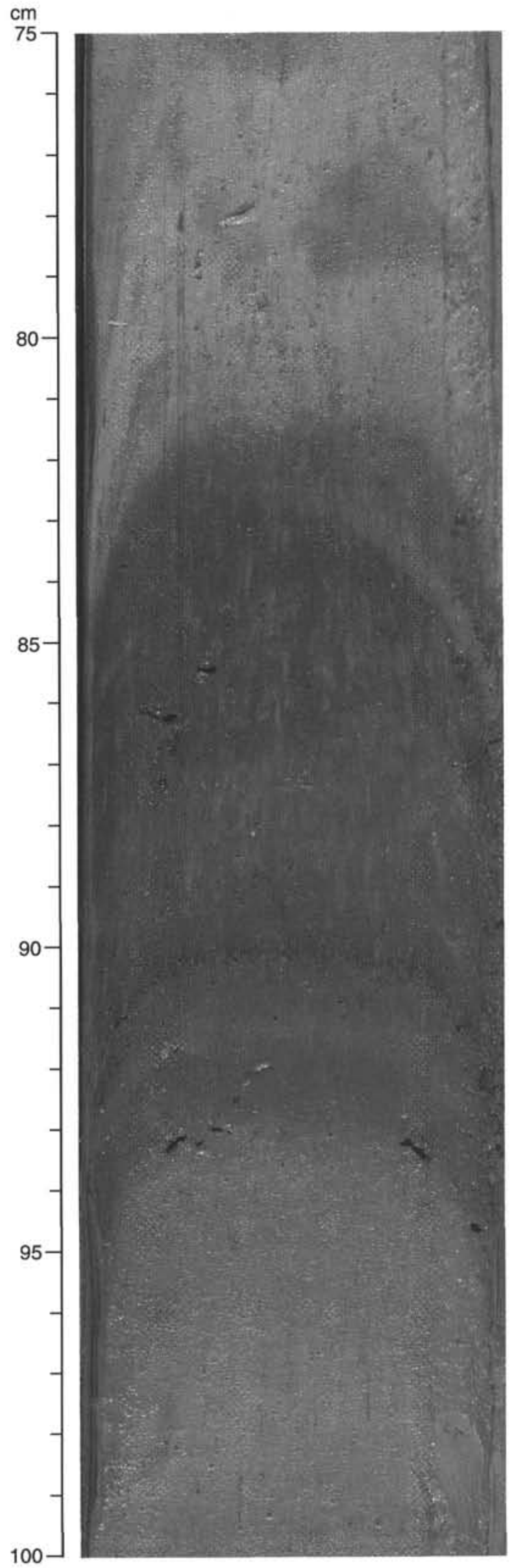

Figure 13. Example of a thinly color-banded, organic-rich layer from Section 975B-2H-3 (8 mbsf). The dominant colors are olive gray with olive black and dark greenish gray. The upper part (82–89.5 cm) is finely bioturbated. The organic carbon content is 1.54% at 84–85 cm.

Table 4. Correlation of organic-rich layers at Site 975.

Class	Type	Key bed number	Core, section, interval (cm)	Top (mbsf)	Bottom (mbsf)	TOC (%)	Core, section, interval (cm)	Top (mbsf)	Bottom (mbsf)	TOC (%)	Core, section, interval (cm)	Top (mbsf)	Bottom (mbsf)
			161-975B-				161-975C-				161-975D-		
CB	II	M1	2H-3, 82–93	7.920	8.030	1.54	2H-5, 12–28.5	8.520	8.685		2H-1, 91.5–104.5	8.315	8.445
H	V	M2									2H-5, 74–78.5	14.140	14.185
CB	V	M3									2H-5, 118–128.5	14.580	14.685
CB	II	M4					3H-2, (38)71–79	14.110	14.190	1.66	2H-5, 137–139.5	14.770	14.795
CB	II	M5	3H-1, 130–133	14.900	14.930	1.52	3H-2, 97–106	14.370	14.460	1.12	2H-6, 2–14	14.920	15.040
H	II	M6	3H-2, 112–120	16.220	16.300	1.72	3H-3, 92.5–101	15.825	15.910	1.48	2H-6, 140–148	16.300	16.380
H	III	M7	3H-4, 60–65	18.700	18.750	0.92	3H-5, 53–57	18.430	18.470	0.84	3H-2, 14–19	18.540	18.590
H	IV	M8	3H-7, 39/42–45	23.000	23.050	0.38	4H-1, 121–122	22.610	22.620		3H-5, 28/32–35.5	23.200	23.255
H	II	M8	4H-2, 49.5–56.5	25.095	25.165	0.97	4H-3, 120–126	25.600	25.660	0.78 (not max?)	3H-7, 26–33	26.160	26.230
CB	II	M9	4H-CC, 8–9.5	32.610	32.625	1.12	5H-1, 145–150	32.350	32.400	1.42	4H-5, 55–65.5	32.950	33.055
							5H-2, 0–2	32.400	32.420	1.13			
			5H-1, disturbed sediments at 46/54 and 58/67	33.100	33.220	(0.68)							
C	III	M10	5H-3, 113–117.5	36.730	36.775	0.89 (not max)	5H-5, 37–39.5	37.270	37.295	0.85 (not max?)	5H-1, 119–123	37.090	37.130
CB	II	M11	5H-5, 116–123.5	39.760	39.835	1.83	5H-7, 57.5–63.5	40.475	40.535	1.90	5H-3, 136–143.5	40.260	40.335
C	II	M12	6H-1, flow in, about 40	42.500			6H-2, 117–130.5	43.070	43.205	1.36	5H-6, 45.5–58	43.855	43.980
H	II	M13	6H-2, 100–103	44.600	44.630	1.04	6H-4, 29.5–31	45.195	45.210	1.09	Missing or 5H-CC, Paleo	45.640	45.690
C	I	M14	6H-3, 77–87	45.870	45.970	2.80	6H-5, 21.5–31.5	46.615	46.715	2.90	6H-1, 125.5–138	46.655	46.780
CB	II	M15	6H-4, 29–33	46.890	46.930	1.36	6H-5, 127–130.5	47.670	47.705	1.54	6H-2, 86.5–92	47.765	47.820
CB	II	M16	6H-4, 44–53	47.040	47.130	1.26	6H-5, 140.5–150	47.805	47.900	1.61	6H-2, 103–112.5	47.930	48.025
CB	II	M17	6H-6, 20.5–25.5	49.805	49.855	(0.82)	7H-1, 67.5–73	50.575	50.630	1.10	6H-4, 101.5–105.5	50.915	50.950
H	II	M18	7H-4, 66–70.5	56.760	56.805	0.95	7H-5, 106.5–108.5	59.965	59.985	0.76	7H-2, 43.5–46.5	56.835	56.865
H	V	M19	8H-4, 124.5–126	66.845	66.860		8H-6, 145–146	68.350	68.360		8H-3, 72.5–74	68.125	68.140
C	II	M20	8H-7, 22–32	70.320	70.420	1.47	9H-2, 112 or 123–128.5	71.575	71.685		8H-5, 129–139	71.690	71.790
C	II	M21	8H-CC, 6–11	70.720	70.770		9H-3, 2–14	71.920	72.040	1.00	8H-6, 13–24	72.030	72.140
			9H-1, 13–25 disturbed	70.730	70.85	0.95							
			Repetition by faulting or by drilling??		overlap								
ORL CB	II	M22	9H-1, 141–145	72.010	72.050	1.00	9H-3, 128–133	73.180	73.230		8H-6, 140–145	73.300	73.350
ORL H	I	M23	9H-2, 119–125	73.290	73.350	2.59	9H-4, 98–105	74.380	74.450		9H-1, 22.5–29.5	74.125	74.195
ORL CB	V	M24	9H-3, 115–123	74.750	74.830		9H-5, 91–97	75.810	75.870		9H-2, 24–28.5	75.640	75.685
ORL CB	I	M25	9H-5, 82 or 85–91.5	77.435	77.515	2.69	9H-7, 50–61	78.400	78.510		9H-3, 145.5–150	78.355	78.400
ORL CB	I	M25									9H-4, 0–3	78.400	78.430
ORL CB	III	M26	9H-6, 32–33	78.420	78.430	0.83	10H-1, 54–55.5	78.940	78.955		9H-4, 100.5–101	79.405	79.410
ORL C	V	M27	9H-6, 122–124	79.320	79.340		10H-2, 9–12.5	79.990	80.025		9H-5, 52–59	80.420	80.490
ORL H	I	M28	10H-3, 75.5–77.5	83.855	83.875	2.02	10H-5, 24–28	84.640	84.680		10H-1, 120.5–124.5	84.605	84.645
ORL C	III	M29	10H-4, 137–140	85.970	86.000	(0.56)	10H-6, 73–79	86.630	86.690		10H-3, 17–20.5	86.570	86.605
ORL C	III	M29									10H-3, 23.5–28 Repetition by reverse faulting	86.635	86.680
ORL CB	II	M30	11H-4, 87–90	94.970	95.000	1.08	11H-5, 127–129.5	95.170	95.195		11H-2, 43–44	94.830	94.840
ORL H	V	M31	11H-7, 78–80	99.380	99.400		12H-2, 28–30	99.180	99.200		11H-5, 69–71.5	99.590	99.615
ORL CB	III	M32	12H-1, 66–68	99.760	99.780	0.84	12H-2, 135–135.5	100.250	100.255		11H-6, 27–29	100.670	100.690
ORL C	II	M33	12H-5, 105–114	106.150	106.240	0.99	12H-6, 109–115	105.990	106.050		12H-3, 42–50.5	105.820	105.905
ORL C	V	M34					14H-3, 67–68	118.670	118.680		13H-6, 14–16.5	119.540	119.565
ORL CB	III	M35	14H-1, 76–77	118.860	118.870	0.82	14H-4, 57–58	120.070	120.080		13H-7, 3–5	120.930	120.950
ORL C	IV	M36	14H-2, 25–30	119.850	119.900	(0.35)	14H-5, 10–15	121.100	121.150		14H-1, 3.5–6	121.435	121.460
ORL H	III	M37	14H-3, 104–106	122.14	122.16	(0.56)	14H-6, 97–98.5	123.470	123.485		14H-2, 112–115	124.020	124.050

Notes: At Hole 975A, key bed number M1 is found in Section 1H-5, 69–79.5 cm (6.690–6.795 mbsf). Key bed numbers identify individual organic-rich layers in Figure 14. Type: I = >2% TOC; II = 1%–2% TOC; III = 0.5%–1% TOC; IV = <0.5% TOC; V = TOC not determined. ( ) = TOC for ORLs with possible admixture of background sediment or which are bioturbated. Class: CB = color banded; H = homogeneous; C = composite (one or more gray layers/laminae within).

Table 5. Types and classes of organic-rich layers at Site 975.

	No. of Pleistocene and upper Pliocene ORLs
Type	
I	4
II	18
III	7
IV	2
V	7
Total	37
Class	
CB	16
H	11
C	10
Total	37

Notes: Type: I = >2% TOC; II = 1%–2% TOC; III = 0.5%–1% TOC; IV = <0.5% TOC; V = TOC not determined. Class: CB = color banded; H = homogeneous; C = composite (one or more gray layers/laminae within).

these beds. Beds of micritic silty clay range in thickness from the millimeter scale up to about 10 cm (darker intervals in Fig. 17). These beds are generally structureless, but in places are laminated (for example, interval 975B-33X-3, 88–90 cm; Fig. 17).

Although micrite and micritic silty clay occur in discrete beds as described above, their most common occurrence is in finely-interlaminated intervals (Fig. 18). Discontinuous laminae of silt- to sand-sized carbonate grains (cemented micrite?) are present within these intervals of finely laminated micrite and micritic silty clay (for example, at 2 cm in Section 975B-33X-3, Fig. 18).

Calcareous silty sand is composed primarily of calcite, clay minerals, quartz, feldspar, and dolomite. Bioclasts and foraminifers, many with rims of isopachous cement, are common. In addition, a graded interval of calcareous silty sand from Section 975B-33X-3, 143–144 cm (306.8 mbsf, Fig. 19) contains rock fragments, glauconite, gypsum, and a wide spectrum of accessory minerals (including garnet, zoisite, zircon, tourmaline, pyroxene(?), epidote, and rutile). Some of the quartz grains from this interval are highly rounded. Downcore, a second bed of calcareous silty sand is horizontally laminated and contains abundant celestite ($SrSO_4$) (Fig. 20; Section 975B-33X-CC, 9–11 cm, 306.95–306.97 mbsf).

In Hole 975C, Unit II consists entirely of interlaminated to thinly interbedded micrite and micritic silty clay (Fig. 16). In Hole 975B, similar lithological association (Unit II; 3 in Fig. 16) is underlain by a sequence of three thin beds of (1) graded calcareous silty sand (4.5 cm thick), (2) micritic silty clay (5 cm thick), and (3) laminated calcareous silty sand (8 cm thick). The Unit II/III boundary was placed at the contact between the laminated calcareous silty sand bed and an underlying interval of gypsum (Fig. 20; Section 975B-33X-CC, 11 cm, 306.97 mbsf). The contact appears sharp although fracturing and biscuiting by XCB-drilling have obscured the interface between the two lithologies.

Unit III

Hole 975B, Sections 33X-CC, 11 cm through 34X-CC, 306.97–317.1 mbsf;
Hole 975C, Core 34X, 310.7–313.7 mbsf.

Lithostratigraphic Unit III comprises 4.4 m and 1.6 m of late Miocene (Messinian) evaporites at Hole 975B and Hole 975C, respectively. The following discussion relies primarily on the thicker sequence recovered at Hole 975B (Fig. 16) and is based on visual, smear-slide, and thin-section observations and X-ray diffraction analyses. We have used the classification scheme of evaporitic rocks outlined in Carozzi (1993).

The major lithology in this evaporite sequence is light olive gray to moderate olive brown gypsum that occurs in three facies: nodular,

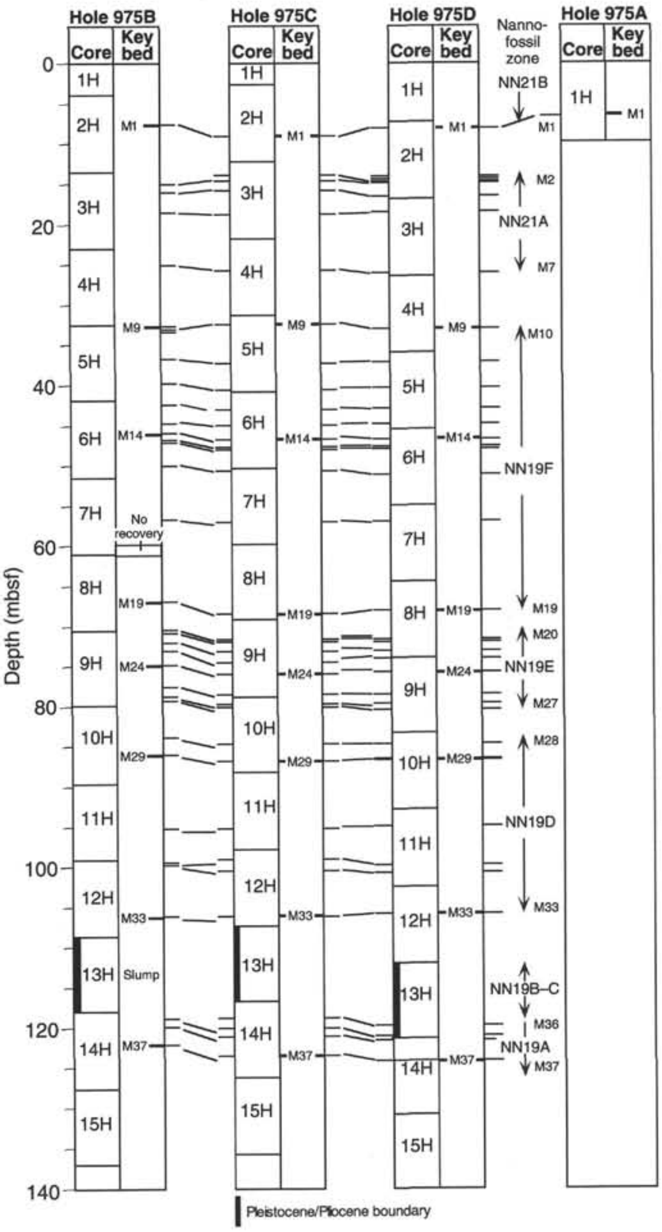

Figure 14. Correlation of organic-rich layers between holes at Site 975. The correlation is based on characteristics of the layers recorded on Visual Core Description sheets and in photographs, on total organic carbon content, and on age as indicated by nannofossil zones. The identification of individual layers (M1-M37) is given in Table 4.

finely-laminated, and gypsiferous chalk (coarse crystals in a micrite matrix). The nodular facies is characterized by irregular, coalescing nodular to wavy-bedded massive gypsum (Fig. 21). This facies develops by aggrading crystallization of coarse gypsum crystals along the upper surfaces of laminae within the finely laminated gypsum facies (Fig. 22).

In the finely laminated gypsum facies, the laminae have planar bases with planar to irregular (wavy) upper surfaces (Fig. 23). Clay minerals and micrite are concentrated along lamina boundaries, particularly at the upper wavy surfaces; locally, these contacts are stylolitized. In thin section, the laminae exhibit progressive changes in grain size, with interlocking gypsum crystals becoming coarser towards the top of the laminae (Fig. 24A).

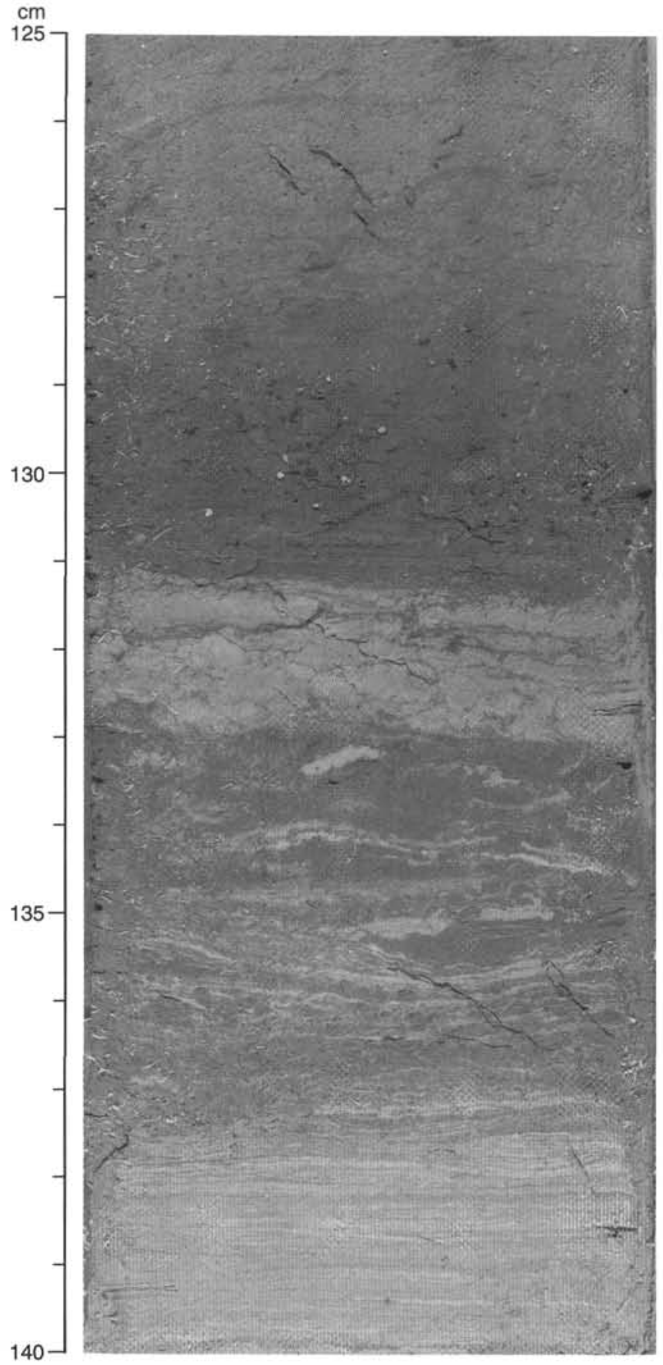

Figure 15. Boundary of Units I and II is located at 131 cm in Section 975B-33X-2 (305.21 mbsf). It separates a sandy silty interval at the base of the nannofossil clay and nannofossil clay sequence of Unit I from finely laminated micrite and micritic silty clay of Unit II.

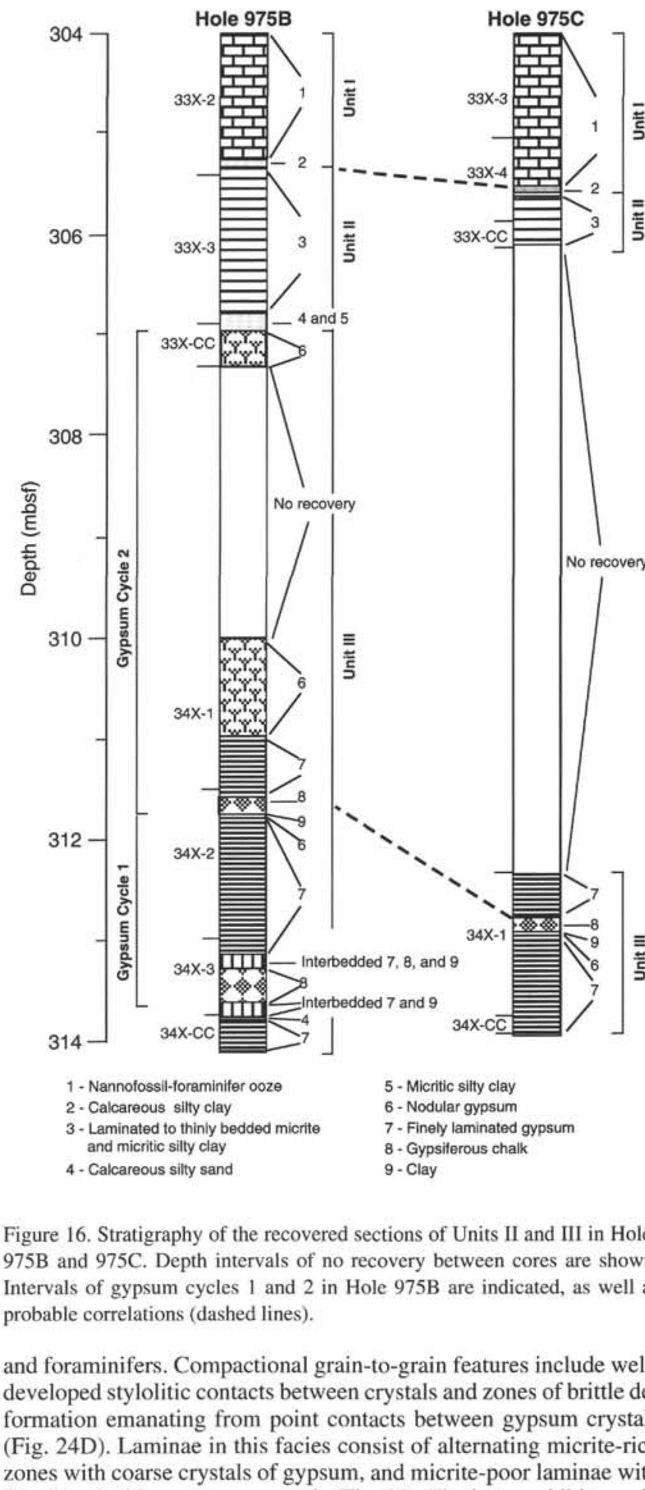

Figure 16. Stratigraphy of the recovered sections of Units II and III in Holes 975B and 975C. Depth intervals of no recovery between cores are shown. Intervals of gypsum cycles 1 and 2 in Hole 975B are indicated, as well as probable correlations (dashed lines).

The gypsiferous chalk facies contains gypsum crystals that range up to 1 cm in length. A thin section of this facies shows large euhedral crystals of gypsum in a matrix-supported to grain-supported texture, commonly with the long axes of crystals aligned parallel to bedding (Fig. 24B). The matrix is composed of fine micrite and whole to fragmented pelagic foraminifers. Euhedral crystal forms and linear matrix-inclusion trails that pass through adjacent crystals provide evidence for an authigenic origin of these gypsum grains (Fig. 24C). The inclusions within these crystals consist of nannofossils, micrite, and foraminifers. Compactional grain-to-grain features include well-developed stylolitic contacts between crystals and zones of brittle deformation emanating from point contacts between gypsum crystals (Fig. 24D). Laminae in this facies consist of alternating micrite-rich zones with coarse crystals of gypsum, and micrite-poor laminae with fine, interlocking gypsum crystals (Fig. 25). The latter exhibit poorly developed enterolithic folding.

Unit III also comprises several minor lithologies. Thin (1–2 cm) beds of grayish green clay to micrite-rich clay contain abundant clay minerals and quartz, variable calcite, minor dolomite, and trace amounts of gypsum and feldspar. One thin bed of foraminifer-rich gypsum silty sand and a thin white lamina of anhydrite are also present.

The evaporites of Unit III comprise two broad cycles in Hole 975B (Fig. 16). Both of these cycles begin with a clay or micrite-rich clay interval, overlain by laminated to thinly-bedded gypsiferous

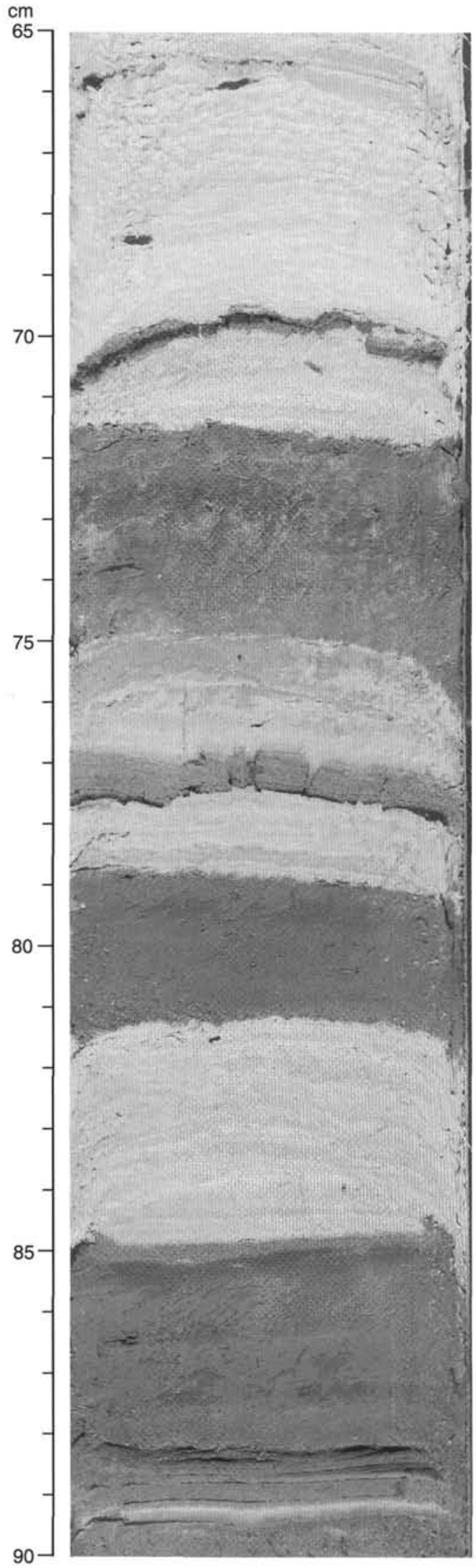

Figure 17. Thinly interbedded micrite and micritic silty clay from Section 975B-33X-3 (306 mbsf) in Unit II.

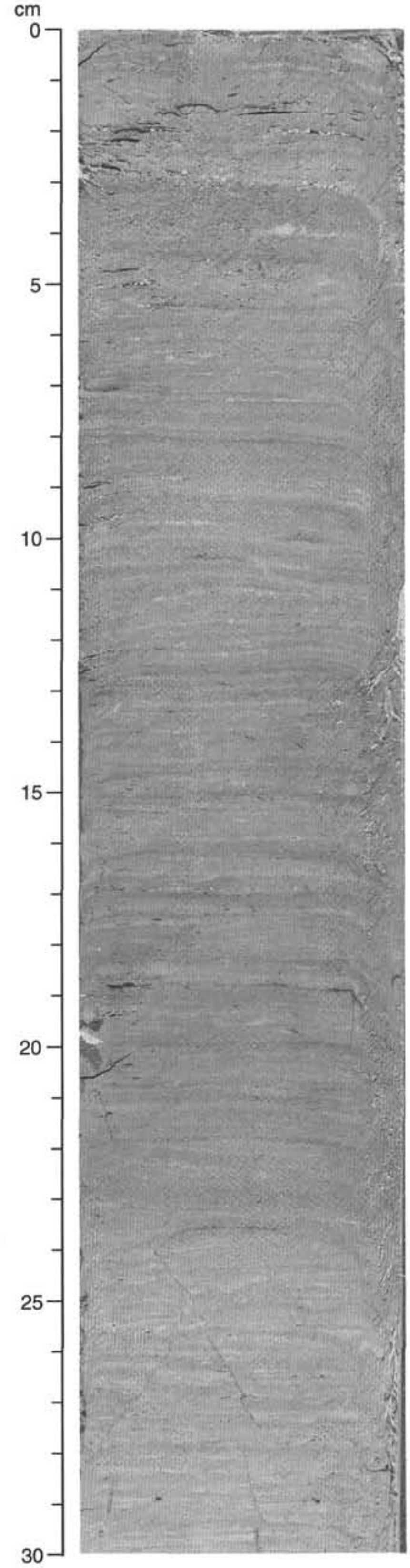

Figure 18. Finely laminated micrite and micritic silty clay from Section 975B-33X-3 (305 mbsf) in Unit II.

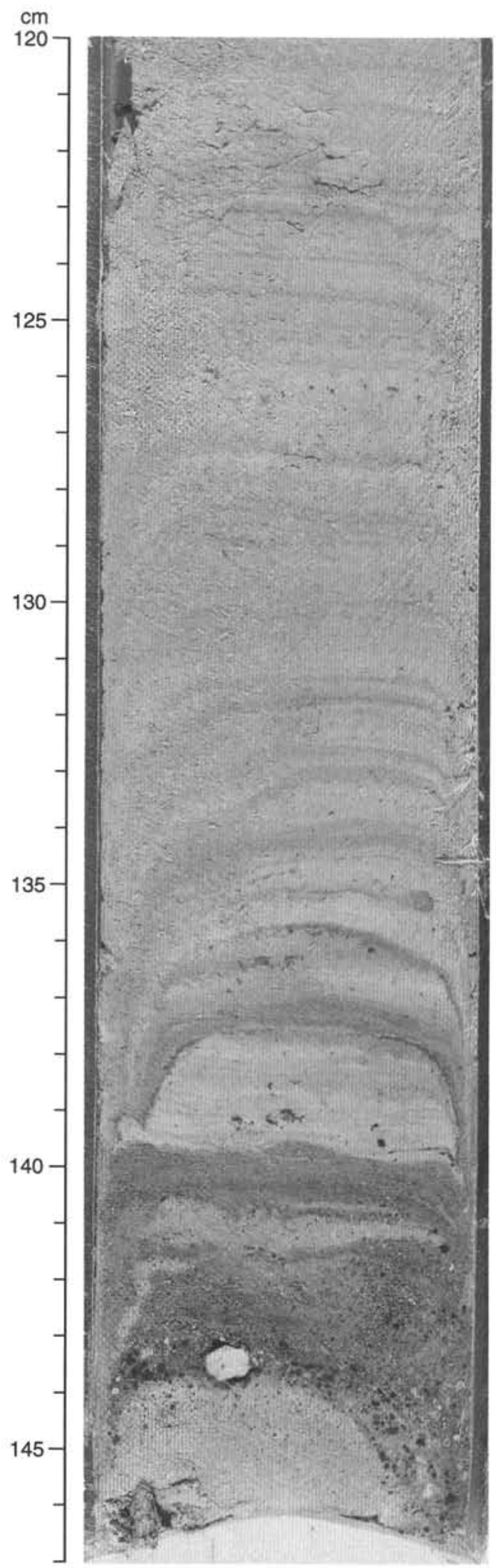

Figure 19. Layer of calcareous silty sand at 139.5–144 cm in Section 975B-33X-3 (306.8 mbsf) in Unit II.

chalk (Fig. 25). Thicknesses of the clay/gypsiferous chalk sequences range up to 40 cm. The gypsiferous chalk intervals are overlain by laminated gypsum, which gradationally passes upward into the nodular gypsum facies. Although nodular gypsum is restricted to a few centimeters-wide interval in the lower cycle, it is extensively developed in the upper cycle (Fig. 16).

Discussion

The Marine Sequence: Unit I

The sediments of Unit I are interpreted to have been deposited in an open marine environment. The sedimentation rates for this unit are approximately 7 cm/k.y. for the Pleistocene–Holocene and 5 cm/k.y. for the Pliocene (see "Biostratigraphy" section, this chapter), somewhat higher than those of the sediments at Site 974 (see "Biostratigraphy" section, "Site 974" chapter, this volume). The upward increase in sedimentation rate and gradual upward decrease in carbonate content with depth (Fig. 4) may reflect a shift from dominantly pelagic to hemipelagic conditions.

The rhythmic alternations of lighter nannofossil ooze to nannofossil clay and darker nannofossil clay noted in Unit I sediments likely reflect cyclicity in the delivery of terrigenous material to the site. Although the lower contacts of many of the darker intervals are sharp, clearly graded beds or lamination structures indicative of turbiditic deposition were not observed. More detailed examination of sedimentary structures by X-radiography would be necessary to recognize facies changes related to fine-grained or muddy turbidite deposition (Hill, 1984). An alternative interpretation of these facies is deposition from nepheloid flows (Pickering et al., 1989). The episodic activity of bottom currents is suggested by rare laminae and thin beds of silt or sand in the clay-rich sequence that are interpreted as lag deposits. The finely laminated intervals in the lower portions of Unit I may reflect periodic fluctuations of terrigenous input, possibly by low concentration turbidity currents, with little bed load traction (Pickering et al., 1989).

Despite the overall similarities of the ORLs at Sites 974 and 975, several differences exist. The average total organic carbon content of ORLs at Site 975 is 1.3% (Table 4; see "Organic Geochemistry" section, this chapter), lower than the average found for ORLs from Site 974 (2.4%; see "Organic Chemistry" section, "Site 974" chapter, this volume). Murat (1991) documented a positive correlation between water depth and organic carbon content for individual sapropels (ORLs) of the eastern Mediterranean basin. This trend must reflect differences with depth in preservation of organic carbon because the flux of organic carbon to the sediment-water interface generally decreases with increased water depth. The differences in total organic carbon content of the ORLs from Sites 974 and 975 may be related to the fact that water depth at Site 975 is roughly 1000 m less than at Site 974. Site age is a second difference in the record of ORLs at the two sites. More ORLs were recovered in the late Pleistocene sections (nannofossil Zone NN19F and up) at Site 975 than at Site 974.

Micrite, here defined as silt- and clay-sized grains of microcrystalline calcite, was noted as a common constituent of Unit I sediments. In a deep-marine environment, such as that represented by Unit I sediments from Site 975, recrystallization is the most likely origin of the micrite. During burial, clay-sized nannofossils and small calcite crystals on the walls of foraminifers dissolve and the calcite reprecipitates as overgrowths on larger crystals such as larger coccoliths and discoasters (Morse and Mackenzie, 1990). This well-documented reaction, which releases Sr^{2+} to pore waters (Baker et al., 1982), may also account for the gradients in dissolved Sr at this site (see "Inorganic Geochemistry" section, this chapter).

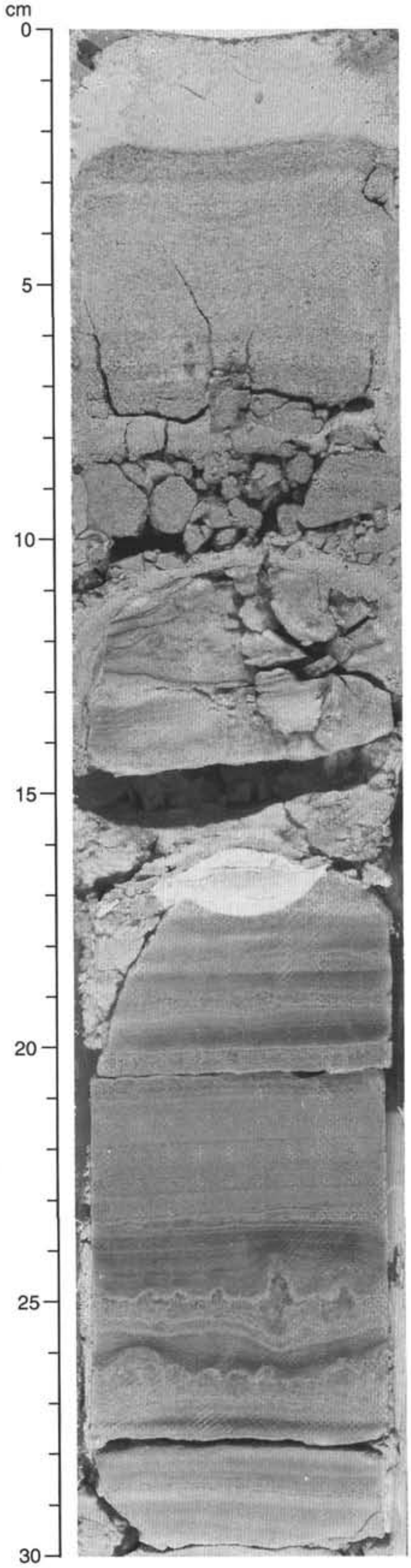

Figure 20. The boundary between Units II and III is located at 11 cm in Section 975B-33X-CC (306.97 mbsf) and separates the silty sand at the base of Unit II from the underlying gypsum of Unit III.

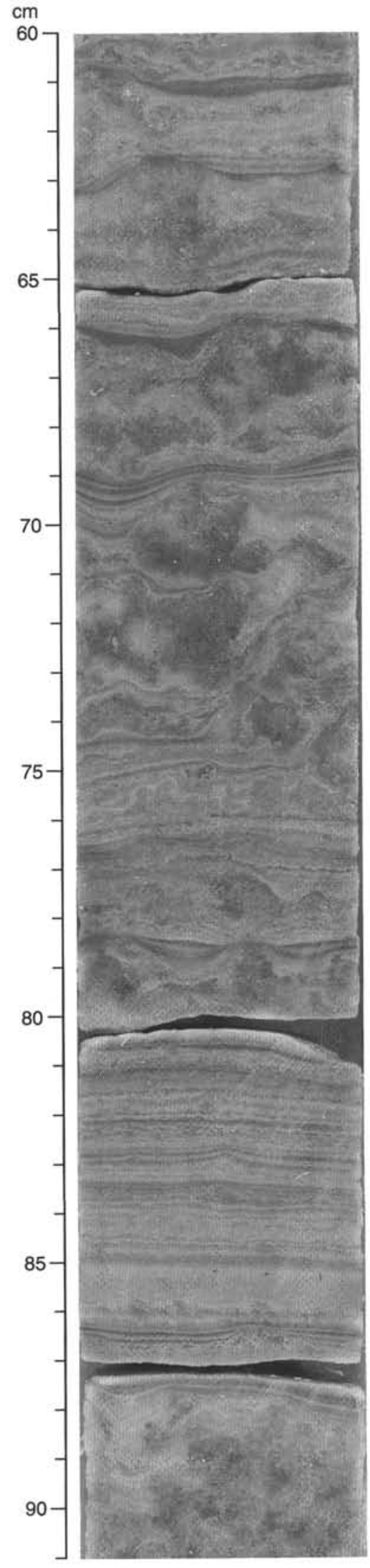

Figure 21. Nodular gypsum from Section 975B-34X-1 (310.7 mbsf).

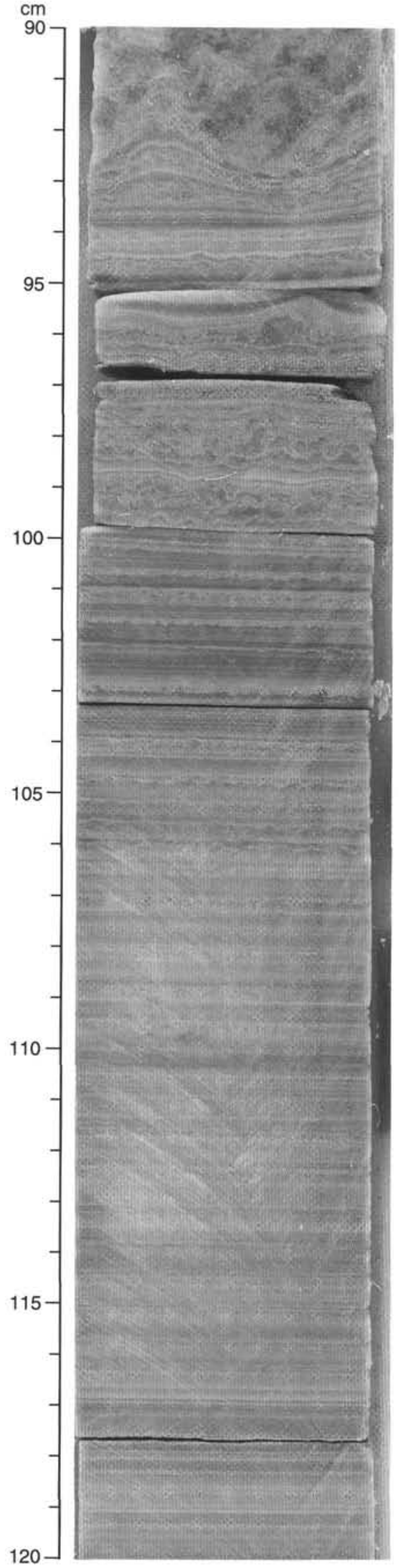

Figure 22. Transition upsection from laminated to nodular gypsum in Section 975B-34X-1 (310.9 mbsf).

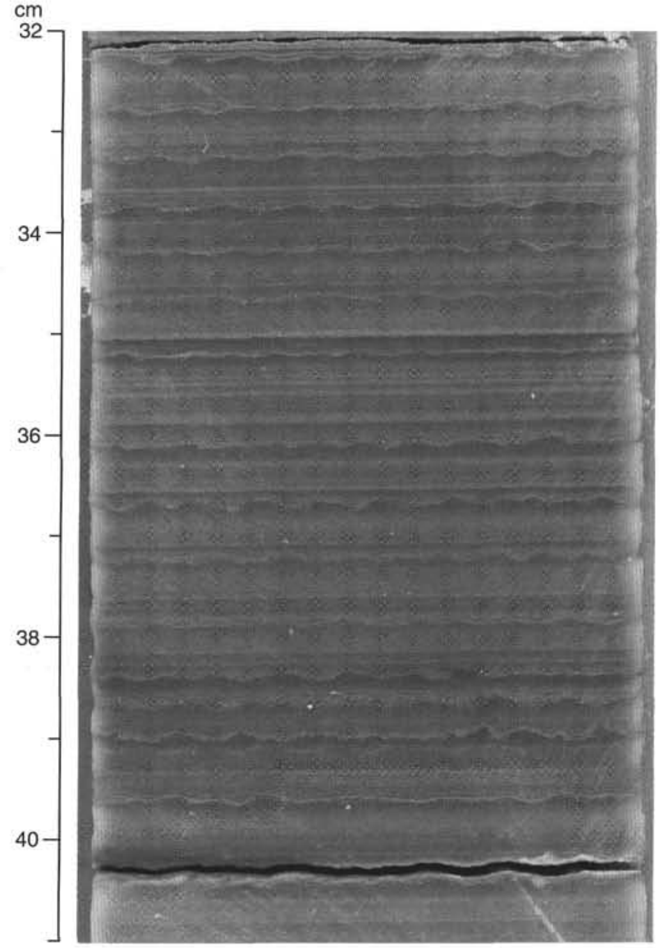

Figure 23. Laminated gypsum interval from Section 975C-34X-1 (311 mbsf).

The Post-Evaporite Sequence: Unit II

Previous drilling in the Mediterranean recovered late Messinian sediments, but a complete record of the transition from the Messinian evaporative environment to the open marine conditions represented by the lower Pliocene hemipelagic and pelagic sediments recovered at Site 975 was not obtained (e.g., Cita et al., 1978). A survey of previous drilling sites in the vicinity of Site 975 reveals that Miocene post-evaporite sedimentation varied significantly among sites (Table 6).

Unit II at Site 975 differs from these previous samples of post-evaporite, Messinian sediment in terms of carbonate mineralogy, terrigenous content, and microfossil abundance. The dolomitic marls and marl oozes of Sites 124, 132, 134, and 372 in places display fine laminations that are of possible stromatolitic origin as interpreted by shipboard scientists (Table 6; Friedman, 1973). The intervals of finely laminated micrite and micritic silty clay of Unit II have similar laminated textures, but smear-slide and X-ray diffraction analyses indicate that they contain primarily authigenic micritic calcite, not biogenic calcite and dolomite. Trace to minor amounts of dolomite were detected in Unit II, but the intervals of pure micrite contain no dolomite, only trace amounts of quartz, and few nannofossils. The descriptions of pre-evaporite sediments from Site 372 and Unit II from Site 975 are also grossly similar. Cita et al. (1978) provide a detailed description of Messinian "laminites" (finely laminated, varved, nonburrowed dolomite-bearing marls) that are overlain by dolomitic marls and laminated gypsum. The laminites consist of finely interlaminated white, fine-grained structureless layers and gray, coarser-grained, more detrital-rich layers (Cita et al., 1978) and appear in core

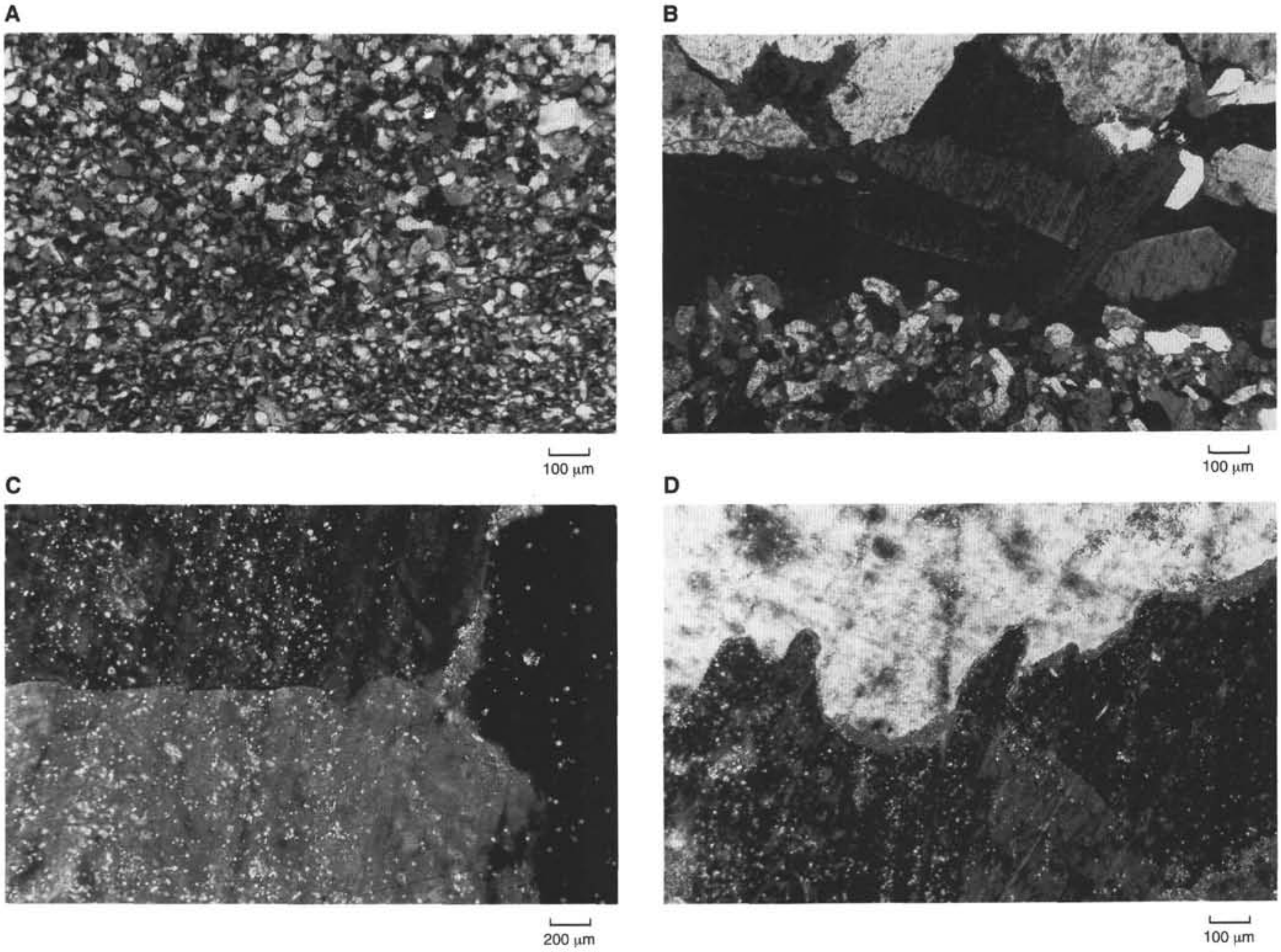

Figure 24. **A.** Thin-section photograph of upward progressive changes in grain size in laminated gypsum from Section 975B-34X-2, 103–108 (312.5 mbsf). **B.** Thin-section photograph showing alignment of euhedral gypsum grains parallel to bedding in the gypsiferous chalk in Section 975B-34X-3, 30–36 cm (313.3 mbsf). **C.** Thin-section photograph showing linear trails of inclusions that cross gypsum crystals from Section 975B-34X-3, 30–36 cm (313.3 mbsf). **D.** Thin-section photograph showing stylolites in gypsum from Section 975B-34X-2, 103–108 (312.5 mbsf).

photographs to be very similar to the finely interlaminated micrite and micritic silty clay of Unit II. The calcite of the laminites, however, is in the form of coccoliths and foraminifers, not micrite as in Unit II, Site 975.

Unit II sediments were probably deposited in a shallow water, low-energy, environment. The fine laminations could represent seasonal blooms, seasonal salinity changes, or seasonal changes in sediment input, as interpreted for Site 372 laminites by Cita et al. (1978). The fine laminations of Unit II, however, are wavy and very similar in appearance to the layering of algal or microbial mats (e.g., Friedman, 1973). The abundance of micrite in this unit favors the latter interpretation, because original precipitates (most likely magnesian calcite) in the algal-microbial mats would readily recrystallize to calcite during diagenesis (e.g., Morse and Mackenzie, 1990). Beds of micritic silty clay and calcareous silty sand in Unit II could reflect periods of increased sediment input to the coastal zone, or transitions to higher energy facies such as tidal channel or beach sediments. The boundary between Unit I and Unit II thus marks the change from an open marine environment to a shallow coastal, possibly intertidal or lagoonal, environment.

The presence of celestite in the bed of calcareous silty sand at the base of Unit II most likely indicates a diagenetic front where Sr^{2+}, released by diagenetic recrystallization and micritization of carbonates, reacts with SO_4^{2-} that diffuses up from the underlying gypsum of Unit III (e.g., Baker and Bloomer, 1988; see "Inorganic Geochemistry" section, this chapter).

The Evaporite Sequence: Unit III

The evaporite sequence of Unit III is consistent with deposition in a shallow subaqueous to supratidal environment. Petrographic evidence (inclusion composition and alignment of inclusion trails across crystal boundaries in gypsum) indicates that the intervals of gypsiferous chalk formed by in situ growth in a gypsum-saturated sediment. The presence of foraminifers and nannofossils in the matrix suggests that it originated, at least in part, from marine water.

The laminated gypsum facies is typical of intertidal to supratidal deposition, with alternating deposition of clastic gypsum and clay/micrite (Carozzi, 1993). Recrystallization of gypsum (aggrading neomorphism) leads to growth of crystal palisades (fans) along the coarser, upper margin of the laminae. Schreiber et al. (1976) attribute growth of this texture to cyclic dilution of the overlying brine. Progressive recrystallization and neomorphism of laminated gypsum produces the nodular facies. The nodular facies is most characteristic of the supratidal environment (e.g., Carozzi, 1993; Garrison et al., 1978).

The gypsum cycles identified in Unit III are similar to those recovered from Site 374 in the Ionian Sea (Fig. 26; Garrison et al., 1978). The mudstone member of Figure 26 could represent the clay to micritic clay and gypsiferous chalk intervals of Unit III at Site 975. Gradual upward shallowing produces the laminated gypsum interval which, when exposed in the supratidal environment, recrystallizes into the nodular gypsum.

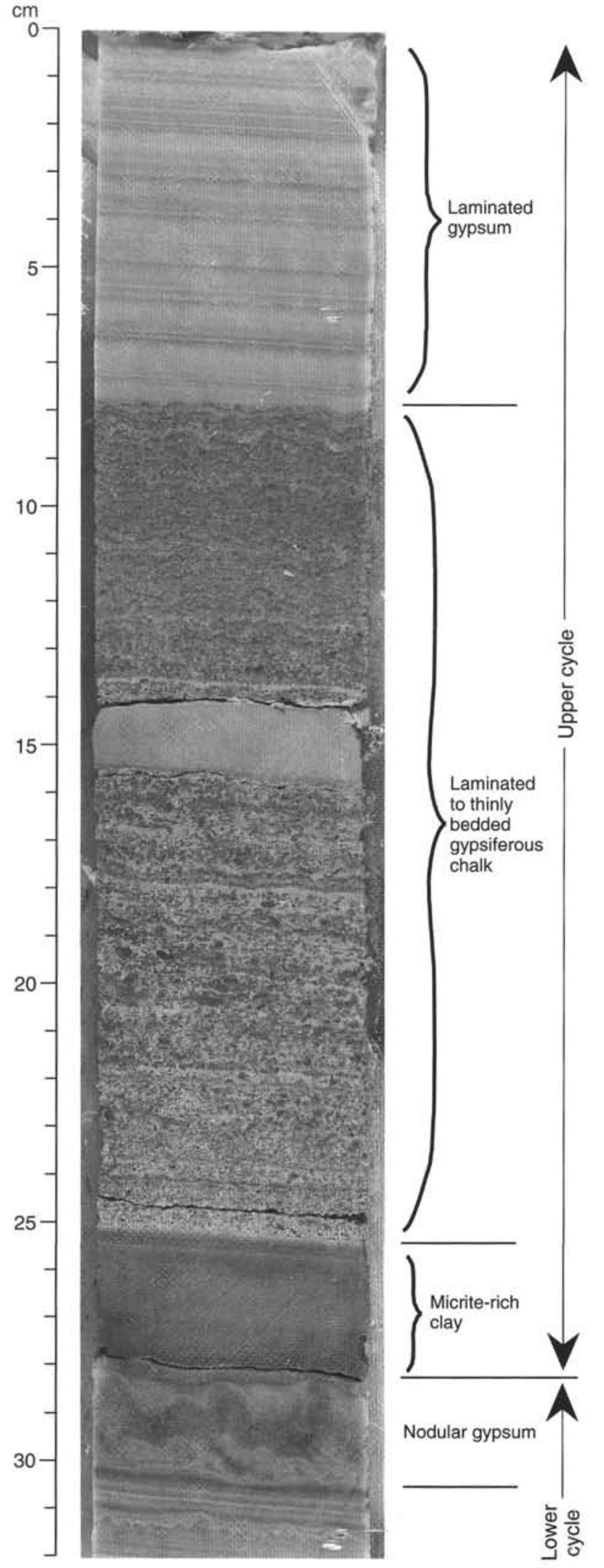

Figure 25. Lower part of a gypsum cycle showing the basal bed of micrite-rich clay overlain by gypsiferous chalk, then laminated gypsum (Section 975B-34X-2, 311.8 mbsf).

Summary

The facies transitions indicated by the progression from Unit III to Unit I are interpreted to represent a transgressive sequence that begins with the supratidal to intertidal, evaporative environment that produced the gypsiferous sediments of the Messinian (Unit III). The Unit II/III boundary marks the transition to an intertidal to shallow lagoonal setting (Unit II). The boundary between Unit II and Unit I represents the change to an open marine environment. In keeping with this pattern of deepening upsection, the gradual change from somewhat more pelagic conditions in the lower portions of Unit I to a more hemipelagic environment probably reflects a temporal increase in terrigenous influx rather than a change in proximity of the source.

BIOSTRATIGRAPHY

Calcareous Nannofossils: Abundance and Preservation

Cores recovered at Site 975 contain abundant, well-preserved Pleistocene to upper Miocene nannofossils. Exceptions are Samples 975A-1H-CC, 975B-1H-CC, 975B-34X-CC, and 975C-32X-CC, 33X-CC, and 34X-CC, wherein nannofossils are rare to common in abundance.

Biostratigraphy

Hole 975A

Only one core was taken in Hole 975A. Sample 975A-1H-CC contains *Emiliania huxleyi* and is assigned to Subzone NN21A.

Holes 975B, 975C, and 975D

Figures 27–29 show the zonal assignments of each core, respectively, in Holes 975B, 975C, and 975D, as well as the occurrence of species that define the zonal boundaries.

Hole 975B (Fig. 27)

The stratigraphic interval at this site ranges from uppermost Miocene (Zone NN12) to uppermost Pleistocene–Holocene (Subzone NN21B.) All zones and subzones within this sequence are determined except the Pleistocene Subzone NN19B/NN19C boundary.

The NN19A/NN19B boundary approximates the Pliocene/Pleistocene boundary (at 119.50 mbsf), the occurrence of the last common *Reticulofenestra pseudoumbilicus* approximates the lower/upper Pliocene boundary (at 233.66 mbsf), and the extinction of *Helicosphaera intermedia* in Zone NN12 approximates the Miocene/Pliocene boundary (at 307.26 mbsf). In this hole, the Pliocene/Pleistocene boundary is between Samples 975B-13H-CC (118.66 mbsf) and 14H-2, 75–77 cm (120.35 mbsf). The lower/upper Pliocene boundary is between Samples 975B-25X-6, 19–20 cm (231.49 mbsf), and 25X-CC (235.24 mbsf). The Miocene/Pliocene boundary is between Samples 975B-32X-CC (302.75 mbsf) and 33X-3, 130–131 cm (306.70 mbsf).

Hole 975C (Fig. 28)

Sediments in this hole range from lower Pliocene (Zone NN12/NN13 undifferentiated) to uppermost Pleistocene–Holocene (Subzone NN21B). Samples 975C-30X-CC to 34X-CC were assigned to undifferentiated Zone NN12/NN13 because no diagnostic marker species were found to separate the two zones.

The Pliocene/Pleistocene boundary NN19A/N19B was not accurately determined because of the low sampling resolution, and was placed between Samples 975C-13H-CC (117.10 mbsf) and 14H-CC (126.31 mbsf) at the mean depth of 121.70 mbsf. The lower/upper Pliocene boundary lies between Samples 975C-25X-CC (231.60 mbsf) and 26X-CC (240.79 mbsf).

Table 6. Summary of post-evaporite sediment recovered by drilling in the vicinity of Site 975.

Leg	Site	Location	Lithology	Environment	Reference
13	124	Balearic Rise	Dolomitic marls, in places finely interlaminated with terrigenous silt, and interbedded with dark, finely laminated sediment rich in pyrite and carbonaceous material	Shallow water, possibly stromatolitic	Ryan, Hsü, et al., 1973
13	132	Tyrrhenian Basin	Dolomitic marl and dark, pyritic, sandy marl ooze containing micritic calcite and dolomite	Shallow water, possibly stromatolitic	Ryan, Hsü, et al., 1973
13	134	Balearic Abyssal Plain	Dark dolomitic marl ooze laminated with marl ooze	Shallow water, possibly stromatolitic	Ryan, Hsü, et al., 1973
42A	372	Menorca Rise	Variegated, laminated, nannofossil dolomitic marl	Shallow water, possibly stromatolitic	Hsü, Montadert, et al., 1978
107	652	Tyrrhenian Sea	Variegated gypsiferous mudstones, siltstones, and sandstones with variable carbonate contents	Lacustrine	Kastens, Mascle, Auroux, et al., 1987
161	974	Tyrrhenian Sea	Variegated clay, calcareous silty clay, silt, and sand with normal grading and parallel and cross lamination	Lacustrine	Site 974 "Lithostratigraphy" section, this volume

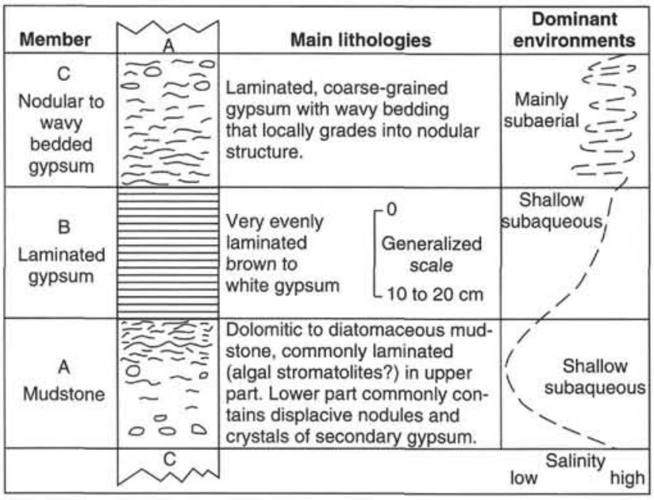

Figure 26. Model of facies transitions in a gypsum cycle (from Garrison et al., 1978).

Hole 975D (Fig. 29)

Sediments in this hole range from upper Pliocene (Zone NN17) to upper Pleistocene/Holocene (Zone NN21B). Subzones NN19B and NN19C were not separated. The Pliocene/Pleistocene boundary was placed between Samples 975D-12H-CC (112.46 mbsf) and 13H-CC (122 mbsf) at the mean depth of 117.23 mbsf.

Planktonic Foraminifers: Abundance and Preservation

Cores recovered contain abundant and well-preserved Pleistocene to lower Pliocene foraminiferal assemblages. Upper Miocene samples above gypsum layers contain poorly to moderately well-preserved foraminiferal assemblages that contain dwarfed, recrystallized, and fragmented specimens reflecting abnormal ecological conditions and subsequent diagenetic alteration. During this Miocene interval, the environment was stressed but some dwarfed planktonic and benthic foraminiferal forms occasionally survived.

Biostratigraphy

Biozones, the distribution of zonal markers, and sampling intervals are shown in Figures 30–32.

Hole 975A

A 9.5-m section was recovered from Hole 975A that overshot the sediment-water interface. Sample 975A-1H-CC yields an abundant assemblage that cannot be assigned to a defined biozone since the significant planktonic foraminiferal markers are missing. The most common species are *Globorotalia scitula* and *Globigerina falconensis.*

Hole 975B (Fig. 30)

A 299-m-thick upper Miocene–Pleistocene sequence was recovered in Hole 975B.

The Pleistocene interval is 108 m thick but only the *Globigerina cariacoensis* Zone was detected. *Globorotalia truncatulinoides excelsa,* the taxon used by stratigraphers to recognize the homonymous zone, was not observed. The Pliocene–Pleistocene boundary, which coincides with the MPL6/*G. cariacoensis* zonal boundary, occurs at Sample 975B-12H-CC (108.85 mbsf). All the biozones of the Pliocene sequence were recognized. From Sample 975B-33X-3, 80–82 cm (306.20 mbsf), down to the hole's total depth (314.13 mbsf), the foraminifers are characterized by dwarfed and poorly preserved assemblages common in the uppermost Miocene Mediterranean sediments (corresponding to the "Lago Mare" facies).

Hole 975C (Fig. 31)

A 307-m-thick upper Miocene–Pleistocene sequence was recovered in Hole 975C (Fig. 31). The Pleistocene interval was recovered from the seafloor to ~88 mbsf, and the Pliocene/Pleistocene boundary was placed between Samples 975C-13H-3, 160–162 cm, and 975C-13H-7, 49–51 cm. Both *G. truncatulinoides excelsa* and *G. cariacoensis* Zones were recognized. All the biozones of the Pliocene sequence were recognized. The base of Zone MPL6 was recognized in Sample 975C-14H-CC (126.26 mbsf). Sample 975C-33X-CC (306.82 mbsf) to sediment at the bottom of the hole contain a Messinian assemblage that indicates the *Globorotalia conomiozea* Zone. The most significant taxa are *G. conomiozea, G. mediterranea, G. miotumida, G. merotumida,* and *Neogloboquadrina acostaensis* (sinistral coiling).

Hole 975D (Fig. 32)

A 150-m-thick upper Pliocene–Pleistocene sequence was recorded in Hole 975D.

The Pleistocene interval and the Pliocene/Pleistocene boundary were not recognized since the markers were not detected. This interval is characterized by a monotonous assemblage in which *Globorotalia inflata, Globigerinoides ruber, Neogloboquadrina dutertrei* are at times dominant species. The base of Zone MPL6 was recognized in Sample 975D-13H-CC (122.00 mbsf). Samples 975D-14H-CC through 15H-CC, the latter of which yields common specimens of *Sphaeroidinella dehiscens,* were assigned to Zone MPL5b. However, rare specimens of *Globorotalia bononiensis–Globorotalia inflata* transitional forms occur in Sample 975D-15H-CC (140.98 mbsf), indicating that the top of Zone MPL5a is very close to this sample.

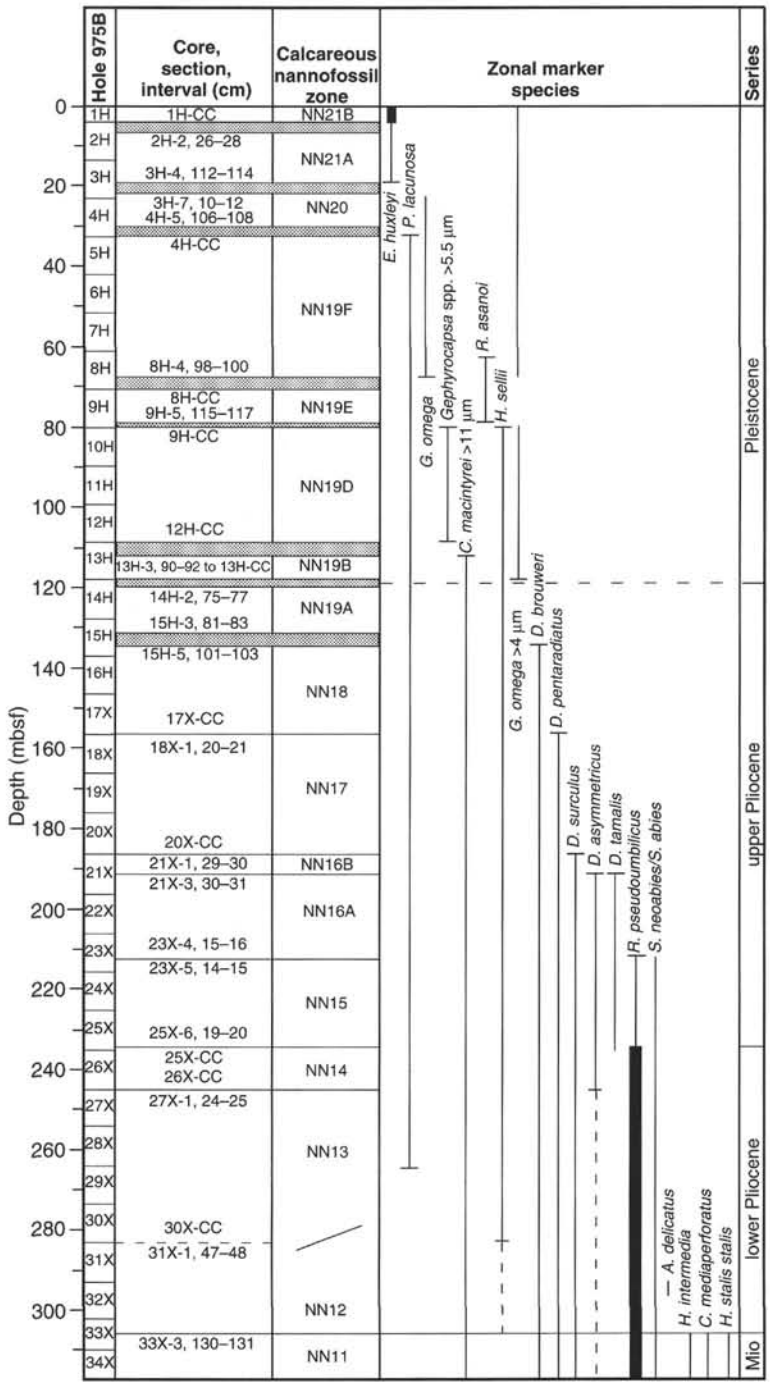

Figure 27. Calcareous nannofossil zonation of Hole 975B. Bold lines represent acme intervals. Lack of a short horizontal line at the end of a species' vertical range line indicates that the range of that species is incomplete. Dashed vertical lines below the Mediterranean bases of *H. sellii* and *D. asymmetricus* indicate their irregular occurrences elsewhere. Shaded areas represent intervals not sampled. Missing zones or subzones do not imply hiatuses. The zones/subzones may be in sections not yet examined.

Benthic Foraminifers

Benthic foraminifers in Site 975 (present-day water depth of 2415 m) generally compose <1% of the total foraminiferal assemblage in most of the examined samples. Relative to the previous deeper Site 974 (present-day water depth of 3459 m), their size and presence is much greater, and they are much more diverse. The most recurrent forms are various species of lagenids, deep miliolids (e.g., *Pyrgo* spp. and *Articulina tubulosa*), *Cibicidoides kullenbergi, Cibicides* spp., *Cassidulina neocarinata, Gyroidina* spp., *Siphonina reticulata, Hyalinea balthica, Planulina wuellerstorfi, Gyroidina laevigata, Pullenia quinqueloba,* and *Oridorsalis stellatus,* which indicate an upper to middle bathyal environment. Occasional evidence exists for downslope contamination by shelf taxa that are often abraded and mixed with deeper water assemblages. *Bulimina aculeata* is common in Sample 975D-3H-CC, and *Pyrgo murrhina* in Sample 975D-4H-CC. In Sample 975B-7H-CC, rare specimens of *Hyalinea balthica* are present. *Globobulimina affinis* in Sample 975B-5H-CC and *El-*

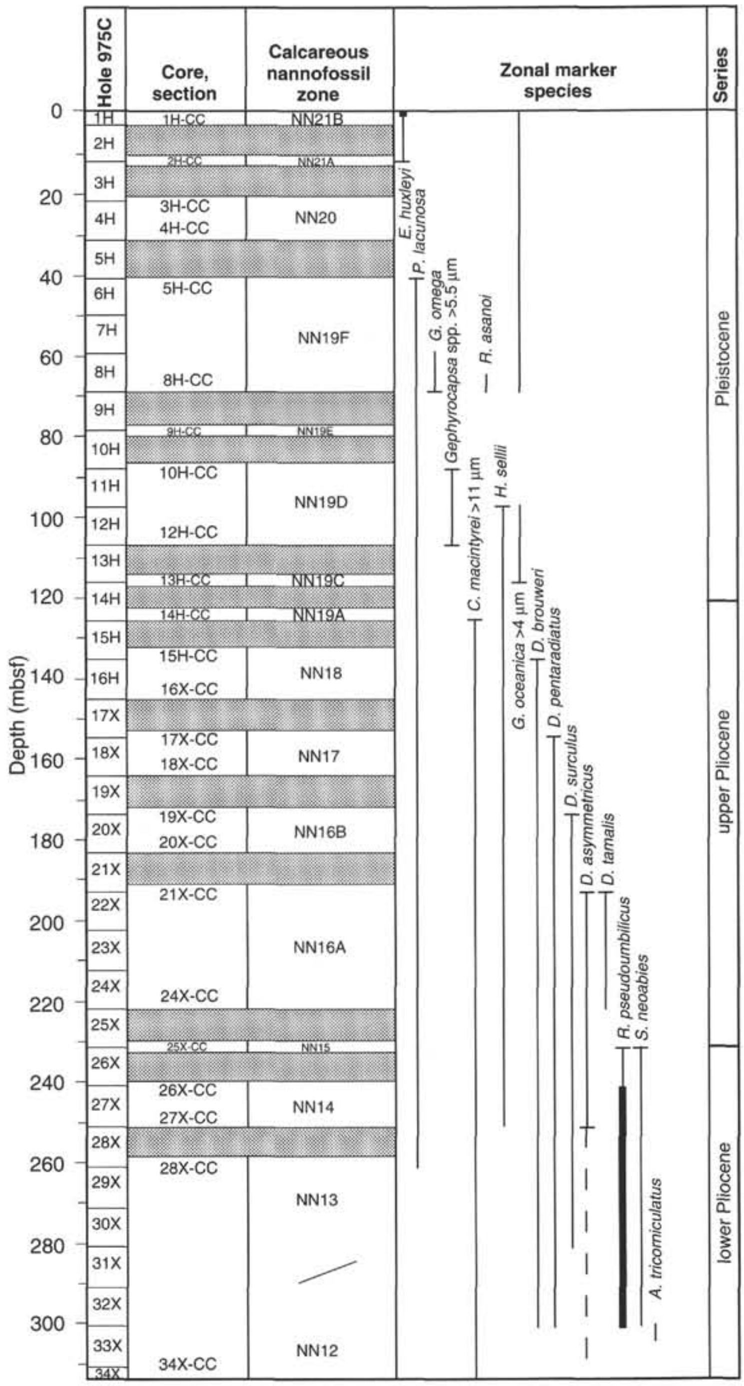

Figure 28. Calcareous nannofossil zonation of Hole 975C (see Fig. 27 caption for details).

phidium spp. in Sample 975B-26X-CC indicate displacement from the inner shelf. A few specimens of *Ammonia tepida* in Sample 975B-33X-CC (302.7 mbsf) suggest a brackish water environment, which is typical of the "Lago Mare" facies.

Biozonal Correlation

Correlation of the calcareous nannofossil and planktonic foraminiferal zonations is shown in Figure 33. Discrepancies between the depth distribution of some biozones in the different holes could be caused by correlation problems between the two groups of fossils or because of limited sampling resolution.

The placement of the Pliocene/Pleistocene boundary is based on the calcareous nannofossils, the Miocene/Pliocene boundary on the planktonic foraminifers, and the lower/upper Pliocene boundary on both groups of microfossils.

Paleoecology

The calcareous nannofossil assemblage in all holes at this site is typical of normal open-ocean conditions with the exception of an in-

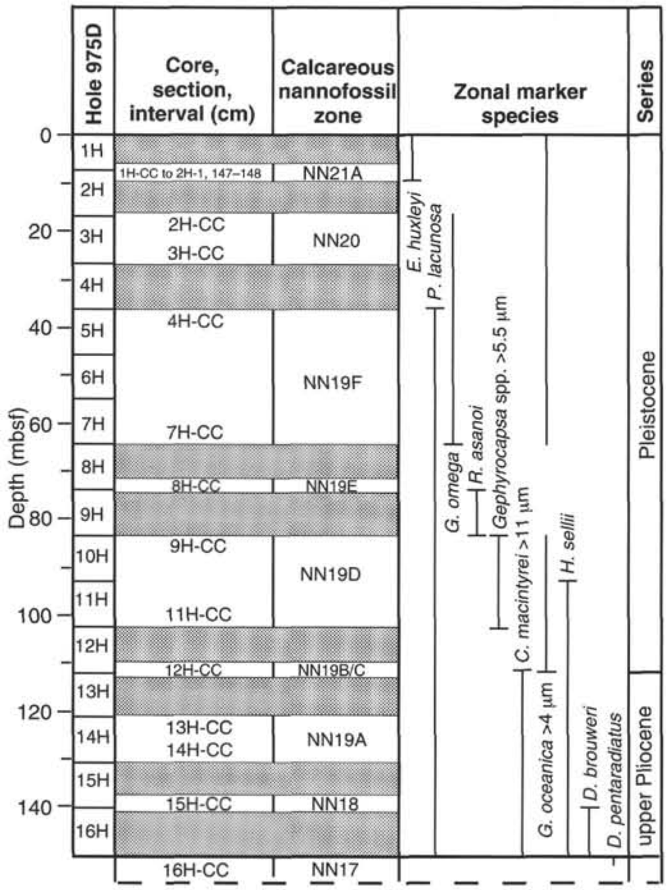

Figure 29. Calcareous nannofossil zonation of Hole 975D (see Fig. 27 caption for details).

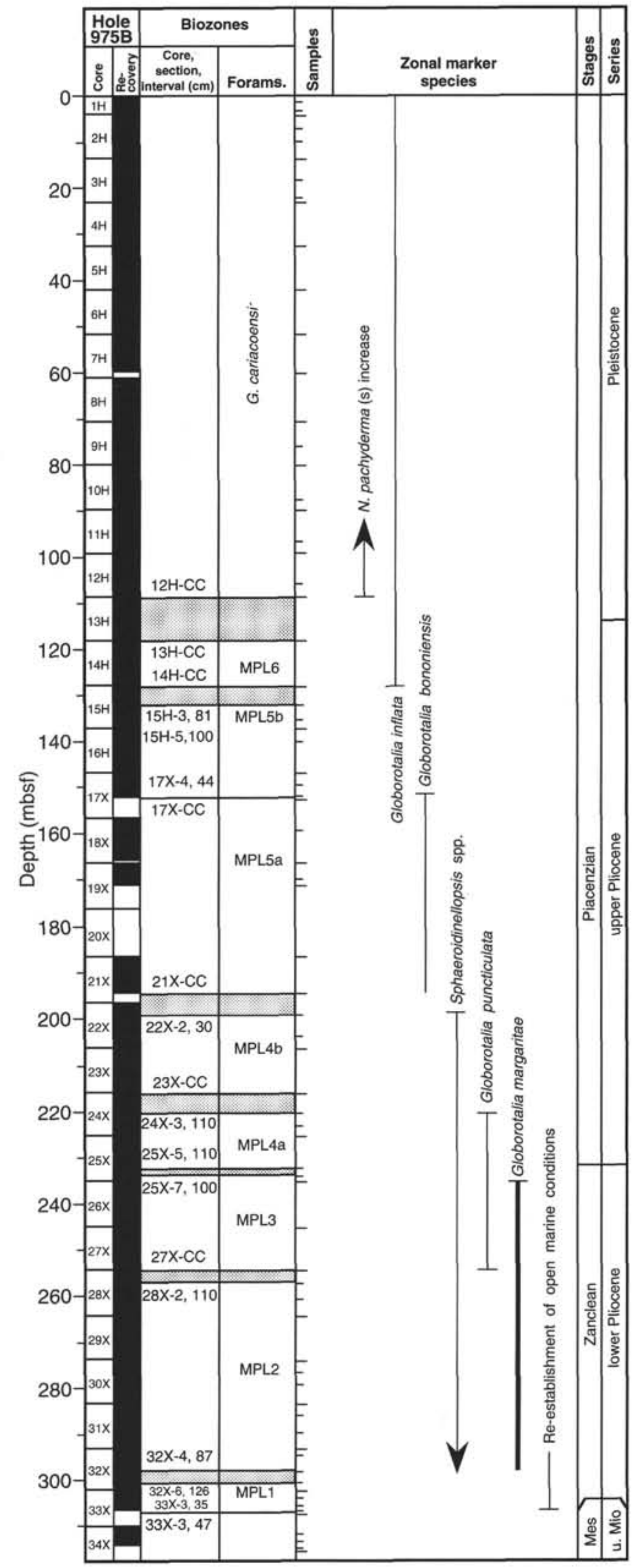

Figure 30. Planktonic foraminiferal zonation of Hole 975B. Shaded areas represent intervals not sampled.

terval in Core 975B-13H, 118.66 mbsf (lowermost Pleistocene, Subzone NN19B). In fact Samples975B-13H-CC, 975B-13H-3, 90–92 cm (112.50 mbsf), and 975B-13H-6, 45–47 cm (116.55 mbsf) contain a prolific "*Braarudosphaera* bloom" in which *Braarudosphaera bigelowii* makes up an estimated 20% (by volume) of the core catcher sample, 40% of Sample 975B-13H-3, 90–92 cm, and 60% of 975B-13H-6, 45–47 cm. Moreover, common specimens of *B. bigelowii* in these samples are considerably larger (18–20 μm) than the normal size of *B. bigelowii* (10–14 μm) (Siesser et al., 1992.)

This bloom of *B. bigelowii* probably signals unusual oceanographic conditions. In today's oceans, *B. bigelowii* prefers low-salinity, nearshore waters and is rarely found in the open ocean (Siesser et al., 1992), and thus it is rare in pelagic sediments. Only rare or few *B. bigelowii* are usually found during routine examination of slides made from Cenozoic or Cretaceous open-ocean sediments (this is also true in all samples examined so far from Holes 974A through 974D and 975A through 975D, with the exception of the samples noted above). Because of this, it has been difficult to explain the occurrence of the Oligocene "*Braarudosphaera* Chalk" deposited under apparently open-ocean conditions in the South Atlantic and elsewhere. Attempts to explain these unusual blooms have focused on injection of low-salinity waters, with or without specific nutrient additions, as the triggering mechanism (Siesser et al., 1992).

Other reports of this phenomenon in the Mediterranean have been made by Müller (1978; 1990), who noted similar *Braarudosphaera*-rich sediments at Sites 371, 651, 652, 653, 654, and 655. Moreover, these blooms were also found in Zone NN19, with additional blooms in Zone NN17/NN18 at Site 651 and 653.

Planktonic foraminiferal assemblages are also typical of open-ocean conditions. Benthic foraminifers provide some insights into

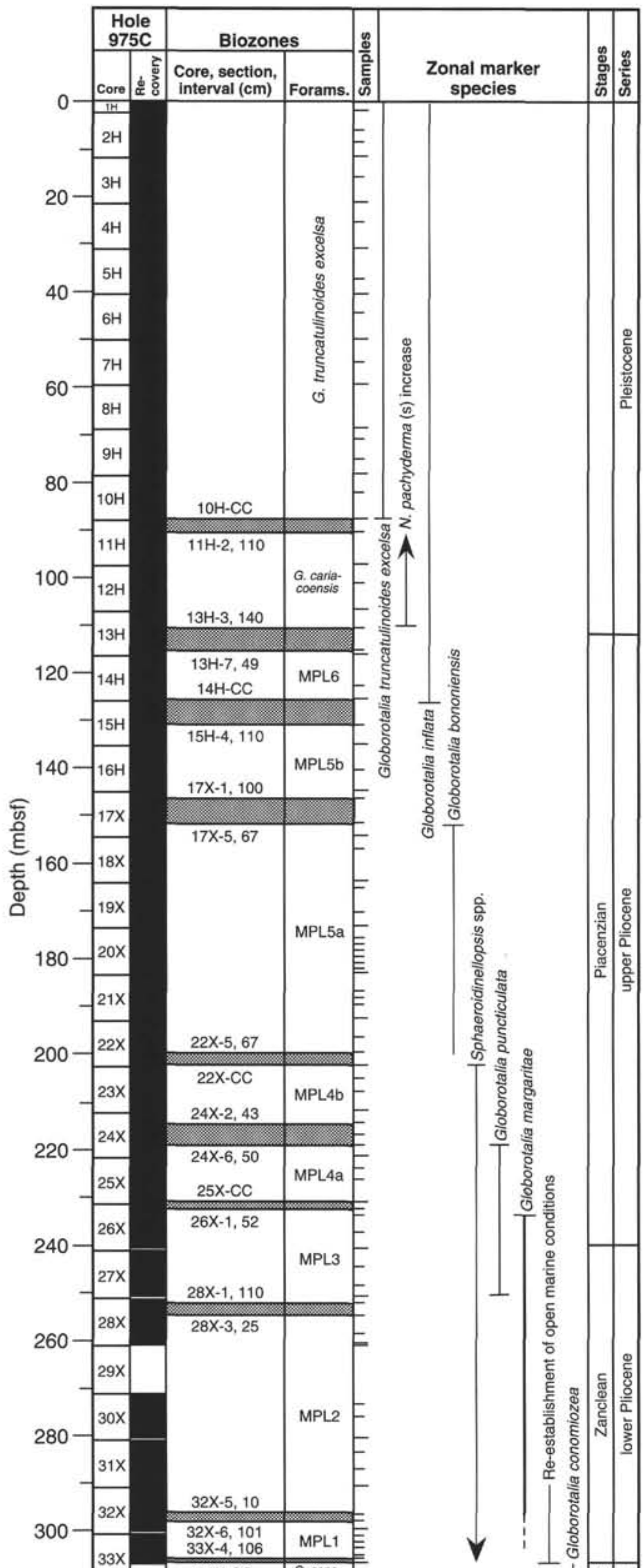

Figure 31. Planktonic foraminiferal zonation of Hole 975C. Shaded areas represent intervals not sampled.

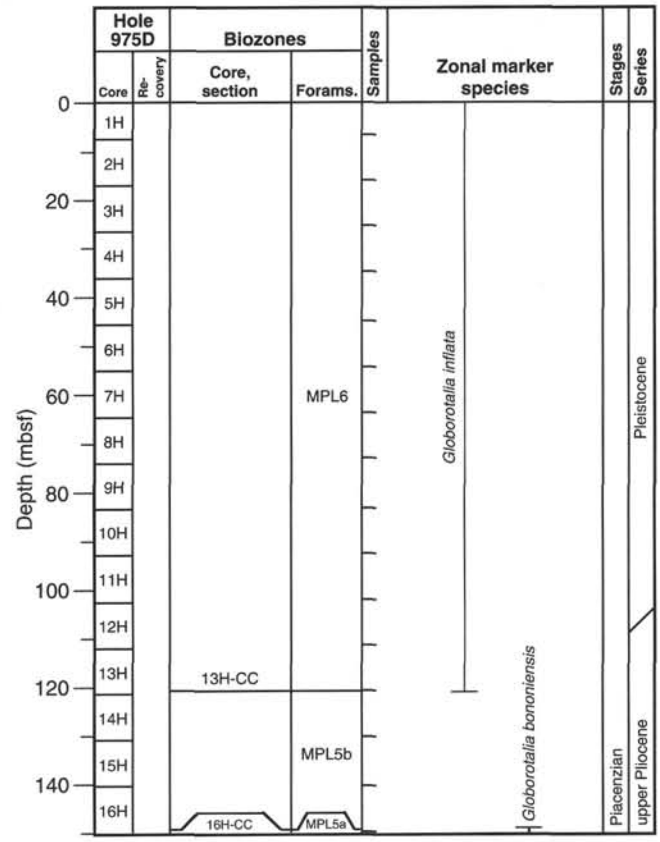

Figure 32. Planktonic foraminiferal zonation of Hole 975D.

seafloor conditions. Except for the Messinian sequence that was penetrated at the bottom of the site, sediments at Site 975 were deposited in upper to middle bathyal depths. Occasional sedimentologic and faunal evidence exists for reworking from shallow-water environments. Supplemental samples for shipboard analyses generally avoided sampling in these intervals.

The "Lago Mare" facies (Hsü, Montadert, et al., 1978) consists of sediments deposited in brackish environments, which are spread diffusely around the eastern Mediterranean. These deposits are well known to characterize the uppermost Messinian sequence of Mediterranean land sections. Usually they contain an *Ammonia-Cyprideis* fauna associated with lacustrine gastropods. The presence of *Ammonia tepida* in Sample 975B-33X-CC (302.7 mbsf) suggests that lithostratigraphic Unit II (see "Lithostratigraphy" chapter, this volume) may be a western Mediterranean equivalent of the "Lago Mare" facies found in other parts of the Mediterranean.

Sedimentation Rates

Sedimentation rates for Hole 975B are shown in Figure 34. Age data used (Table 7) for construction of the plot are based on FO, LO, FCO, and LCO events of selected nannofossils and planktonic foraminifers (see Table 2, "Explanatory Notes" chapter, this volume). Average sedimentation rates in Hole 975B were 68.28 m/m.y for the Pleistocene/Holocene, 48.9 m/m.y. for the upper Pliocene, and 53.8 m/m.y. for the lower Pliocene. These rates are uncorrected for compaction.

PALEOMAGNETISM

Eighty-five APC and XCB archive halves from Site 975 were measured with the cryogenic magnetometer. Natural remanent mag-

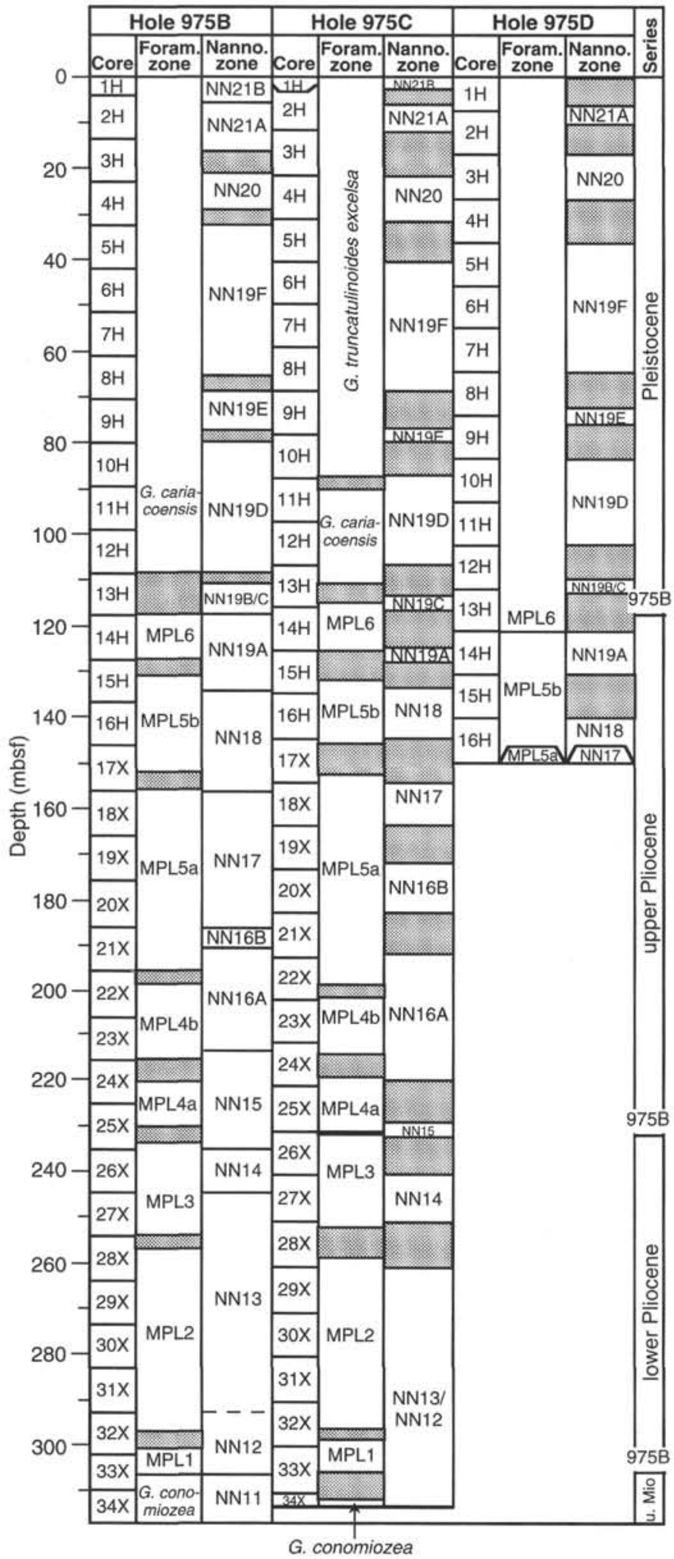

Figure 33. Summary of nannofossil and foraminiferal zonations of Holes 975B–975D.

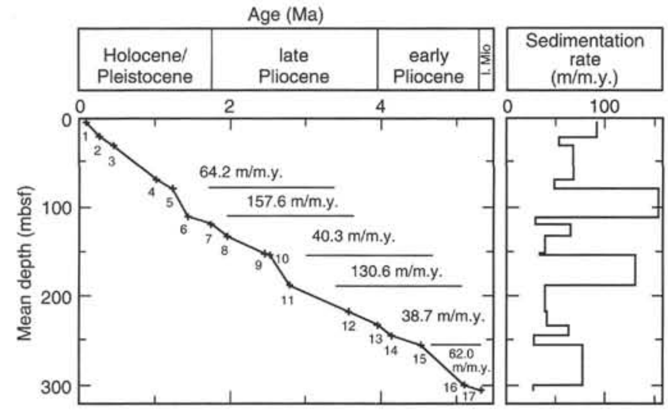

Figure 34. Age-depth function and sedimentation rates at Hole 975B.

Table 7. Age of calcareous nannofossil and planktonic foraminiferal biostratigraphic events and depths of their occurrence in Hole 975B.

		Biostratigraphic event	Age (Ma)	Depth (mbsf) Top	Bottom	Mean
1	FO	*E. huxleyi* acme	0.085	4.16	5.86	5.01
2	FO	*E. huxleyi*	0.26	19.22	22.70	20.96
3	LO	*P. lacunosa*	0.46	30.16	32.75	31.46
4	FO	*G. omega* >4.0 µm	1.02	66.58	70.91	68.75
5	LO	*Gephyrocapsa* spp. >5.5 µm	1.24	77.75	80.56	79.16
6	FO	*Gephyrocapsa* spp. >5.5 µm	1.44	108.85	112.50	110.68
7	FO	*G. oceanica* >4.0 µm	1.75	118.66	120.35	119.51
8	LO	*D. brouweri*	1.96	131.41	134.61	133.01
9	LO	*G. bononiensis*	2.45	151.54	152.35	151.95
10	LO	*D. pentaradiatus*	2.52	152.00	156.50	154.25
11	LO	*D. tamalis*	2.78	186.69	189.70	188.20
12	LO	*G. puncticulata*	3.57	216.09	220.00	218.05
13	LCO	*G. margaritae*	3.94	231.49	234.39	232.94
14	FCO	*D. asymmetricus*	4.13	244.58	245.05	244.82
15	FO	*G. puncticulata*	4.52	254.06	257.10	255.58
16	FCO	*G. margaritae*	5.10	298.17	301.56	299.87
17		Re-establishment of open-marine conditions	5.33	305.75	305.87	305.81

Notes: FO = first occurrence, LO = last occurrence, LCO = last common occurrence, FCO = first common occurrence.

Table 8. Azimuthal orientation of APC cores from Hole 975B using Tensor tool data.

Core	Magnetic toolface (MTF) (°)
161-975B-	
3H	124
4H	181
5H	63
6H	348
7H	51
8H	225
9H	248
10H	122
11H	149
12H	238
13H	236
14H	194
15H	234
16H	228

Notes: Cores 974B-3H to 17H were oriented. The orientation parameter (MFT) is an angle between true north and X-axis of the core-coordinate.

netizations (NRM) and remanences after alternating field (AF) demagnetization at 25 mT were measured every 10 cm. Some discrete samples were measured with the spinner magnetometer for rock-magnetic analysis. The Tensor tool provided core orientations in Hole 975B (Table 8). As at Site 974, magnetostratigraphic interpretation was not very successful.

Characteristics of the Overprinting

Strong overprinting hindered determination of primary magnetization (Fig. 35–38). This overprint is characterized by:

1. high intensity of magnetization. NRM intensities have a median of 50 mA/m (APC and XCB cores) except lithostratigraphic

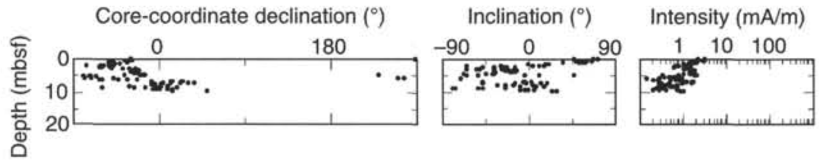

Figure 35. Pass-through remanent magnetization measurements from Hole 975A after AF demagnetization at 25 mT.

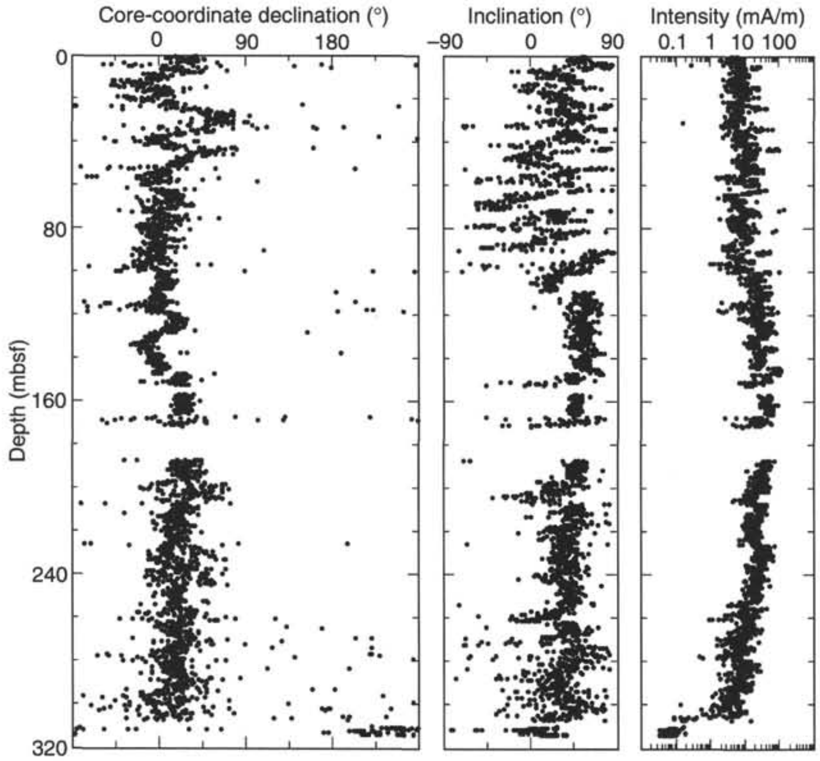

Figure 36. Pass-through measurements of archive halves from Hole 975B after AF demagnetization at 25 mT.

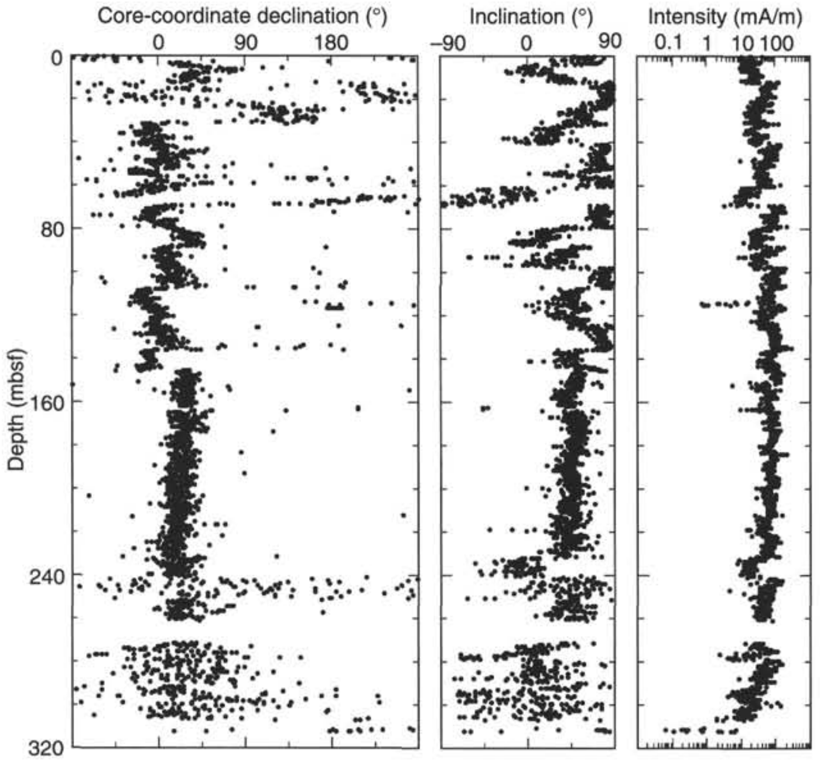

Figure 37. Pass-through measurements from Hole 975C after AF demagnetization at 25 mT

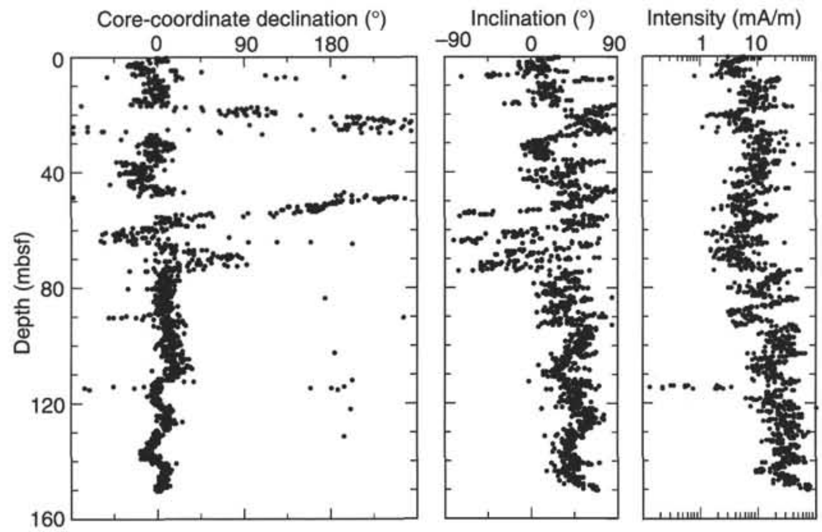

Figure 38. Pass-through measurements of archive halves from Hole 975D after AF demagnetization at 25 mT.

Units II and III where intensity decreases to about 0.1 mA/m. After demagnetization at 25 mT, intensities decrease to about 20% of the NRM.

2. predominance of positive inclinations close to the present field (60°), and occasionally vertical (90°). After demagnetization up to 25 mT, several intervals with shallow and negative inclinations are observed (Fig. 35–38).
3. pervasive radial remagnetization (PRR; Leg 154 Shipboard Scientific Party, 1995). The declination is perpendicular to the split surface in archive and working halves. Below 140 mbsf, in XCB cores, declination is at 20° to the X-axis despite strong core biscuiting.

Rock-Magnetic Properties

We sampled three discrete cubes to investigate rock-magnetic differences. Sample 975C-1H-1, 32–34 cm, was collected from a silty clay layer of moderate yellowish brown color (10YR 5/4) and is assumed to reflect seafloor oxidizing conditions. Samples 975C-1H-1, 121–123 cm (light olive gray, 5Y 5/2) and 975C-3H-4, 105–107 cm (olive-gray ooze, 5Y 4/1) have typical colors of Unit I (see "Lithostratigraphy" section, this chapter).

The values of $S_{-0.3T}$ parameters (0.98 ± 0.01; see "Explanatory Notes" chapter, this volume) for the samples indicate the absence of highly coercive magnetic minerals like hematite or goethite. Comparison between stepwise AF demagnetization curves of anhysteretic remanent magnetization (ARM) and saturated IRM (modified Lowrie-Fuller test; Johnson et al., 1975) are shown in Figure 39. For Samples 975C-1H-1, 121–123 cm, and 975B-3H-4, 105–107 cm, IRM is always less coercive than ARM. This suggests that magnetic minerals in the samples are single-domain or pseudo-single domain. Contrary to this, ARM is less coercive for Sample 975C-1H-1, 32–34 cm, which implies dominance of multidomain states or contamination from superparamagnetic grains (Heider et al., 1992). Thus, contamination of very fine superparamagnetic grains formed by surface diagenesis is plausible for the upper part of the core.

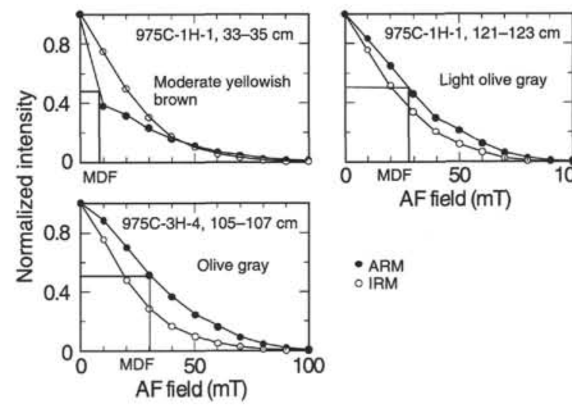

Figure 39. Stepwise AF demagnetization curves of ARM and saturated IRM (modified Lowrie-Fuller test).

Magnetostratigraphy

Two intervals of shallow and negative inclinations are observed (Fig. 40) between 25 and 45 mbsf and between 50 and 100 mbsf. Shallow inclinations may indicate insufficient demagnetization to reveal negative inclination (e.g., from 80 to 100 mbsf in Hole 975D). In addition, a short interval of negative inclination is found at about 10 mbsf. If the negative inclination at 10 mbsf is not a drilling- or coring-induced artifact, it may be a short reversed interval (about 0.1 Ma) just beneath the seafloor.

According to biostratigraphic data, the negative inclinations found in the interval between 25 and 45 mbsf cannot be correlated to the Brunhes/Matuyama (B/M) boundary, because the last occurrence of the zonal marker, *P. lacunosa* (0.46 Ma) is at 23–32 mbsf (Hole 975B). The Matuyama chron probably ends at the top of the second reversal interval at about 50 mbsf, which is in close agreement with the biostratigraphic data.

Magnetic Susceptibility and Sapropel Horizons

Some sapropel horizons are plotted with respect to the low-field magnetic susceptibility data (Figure 41). The magnetic susceptibility signal is similar from hole to hole and sapropels mostly correspond to low susceptibilities below a peak in susceptibility. In contrast, one sapropel, Section 975B-6H-4, is characterized by a small susceptibility peak within a zone of low susceptibility. This susceptibility peak is followed by a decrease that may reflect the redox conditions during deposition of sapropels and possibly post-depositional diagenesis. Since sources of low-field susceptibility could be due to multiple causes (mineralogy, content, and grain size of ferrimagnetic minerals, but also clay content), it appears that further rock-magnetic studies in the sapropel horizons will contribute to understanding potential relationships between sapropel deposition and magnetic susceptibility.

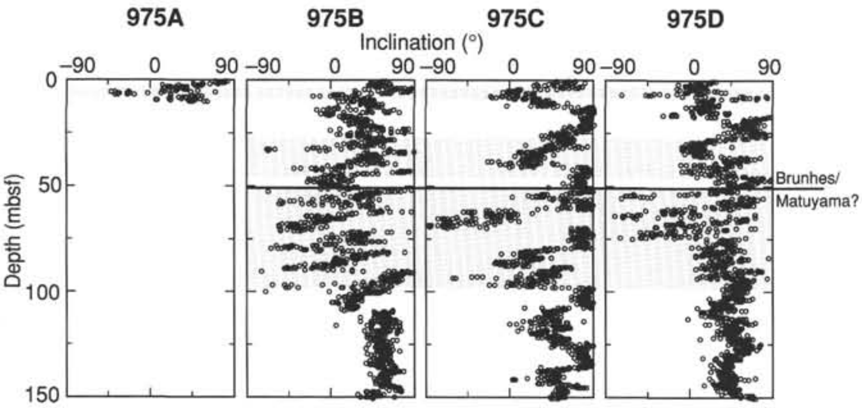

Figure 40. Correlation of inclination among Holes (975A to 975D) after AF demagnetization at 25 mT. Negative and shallow inclinations (shadow bands) are found at three horizons throughout holes.

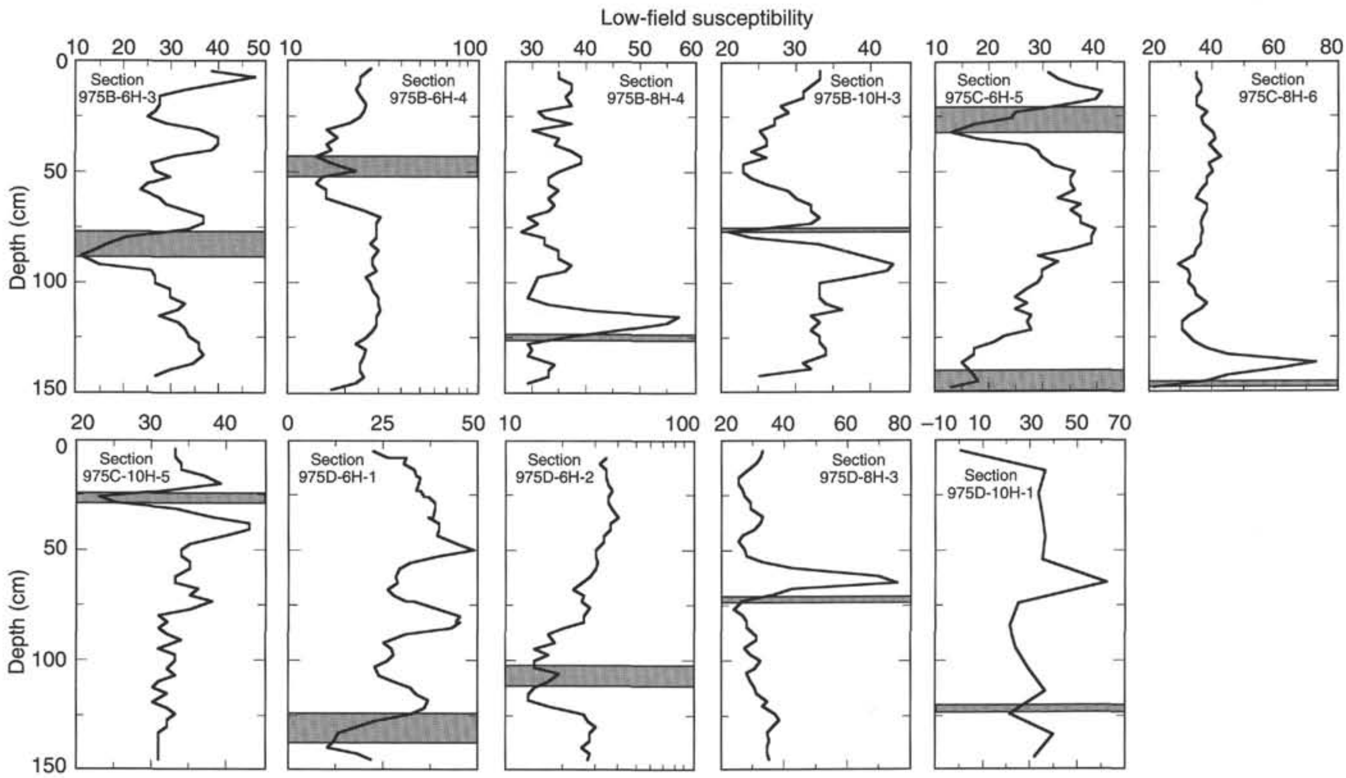

Figure 41. Comparison between sapropel occurrence (shaded zone) and low-field magnetic susceptibility in core sections measured on MST. To convert the susceptibility value into SI units, multiply 0.63×10^{-5} to the horizontal axes.

COMPOSITE DEPTHS

High-resolution (2–10-cm-scale) data were collected on the multisensor track (MST) and with a handheld spectrophotometer on cores recovered from all holes of Site 975. Three principal variables (GRAPE density, magnetic susceptibility, and 550-nm-wavelength color reflectance) were used to construct a composite depth section from Holes 975B, 975C, and 975D to 135 mbsf. Distinctive features were correlated between cores from each hole and depth-shifted to a common depth scale (meters composite depth = mcd) so that overlapped cores from different holes would produce a single composite section. The offsets for each core used for alignment are listed in Table 9, which gives standard ODP meters below seafloor depths (mbsf), offset in meters, and the composite depth for each core (mcd). Shifted and aligned core data are shown in Figures 42 and 43.

The composite (or "spliced") section seeks to provide a complete stratigraphic record utilizing overlapping intervals of cores from the different holes. The composite section is described in Table 10. Splices from Table 10 are indicated by arrows in Figure 42. Correlation between cores was consistent between the seafloor and approximately 135 mbsf. Below this depth a continuous record could not be constructed with confidence. Individual pairs of cores from Holes 975B and 975C have been tied together where possible in the lower parts of the holes.

STRUCTURAL GEOLOGY

The Pleistocene and Pliocene sediments cored at Site 975 are unconsolidated or poorly consolidated clay, silt, and marly ooze, which show considerable drilling-induced deformation, including zones of downward drag about 1 cm on each side of the APC cores, and "biscuit" structure in the XCB cores. The only consolidated material is the latest Miocene evaporitic sequence at the bottom of the hole.

The dip of bedding is close to horizontal throughout all four holes at Site 975, apart from meter-scale changes due to slumping. A 1-m

Table 9. Composite depth table for Holes 975A, 975B, 975C, and 975D.

Core	Depth (mbsf)	Offset (m)	Depth (mcd)	Comment
161-975A-				
1H	0.00	2.60	2.60	
161-975B-				
1H	0.00	0.00	0.00	
2H	4.10	1.73	5.83	
3H	13.60	1.50	15.10	
4H	23.10	2.85	25.95	
5H	32.60	3.75	36.35	
6H	42.10	4.90	47.00	
7H	51.60	4.75	56.35	
8H	61.10	6.40	67.50	
9H	70.60	6.31	76.91	
10H	80.10	6.80	86.90	
11H	89.60	6.55	96.15	
12H	99.10	6.87	105.97	
13H	108.60	7.70	116.30	
14H	118.10	9.04	127.14	
15H	127.60	8.99	136.59	
16H	137.10	7.91	145.01	
17X	146.60	7.51	154.11	
18X	156.30	7.51	163.81	
19X	166.30	7.51	173.81	1
20X	176.40	7.51	183.91	1
21X	186.40	7.51	193.91	1
22X	196.20	7.51	203.71	1
23X	206.20	7.51	213.71	1
24X	215.90	7.51	223.41	1
25X	225.40	8.32	233.72	1
26X	235.10	7.61	242.71	2
27X	244.80	8.32	253.12	2
28X	254.50	8.32	262.82	2
29X	264.10	8.32	272.42	1
30X	273.60	8.32	281.92	1
31X	283.30	9.59	292.89	1
32X	292.80	9.59	302.39	2
33X	302.40	9.59	311.99	1
34X	310.00	9.59	319.59	1
161-975C-				
1H	0.00	0.00	0.00	
2H	2.40	0.95	3.35	
3H	11.90	1.91	13.81	
4H	21.40	2.36	23.76	
5H	30.90	3.20	34.10	
6H	40.40	4.15	44.55	
7H	49.90	4.37	54.27	
8H	59.40	4.87	64.27	
9H	68.90	5.20	74.10	
10H	78.40	5.83	84.23	
11H	87.90	5.71	93.61	
12H	97.40	6.39	103.79	
13H	106.90	6.97	113.87	
14H	116.40	7.80	124.20	
15H	125.90	7.80	133.70	1
16H	135.40	7.80	143.20	1
17X	144.90	7.80	152.70	1
18X	154.40	7.80	162.20	1
19X	164.10	7.80	171.90	1
20X	173.70	7.80	181.50	1
21X	183.40	7.80	191.20	1
22X	192.90	7.80	200.70	1
23X	202.50	7.80	210.30	1
24X	212.20	7.80	220.00	1
25X	221.70	7.80	229.50	1
26X	231.40	7.80	239.20	1
27X	241.00	7.80	248.80	1
28X	251.00	7.80	258.80	1
29X	261.00	7.80	268.80	1
30X	270.90	7.80	278.70	1
31X	280.80	7.80	288.60	1
32X	290.80	7.80	298.60	1
33X	300.70	7.80	308.50	1
34X	310.70	7.80	318.50	1
161-975D-				
1H	0.00	0.00	0.00	
2H	7.40	1.23	8.63	
3H	16.90	1.80	18.70	
4H	26.40	2.59	28.99	
5H	35.90	3.38	39.28	
6H	45.40	4.05	49.45	
7H	54.90	4.51	59.41	
8H	64.40	5.10	69.50	
9H	73.90	5.42	79.32	
10H	83.40	5.80	89.20	
11H	92.90	5.97	98.87	
12H	102.40	6.58	108.98	
13H	111.90	6.88	118.78	
14H	121.40	7.26	128.66	
15H	130.90	7.08	137.98	
16H	140.40	12.26	152.66	

Notes: 1 = offset carried from core above due to poor overlap. 2 = Hole 975B core adjusted to match Hole 975C. Adding offset to meters below seafloor (mbsf) within each core will produce meters composite depth (mcd).

slump fold occurs at 113.5–114.5 mbsf (Section 975B-33X-3) in Hole 975B (Fig. 11), as part of an east-facing fold-pair (core coordinates), and a 2-m slump fold associated with a reverse-sense shear occurs at 143 mbsf (Section 975B-16H-5). A minor reverse fault at 85.6 mbsf (Section 975B-10H-4; Fig. 44) is also probably a result of soft-sediment sliding. Slumping may have been related to the very gentle east-northeast dip of the entire Neogene and Pleistocene sequence, visible in seismic profiles across this site (see "Background and Objectives" section, this chapter).

Steeply dipping conjugate fractures in laminated shale and anhydrite at 305.6 mbsf (Section 975B-33X-3) in Hole 975B appear to have been affected by pressure-solution, producing stylolites (Fig. 45); very similar vertical stylolites are visible at exactly the same level in Hole 975C. Brittle boudins occur in a sand layer within anhydrite at 306.4 mbsf (Section 975B-33X-3; Fig. 46). Neither of these features are likely to have any regional tectonic significance.

The lack of tectonic deformation and the paucity of slump structures, compared with those seen at Site 974, suggest that Site 975 was tectonically inactive during Pliocene and Pleistocene times. The pinch-out of Messinian reflectors towards the acoustic basement high to the south-southeast of Site 975 visible on seismic profile Bal-9 (see "Background and Objectives" section, this chapter) shows that this high already existed by Messinian times.

ORGANIC GEOCHEMISTRY

Calcium carbonate and organic carbon concentrations were measured on samples obtained regularly from Holes 975B and 975C. Organic matter atomic C/N ratios and Rock-Eval analyses were employed to determine the type of organic matter contained within the sediments. Analyses of extractable methyl alkenones yielded estimates of sea-surface paleotemperatures, and GHM pyrolyses provided further information about organic matter character. Routine monitoring of headspace gas contents was done for drilling safety.

Inorganic and Organic Carbon Concentrations

Concentrations of carbonate carbon vary between 2.8% and 11% in sediments from Site 975 (Table 11). These carbonate carbon concentrations are equivalent to 23%-91% sedimentary $CaCO_3$, assuming that all of the carbonate is present as pure calcite. The range in carbonate content reflects varying combinations of biological productivity, dilution by non-carbonate hemipelagic sedimentary components, and post-depositional carbonate dissolution driven by oxidation of organic matter.

Fifteen sapropels, defined in this section as containing at least 1% TOC (Total Organic Carbon; note that this definition of a sapropel is different from that of an organic-rich layer given in the "Lithostratigraphy" section, this chapter), occur in Hole 975B (Fig. 47). Sample 975B-6H-3, 81–82 cm (45.91 mbsf), contains the maximum of 2.8% TOC (Table 11). Fourteen sapropels, as defined here, were identified in Hole 975C at sub-bottom depths comparable to the sapropel occurrences in Hole 975B (Fig. 47). Partial post-depositional oxidation of the organic matter content of the sapropels is suggested by their $CaCO_3$ content, which is generally lower than that of background sediments. This factor may have contributed to lowering the average $CaCO_3$ concentration of the upper 150 m of lithostratigraphic Unit I,

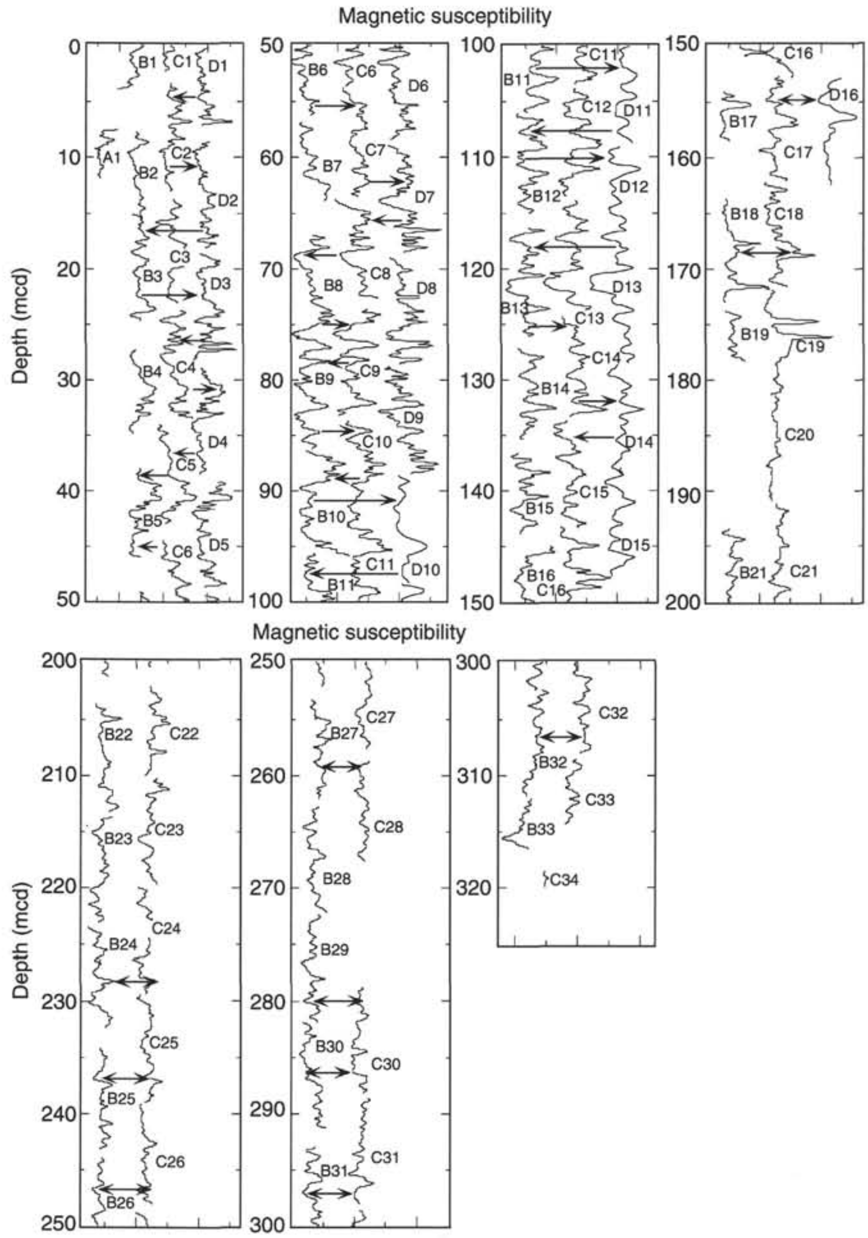

Figure 42. Site 975 magnetic susceptibility data for each hole plotted vs. meters composite depth (mcd) with tie lines used to construct composite depth section (single-ended arrows) and ties between individual cores (double-ended arrows).

relative to the lower 150 m in which sapropels are absent (Fig. 47). Another possible factor is diminished biogenic carbonate production during times of sapropel deposition. Dilution of carbonate content by clastic hemipelagic sediment components is also possible, but this process would dilute organic matter content and thereby diminish sapropel development.

Organic Matter Source Characterization

Organic C/N ratios were calculated using TOC and total nitrogen concentrations to help identify the origin of the organic matter (Table 11). The C/N ratios of sapropels average 12.3, a value that is intermediate between unaltered algal organic matter and fresh land-plant material (e.g., Emerson and Hedges, 1988; Meyers, 1994). Because diagenesis rarely depresses land-plant C/N ratios to values as low as those found in the sapropels, it is likely that these organic-carbon–rich sediments contain algal material that has been partially degraded during settling to the seafloor. Preferential loss of nitrogen-rich, proteinaceous matter can elevate the C/N ratios of algal organic matter by this process.

The C/N values of many background samples low in TOC are very low (<5). These values are probably an artifact of the low carbon content combined with the tendency of clay minerals to absorb ammonium ions generated during the degradation of organic matter (Müller, 1977). The C/N ratios of background samples especially low in organic carbon consequently are not accurate indicators of their organic matter source.

The results of Rock-Eval analyses of selected Site 975 sediments suggest that their organic matter content is a mixture of partially oxidized Type II algal material and Type III land-plant material (Fig. 48). Well-preserved Type II organic matter has high HI values (Espitalié et al., 1977). In general, Site 975 sediments with higher TOC concentrations also have higher HI values (Fig. 49), which is a pattern also found in sapropels in the eastern Mediterranean (Emeis, Robertson, Richter, et al., 1996). This relationship, combined with the average C/N value of 12.3, indicates that the original source of the organic matter was probably algal debris that has subsequently been oxidized. The inverse relationship between TOC and degree of oxidation is consistent with preservation being important in elevating the organic matter contents of Mediterranean sapropels (e.g., Cheddadi

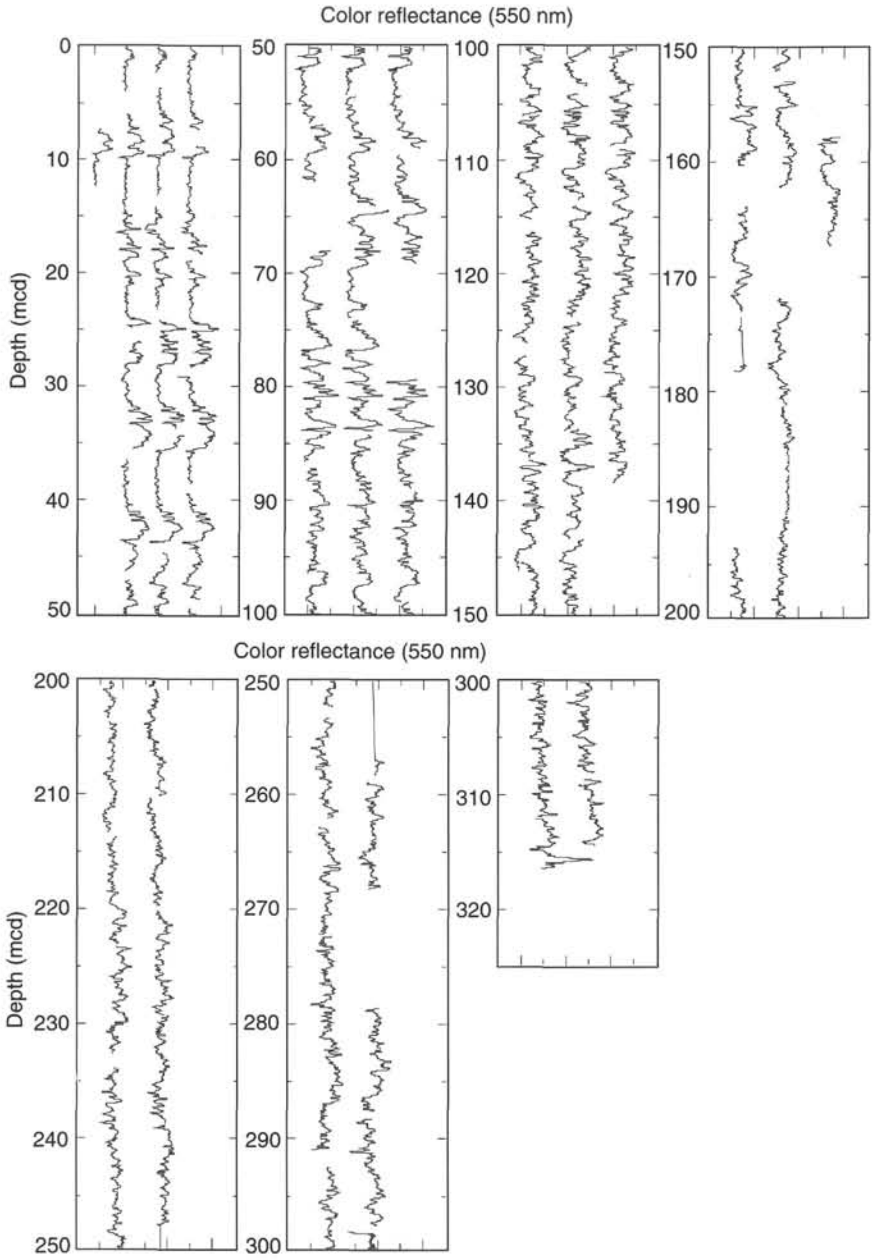

Figure 43. Site 975 550-nm color reflectance for each hole plotted vs. meters composite depth (mcd).

and Rossignol-Strick, 1995). T_{max} values are relatively low (Table 12), showing that organic matter is thermally immature with respect to petroleum generation (Espitalié et al, 1977).

Alkenone Paleotemperature Estimates

Samples containing at least 1% TOC were selected from Hole 975B for extraction and analysis of their C_{37} alkenone biomarkers and calculation of sea-surface paleotemperatures. The calculated paleotemperatures (Table 13) must be considered preliminary because of the limitations of shipboard analytical capabilities. Moreover, $U^{k'}_{37}$ values are converted to temperatures by comparison to *Emiliania huxleyi,* which has been extant for ~250,000 yr; paleotemperatures calculated for sediments older than this must be considered relative rather than absolute.

Sea-surface paleotemperatures have fluctuated over a 7°C range in the Balearic Sea during the Pleistocene (Fig. 50). A similar record of fluctuating paleotemperatures has been reported from the eastern Mediterranean (Emeis, Robertson, Richter, et al., 1996). However, the paleotemperatures calculated for the Balearic Sea are ~5°C cooler than those estimated at times of sapropel deposition in the eastern areas. Part of this difference (≈2°C) appears to be real inasmuch as the extraction and analysis procedures used during Leg 161 were intercalibrated with those of Leg 160 (see "Explanatory Notes" chapter, this volume).

Headspace Gases

Concentrations of headspace methane were low throughout Site 975. The strongly reducing conditions needed for methanogenesis evidently have never been achieved in the sediments at Site 975, and sulfate concentrations remain high throughout the recovered Site 975 sediments (see "Inorganic Geochemistry" section, this chapter). As noted by Claypool and Kvenvolden (1983), the presence of interstitial sulfate inhibits methanogenesis in marine sediments.

INORGANIC GEOCHEMISTRY

Interstitial water samples were obtained at Site 975 from 1.45 mbsf to 306.85 mbsf. Twenty-six samples were collected from Holes

Table 10. Splice table for Site 975.

Hole, core, section, interval (cm)	Depth (mbsf)	Depth (mcd)		Hole, core, section, interval (cm)	Depth (mbsf)	Depth (mcd)
161-975						
D-1H-4, 16	4.66	4.66	tie to	C-2H-1, 124	3.64	4.59
C-2H-6, 7	9.97	10.92	tie to	D-2H-2, 79	9.69	10.92
D-2H-6, 55	15.45	16.68	tie to	B-3H-2, 22	15.32	16.82
B-3H-5, 133	20.93	22.43	tie to	D-3H-3, 73	20.63	22.43
D-3H-6, 34	24.74	26.54	tie to	C-4H-2, 127	24.17	26.53
C-4H-5, 115	28.55	30.91	tie to	D-4H-2, 43	28.33	30.92
D-4H-6, 19	34.09	36.68	tie to	C-5H-2, 109	33.49	36.69
C-5H-4, 43	35.83	39.03	tie to	B-5H-2, 118	35.28	39.03
B-5H-6, 124	41.34	45.09	tie to	C-6H-1, 58	40.98	45.13
C-6H-4, 124	46.14	50.29	tie to	B-6H-3, 28	45.38	50.28
B-6H-6, 142	51.02	55.92	tie to	C-7H-2, 25	51.65	56.02
C-7H-6, 97	58.37	62.74	tie to	D-7H-3, 31	58.21	62.72
D-7H-5, 82	61.72	66.23	tie to	C-8H-2, 46	61.36	66.23
C-8H-4, 58	64.48	69.35	tie to	B-8H-2, 37	62.97	69.37
B-8H-6, 55	69.15	75.55	tie to	C-9H-1, 145	70.35	75.55
C-9H-4, 40	73.80	79.00	tie to	B-9H-2, 58	72.68	78.99
B-9H-6, 70	78.80	85.11	tie to	C-10H-1, 94	79.34	85.17
C-10H-4, 70	83.60	89.43	tie to	B-10H-2, 103	82.63	89.43
B-10H-4, 13	84.73	91.53	tie to	D-10H-2, 84	85.74	91.54
D-10H-7, 24	92.64	98.44	tie to	B-11H-2, 28	91.38	97.93
B-11H-4, 145	95.55	102.10	tie to	D-11H-3, 14	96.04	102.01
D-11H-6, 124	101.64	107.61	tie to	B-12H-2, 16	100.76	107.63
B-12H-3, 103	103.13	110.00	tie to	D-12H-1, 104	103.44	110.02
D-12H-6, 144	111.34	117.92	tie to	B-13H-2, 10	110.20	117.90
B-13H-6, 139	117.49	125.19	tie to	C-14H-2, 97	117.47	125.27
C-14H-7, 13	124.13	131.93	tie to	D-14H-3, 24	124.64	131.90
D-14H-5, 54	127.94	135.20	tie to	C-15H-2, 4	127.44	135.24
Listed below are ties between individual cores. Cores from Holes 975B and 975D have been adjusted to match Hole 975C.						
C-17X-2, 34	146.74	154.54	tie to	D-16X-2, 64	142.54	154.80
B-18X-4, 25	161.05	168.56	tie to	C-18X-5, 34	160.74	168.54
B-24X-4, 43	220.83	228.34	tie to	C-24X-6, 73	220.43	228.23
B-25X-3, 127	228.66	236.98	tie to	C-25X-5, 133	229.03	236.83
B-26X-3, 133	239.21	246.82	tie to	C-26X-6, 19	239.09	246.89
B-27X-4, 103	250.33	258.65	tie to	C-28X-1, 49	251.49	259.29
B-29X-6, 16	271.76	280.08	tie to	C-30X-1, 136	272.26	280.06
B-30X-4, 31	278.41	286.73	tie to	C-30X-6, 22	278.62	286.42
B-31X-3, 130	287.60	297.19	tie to	C-31X-6, 97	289.27	297.07
B-32X-3, 127	297.07	306.66	tie to	C-32X-6, 58	298.88	306.68

Notes: Portions of cores from Holes 975B, 975C, and 975D were used to construct a complete section, avoiding gaps and overlaps through Core 975C-15H. Below this core, correlations were not made due to increased core disturbance and reduced core recovery. Correlative features in individual cores below 135 mbsf are listed in the lower section of the table and identified by double-ended arrows in Figure 42.

975B and 975C. The consistency between the two holes confirms the high precision of the data.

The interstitial water profiles are dominated by two main patterns: (1) constant concentration to about 100 m and then a steady increase or decrease, and (2) a steady increase or decrease with depth from the sediment-water interface (Table 14 and Figs. 51–54).

Evaporite-Related Fluxes

The presence of evaporites, such as halite (NaCl), anhydrite ($CaSO_4$), and especially gypsum ($CaSO_4 \cdot 2H_2O$), at or below the maximum depth penetrated by coring, would provide one source for calcium, salinity, chlorinity, lithium, sulfate, and sodium, which all increase with depth. The relatively shallow chlorinity and sodium gradients indicate a minimal halite presence in the evaporites.

The calcium and sulfate profiles both exhibit a gentle decrease between the sediment-water interface and 46.55 mbsf, and then increase to near linear gradients toward the base of the hole. Both of these profiles indicate a small flux from the water column and a large flux from depth. Dissolution of gypsum in the Messinian evaporites provides the deep source for the calcium and sulfate and explains why sulfate depletion does not occur at this site, even though bacterial sulfate reduction is the main diagenetic process. The shallower sulfate concentration gradient (0.14 mM/m) compared to the calcium and chlorine gradients (0.21 mM/m) may be because of consumption by anaerobic bacteria during organic carbon metabolization, assuming equal diffusive properties of sulfate and calcium. Calcium and particularly strontium may also originate from interactions of the Messinian brines with biogenic carbonates (see "Carbonate Diagenesis section" this chapter). The high lithium concentrations (Fig. 52) suggest the presence of late-stage brines in the evaporites. Diatom dissolution as a source of the lithium is considered highly unlikely at this site, because no evidence of siliceous microfaunas has been observed in the sediments (see "Lithostratigraphy" section, this chapter).

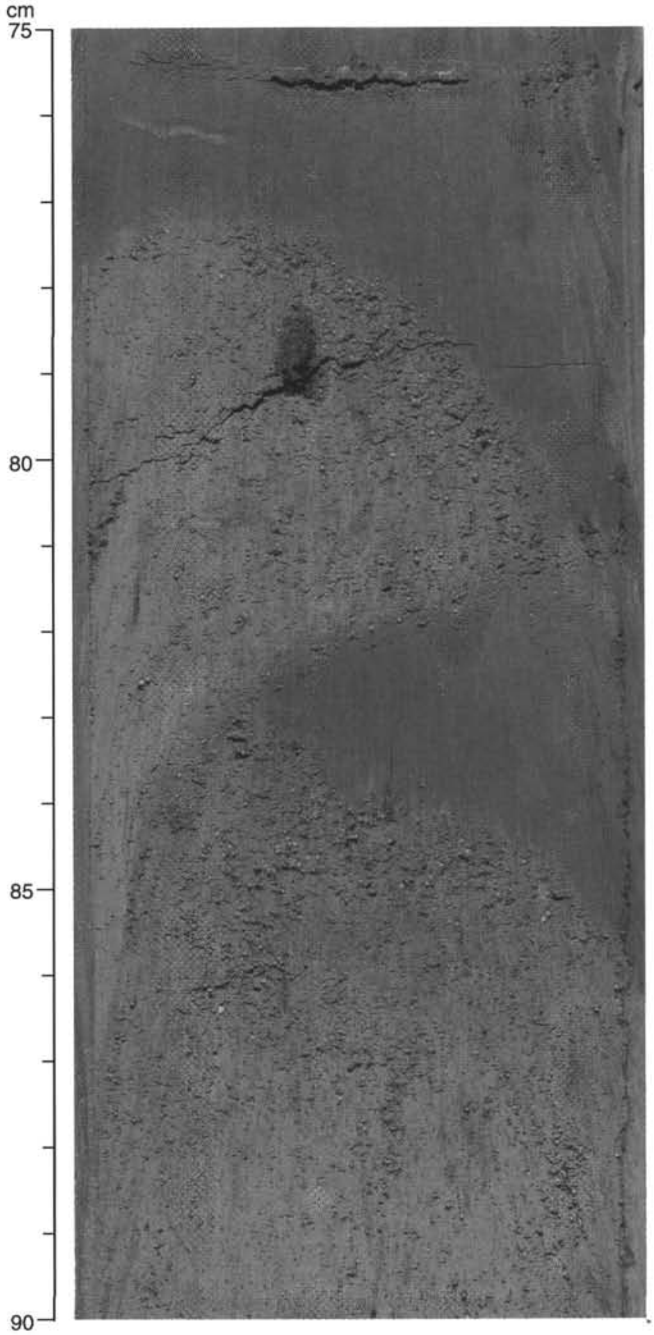

Figure 44. Minor reverse-fault at 85.6 mbsf in Hole 975B. This is probably a result of soft-sediment sliding (close-up photo, 975B-10H-4, 75–90 cm).

Organic Matter Degradation

The ammonium interstitial water profile indicates decomposition of organic matter; the low ammonium concentrations reflect limited

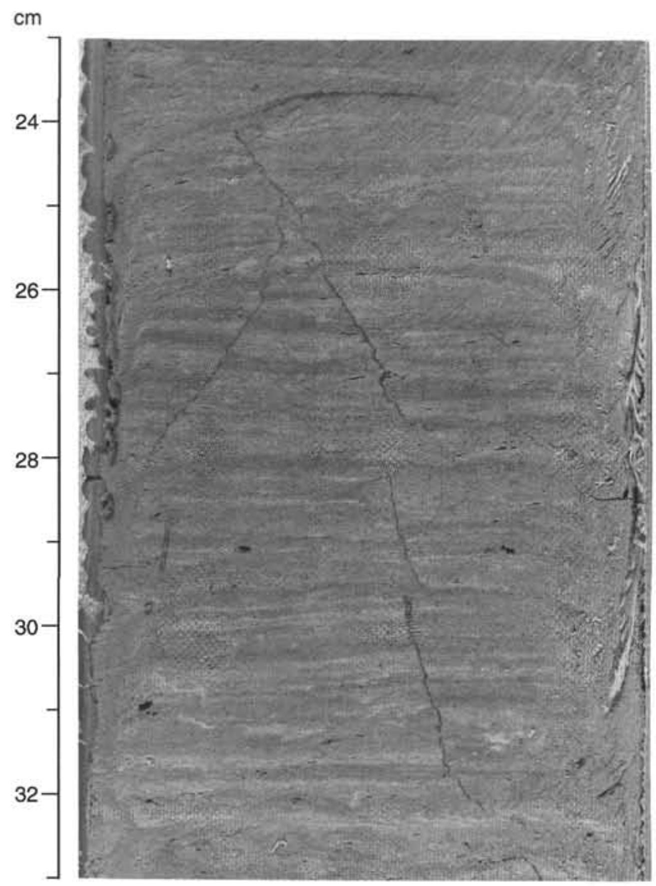

Figure 45. Stylolitic fractures filled by a greenish film in laminated shale and anhydrite at 305.6 mbsf in Hole 975B (close-up photo, 975B-33X-3, 23–33 cm).

availability of organic matter (Fig. 54). The consistent ammonium concentrations below 75.05 mbsf can be ascribed to ion-exchange reactions during organic matter decomposition, which result in ammonium being fixed by clay minerals with a concomitant lithium release. Release of lithium into the interstitial waters, however, would be masked at this site by the high lithium flux from depth. The interstitial water sulfate gradient suggests that organic matter degradation below 5.55 mbsf occurs mainly by sulfate reduction. Between the sediment-water interface and 5.55 mbsf, organic matter degradation is occurring by aerobic degradation and manganese reduction, as evidenced by the manganese mobilization peak at 5.55 mbsf. The resolution of the sampling interval, however, is insufficient to identify the depths of the various reduction zones (manganese, iron, and sulfate). The sulfate flux from the evaporites masks the profile that would be expected in an area of sulfate reduction; such a flux would effectively inhibit the development of methanogenesis (Claypool and Kvenvolden, 1983). Consequently, methane concentrations at this site were very low (see "Organic Geochemistry" section, this chapter). Phosphate concentrations are below the lower limit of detection, reflecting the overall low organic matter content of the sediments at this site (see "Organic Geochemistry" section, this chapter).

Carbonate Diagenesis

The alkalinity profile from the sediment water interface to 75.05 mbsf exhibits concentrations that are consistent and some 2 mM higher than average seawater. This may indicate either a generally low decomposition rate or low abundance of organic matter. Below 200 mbsf, the alkalinity is lower than seawater values, indicating the

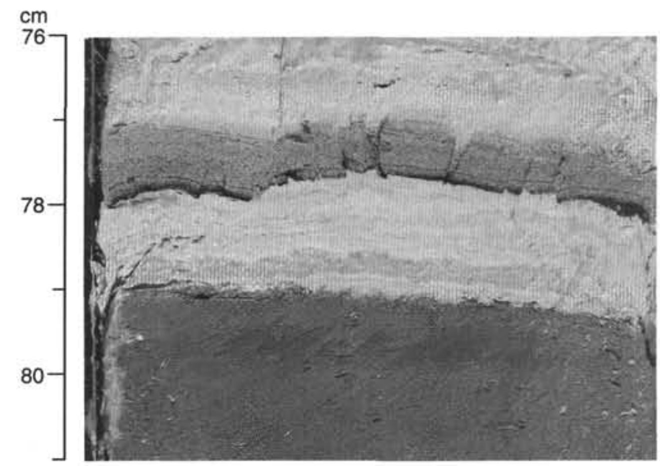

Figure 46. Brittle boudinage in a sand layer within anhydrite at 306.4 mbsf in Hole 975B (close-up photo, 975B-33X-3, 76–81 cm).

precipitation of a carbonate phase or formation of zeolite and clay. The decrease in alkalinity at 75 mbsf, and toward the base of the cored interval, suggests HCO_3^- consumption. The magnesium concentration decreases from 56 mM at the sediment water interface to <55 mM between 27.55 and 75.05 mbsf, before increasing to a peak of 57 mM at 191 mbsf and then decreasing to the base of the cored section. The decrease in both magnesium and alkalinity suggests limited dolomitization could be occurring, from solution, in the upper 70 m of the cored interval, as evidenced by the perceptible decrease in calcium at the top of the cored interval. However, no evidence of dolomitization was visible in this interval. In the lower section of the cored interval dolomitization could be occurring from biogenic calcite dissolution. Dolomite is reported at 306 mbsf (see "Lithostratigraphy" section, this chapter), just above the deepest interstitial water sample. In this case, the interstitial water data are recording this dolomitization process as it occurs.

Remineralization of biogenic carbonate in this manner would liberate strontium. Strontium replaces calcium in $CaCO_3$, anhydrite, and gypsum (Deer et al., 1966; Dean, 1982). However, the occurrence of the strontium peak at 190.85 to 249.25 mbsf suggests that the evaporites are not the source of the strontium flux. Although strontium freely replaces calcium in biogenic $CaCO_3$, upon recrystallization strontium is forced from the $CaCO_3$ lattice (Deer et al., 1966), and thus released to the interstitial phase. Since volcanic ashes are rare at Site 975, the most likely source of the strontium flux is recrystallization of biogenic $CaCO_3$, primarily between 190.85 and 249.25 mbsf. Above and below these depths the near-linear gradients indicate strontium is diffusing away from the inferred zone of recrystallization. The decrease in strontium below 249.25 mbsf indicates strontium consumption; precipitation of celestite, reported at 303 mbsf (see "Lithostratigraphy" section, this chapter), would provide such a sink. Micritization of biogenic carbonates, possibly caused by the evaporitic brines originating from dissolution of the Messinian evaporites, would provide a source for the strontium flux. It is therefore likely that the observed calcium gradient (Fig. 51) reflects both the dissolution of the more soluble gypsum in the evaporites and subsequent interactions of the evaporitic brines with carbonates.

Potassium and Silica

The potassium interstitial profile exhibits a downcore decrease (Fig. 53), which is typical for marine sediments and indicates potassium uptake in clays. This profile is perhaps unexpected, because of the presence of evaporites toward the base of the hole, and may indicate an absence of potassium salts at this locality or limited upward diffusion of certain brine components.

Table 11. Results of inorganic and total carbon (TC) analyses of sediment samples from lithostratigraphic Units I–III at Site 975.

Core, section, interval (cm)	Depth (mbsf)	Inorg. C (wt%)	$CaCO_3$ (wt%)	TC (wt%)	TOC (wt%)	TN (wt%)	TS (wt%)	C/N
Unit I: Pliocene–Pleistocene nannofossil clays and silty clays with organic-rich layers								
161-975B-								
1H-1, 50–51	0.50	5.54	46.1	5.87	0.33	0.05	0.00	7.70
1H-2, 90–92	2.40	4.03	33.6	4.24	0.21	0.03	0.00	8.17
2H-1, 76–77	4.86	4.24	35.3	4.48	0.24	0.04	0.00	7.00
2H-2, 15–16	5.75	3.55	29.6	3.85	0.30	0.05	0.00	7.00
2H-2, 77–78	6.37	6.20	51.6	6.40	0.20	0.04	0.00	5.83
2H-3, 46–47	7.56	5.82	48.5	6.07	0.25	0.10	0.00	2.92
2H-3, 65–66	7.75	4.19	34.9	4.46	0.27	0.05	0.00	6.30
2H-3, 84–85	7.94	5.24	43.6	6.78	1.54	0.14	0.00	12.83
2H-4, 55–56	9.15	4.29	35.7	4.63	0.34	0.04	0.00	9.92
2H-4, 81–82	9.41	4.13	34.4	4.52	0.39	0.06	0.00	7.58
2H-5, 70–71	10.80	4.35	36.2	4.76	0.41	0.05	0.00	9.57
2H-6, 80–81	12.40	3.66	30.5	4.02	0.36	0.05	0.00	8.40
2H-7, 15–16	13.25	4.85	40.4	5.25	0.40	0.06	0.00	7.78
3H-1, 131–132	14.91	4.51	37.6	6.03	1.52	0.14		12.67
3H-2, 100–101	16.10	6.34	52.8	6.57	0.23	0.04	0.00	6.71
3H-2, 113–114	16.23	5.56	46.3	7.27	1.71	0.15	0.00	13.30
3H-3, 100–101	17.60	3.99	33.2	4.48	0.49	0.07	0.00	8.17
3H-4, 61–62	18.71	5.17	43.1	6.09	0.92	0.09	0.00	11.93
3H-7, 24–25	22.84	8.04	67.0	8.35	0.31	0.03	0.00	12.06
3H-7, 42–43	23.02	4.16	34.7	4.54	0.38	0.06	0.00	7.39
4H-1, 132–133	24.42	6.86	57.1	7.11	0.25	0.03	0.00	9.72
4H-2, 51–52	25.11	6.68	55.6	7.65	0.97	0.10	0.00	11.32
4H-4, 69–70	28.29	4.29	35.7	4.65	0.36	0.05	0.00	8.40
4H-5, 83–84	29.93	4.90	40.8	5.18	0.28	0.05	0.00	6.53
4H-5, 97–98	30.07	8.38	69.8	8.61	0.23	0.02	0.00	13.42
4H-CC, 9–10	32.62	5.74	47.8	6.86	1.12	0.11	0.00	11.88
5H-1, 61–62	33.21	5.74	47.8	6.42	0.68	0.06	0.00	13.22
5H-2, 113–114	35.23	4.72	39.3	5.09	0.37	0.06	0.00	7.19
5H-3, 118–119	36.78	5.68	47.3	6.57	0.89	0.09	0.00	11.54
5H-4, 64–65	37.74	7.13	59.4	7.48	0.35	0.02	0.00	20.42
5H-5, 40–41	39.00	5.51	45.9	5.79	0.28	0.05	0.00	6.53
5H-5, 119–120	39.79	5.78	48.1	7.61	1.83	0.16	0.00	13.34
5H-5, 135–136	39.95	5.14	42.8	5.67	0.53	0.08	0.00	7.73
5H-6, 93–94	41.03	6.82	56.8	7.07	0.25	0.03	0.00	9.72
6H-2, 53–54	44.13	5.42	45.1	5.62	0.20	0.05	0.00	4.67
6H-2, 100–101	44.60	5.17	43.1	6.21	1.04	0.11	0.00	11.03
6H-3, 81–82	45.91	4.08	34.0	6.88	2.80	0.18	2.12	18.15
6H-4, 30–31	46.90	4.52	37.7	5.88	1.36	0.13	0.70	12.21
6H-4, 49–50	47.09	2.75	22.9	4.01	1.26	0.17	5.04	8.65
6H-4, 91–92	47.51	4.22	35.2	4.60	0.38	0.07	0.20	6.33
6H-6, 22–23	49.82	4.23	35.2	5.05	0.82	0.09	0.39	10.63
7H-2, 92–93	54.02	6.25	52.1	6.36	0.11	0.03	0.00	4.28
7H-3, 49–50	55.09	4.44	37.0	4.57	0.13	0.05	0.00	3.03
7H-4, 67–68	56.77	4.57	38.1	5.52	0.95	0.11	0.03	10.08
8H-3, 30–31	64.40	4.33	36.1	4.58	0.25	0.05	0.01	5.83
8H-6, 139–140	69.99	7.00	58.3	7.19	0.19	0.05	0.10	4.43
8H-7, 28–29	70.38	5.54	46.1	7.01	1.47	0.13	1.08	13.19
9H-1, 22–23	70.82	3.38	28.2	4.33	0.95	0.12	1.09	9.24
9H-1, 142–143	72.02	4.87	40.6	5.87	1.00	0.11	1.11	10.61
9H-2, 50–51	72.60	5.16	43.0	5.29	0.13	0.05	0.03	3.03
9H-2, 60–61	72.70	4.84	40.3	4.99	0.15	0.06	0.00	2.92
9H-2, 122–123	73.32	5.35	44.6	7.94	2.59	0.18	3.21	16.79
9H-4, 59–60	75.69	3.50	29.2	3.69	0.19	0.06	0.03	3.69
9H-4, 63–64	75.73	4.09	34.1	4.33	0.24	0.05	0.00	5.60
9H-5, 89–90	77.49	4.77	39.7	7.46	2.69	0.20	2.43	15.69
9H-5, 110–111	77.70	6.59	54.9	6.82	0.23	0.05	0.07	5.37
9H-6, 32–33	78.42	5.16	43.0	5.99	0.83	0.10	0.04	9.68
9H-6, 33–34	78.43	5.30	44.1	5.91	0.61	0.09	0.03	7.91
9H-7, 48–49	80.08	4.36	36.3	4.68	0.32	0.06	0.05	6.22
10H-3, 76–77	83.86	5.32	44.3	7.34	2.02	0.16	1.22	14.73
10H-4, 85–86	85.45	6.73	56.1	7.17	0.44	0.05	0.00	10.27
10H-4, 138–139	85.98	5.85	48.7	6.41	0.56	0.08	0.00	8.17
10H-6, 140–141	89.00	4.43	36.9	4.57	0.14	0.05	0.17	3.27
11H-2, 89–90	91.99	3.93	32.7	4.09	0.16	0.05	0.00	3.73
11H-4, 23–24	94.33	5.65	47.1	5.80	0.15	0.05	0.00	3.50
11H-4, 88–89	94.98	5.49	45.7	6.57	1.08	0.11	0.05	11.45
11H-6, 38–39	97.48	6.09	50.7	6.14	0.05	0.04	0.00	1.46
11H-6, 89–90	97.99	3.60	30.0	4.02	0.42	0.07	0.00	7.00
12H-1, 67–68	99.77	5.40	45.0	6.24	0.84	0.10	0.00	9.80
12H-3, 23–24	102.33	5.32	44.3	5.45	0.13	0.05	0.07	3.03
12H-3, 78–79	102.88	5.10	42.5	5.36	0.26	0.06	0.02	5.06
12H-3, 101–102	103.11	5.78	48.1	6.69	0.91	0.04	0.00	26.54
12H-4, 61–62	104.21	4.15	34.6	4.50	0.35	0.05	0.06	8.17
12H-5, 113–114	106.23	8.11	67.6	9.10	0.99	0.09	1.06	12.83
12H-6, 44–45	107.04	6.81	56.7	7.01	0.20	0.05	0.08	4.67
13H-1, 101–102	109.61	7.45	62.1	7.83	0.38	0.07	0.00	6.33
13H-2, 106–107	111.16	6.56	54.6	6.66	0.10	0.03	0.00	3.89
13H-3, 75–76	112.35	6.05	50.4	6.06	0.01	0.09	0.00	0.13
13H-4, 4–5	113.14	8.61	71.7	8.55	0.00	0.06	0.40	0.00
13H-4, 108–109	114.18	6.71	55.9	6.76	0.05	0.06	0.00	0.97
13H-6, 124–125	117.34	3.86	32.2	3.89	0.03	0.07	0.00	0.50
14H-1, 43–44	118.53	4.02	33.5	4.16	0.14	0.09	0.00	1.81
14H-1, 49–50	118.59	4.56	38.0	4.87	0.31	0.10	0.00	3.62
14H-1, 76–77	118.86	5.01	41.7	5.83	0.82	0.11	2.11	8.70
14H-2, 28–29	119.88	4.66	38.8	5.01	0.35	0.11	0.01	3.71
14H-2, 85–86	120.45	6.18	51.5	6.17	0.00	0.08	0.00	0.00

Table 11 (continued).

Core, section, interval (cm)	Depth (mbsf)	Inorg. C (wt%)	$CaCO_3$ (wt%)	TC (wt%)	TOC (wt%)	TN (wt%)	TS (wt%)	C/N
14H-3, 105–106	122.15	5.40	45.0	5.96	0.56	0.09	0.00	7.26
14H-4, 17–18	122.77	5.49	45.7	5.72	0.23	0.08	0.00	3.35
14H-5, 2–3	124.12	4.00	33.3	4.35	0.35	0.07	0.00	5.83
15H-1, 56–57	128.16	4.90	40.8	5.24	0.34	0.08	0.00	4.96
15H-2, 32–33	129.42	4.23	35.2	4.29	0.06	0.07	0.00	1.00
15H-2, 65–66	129.75	5.45	45.4	5.35	0.00	0.07	0.02	0.00
15H-5, 13–14	133.73	4.67	38.9	4.74	0.07	0.06	0.00	1.36
15H-5, 98–99	134.58	6.85	57.1	6.87	0.02	0.07	0.00	0.33
16H-2, 57–58	139.17	7.22	60.1	7.10	0.00	0.06	0.00	0.00
16H-4, 91–92	142.51	4.56	38.0	4.68	0.12	0.95	0.00	0.15
16H-5, 9–10	143.19	4.54	37.8	4.68	0.14	0.78	0.00	0.21
16H-6, 60–61	145.20	4.13	34.4	5.11	0.98	0.07	0.00	16.33
17X-1, 20–21	146.80	7.02	58.5	7.03	0.01	0.08	0.00	0.15
17X-2, 111–112	149.21	7.83	65.2	7.95	0.12	0.06	0.30	2.33
17X-3, 136–137	150.96	6.22	51.8	6.79	0.57	0.08	0.00	8.31
17X-4, 70–71	151.80	5.50	45.8	5.53	0.03	0.72	0.00	0.05
18X-2, 102–103	158.82	6.52	54.3	6.58	0.06	0.08	0.00	0.88
18X-5, 69–70	162.99	5.65	47.1	5.82	0.17	0.06	0.00	3.31
19X-3, 74–75	170.04	5.47	45.6	5.63	0.16	0.05	0.00	3.73
19X-CC, 8–9	170.99	3.22	26.8	3.47	0.25	0.05	0.00	5.83
22X-2, 79–80	198.49	6.33	52.7	6.47	0.14	0.05	0.00	3.27
23X-5, 71–72	212.91	7.52	62.6	7.66	0.14	0.06	0.00	2.72
24X-1, 74–75	216.64	6.65	55.4	6.73	0.08	0.07	0.00	1.33
24X-5, 45–46	222.35	6.98	58.1	7.18	0.20	0.07	0.00	3.33
25X-5, 30–31	230.69	4.78	39.8	5.12	0.34	0.07	0.00	5.67
25X-5, 86–87	231.25	6.51	54.2	6.68	0.17	0.06	0.00	3.31
26X-4, 65–66	240.03	6.58	54.8	6.30	0.00	0.02	0.00	0.00
26X-5, 37–38	241.25	6.24	52.0	6.40	0.16	0.07	0.00	2.67
27X-2, 76–77	247.06	6.29	52.4	6.57	0.28	0.06	0.00	5.44
27X-2, 123–124	247.53	4.53	37.7	4.73	0.20	0.06	0.00	3.89
27X-6, 76–77	253.06	7.61	63.4	7.71	0.10	0.05	0.00	2.33
28X-2, 107–108	257.07	7.17	59.7	6.78	0.00	0.03	0.00	0.00
28X-4, 35–37	259.35	6.89	57.4	7.22	0.33	0.06	0.00	6.42
28X-5, 117–118	261.67	7.51	62.6	7.70	0.19	0.05	0.00	4.43
29X-2, 107–108	266.67	7.72	64.3	8.02	0.30	0.06	0.00	5.83
29X-5, 3–4	270.13	4.67	38.9	5.15	0.48	0.06	0.03	9.33
29X-6, 127–128	272.87	6.66	55.5	6.83	0.17	0.06	0.00	3.31
29X-CC, 29–30	273.92	7.81	65.1	7.88	0.07	0.05	0.00	1.63
30X-1, 64–65	274.24	6.77	56.4	6.42	0.00	0.05	0.00	0.00
30X-4, 37–38	278.47	7.90	65.8	7.95	0.05	0.05	0.00	1.17
30X-4, 138–139	279.48	8.25	68.7	8.34	0.09	0.05	0.00	2.10
30X-6, 41–42	281.51	7.04	58.6	7.31	0.27	0.06	0.00	5.25
31X-1, 66–67	283.96	8.43	70.2	8.58	0.15	0.06	0.00	2.92
31X-5, 72–73	290.02	7.75	64.6	7.90	0.15	0.05	0.00	3.50
31X-7, 23–24	292.53	7.93	66.1	7.91	0.00	0.06	0.00	0.00
32X-1, 96–97	293.76	7.39	61.6	7.53	0.14	0.05	0.00	3.27
33X-1, 10–11	302.50	7.67	63.9	7.75	0.08	0.04	0.00	2.33
33X-1, 146–147	303.86	7.89	65.7	8.00	0.11	0.05	0.00	2.57
33X-2, 68–69	304.58	7.68	64.0	7.78	0.10	0.05	0.00	2.33
33X-2, 102–103	304.92	4.43	36.9	4.52	0.09	0.04	0.00	2.63
33X-2, 130–131	305.20	3.75	31.2	4.13	0.38	0.09	0.00	4.93
161-975C-								
1H-2, 26–27	1.76	4.68	39.0	4.76	0.08	0.06	0.00	1.56
2H-4, 128–129	8.18	9.51	79.2	5.85	0.00	0.08	0.00	0.00
2H-6, 69–70	10.59	4.24	35.3	4.50	0.26	0.06	0.00	5.06
3H-2, 40–41	13.80	4.38	36.5	5.47	1.09	0.12	0.66	10.60
3H-2, 76–77	14.16	5.13	42.7	6.79	1.66	0.14	1.49	13.83
3H-2, 103–104	14.43	4.69	39.1	5.81	1.12	0.14	1.29	9.33
3H-3, 17–18	15.07	4.30	35.8	4.39	0.09	0.71	0.00	0.15
3H-3, 94–95	15.84	5.48	45.6	6.96	1.48	0.15	0.00	11.51
3H-5, 46–47	18.36	6.08	50.6	6.14	0.06	0.07	0.00	1.00
3H-5, 55–56	18.45	5.66	47.1	6.50	0.84	0.84	0.00	1.17
3H-6, 42–43	19.82	4.02	33.5	4.11	0.09	0.62	0.00	0.17
4H-1, 55–56	21.95	3.76	31.3	3.80	0.04	0.72	0.00	0.06
4H-1, 105–106	22.45	8.67	72.2	8.52	0.00	0.07	0.00	0.00
4H-1, 122–123	22.62	4.13	34.4	4.12	0.00	0.56	0.04	0.00
4H-3, 122–123	25.62	6.82	56.8	7.60	0.78	0.10	0.14	9.10
5H-1, 17–18	31.07	7.99	66.6	7.92	0.00	1.10	0.00	0.00
5H-1, 149–150	32.39	6.86	57.1	8.28	1.42	0.15	3.53	11.04
5H-2, 1–2	32.41	6.25	52.1	7.38	1.13	0.13	3.79	10.14
5H-3, 24–25	34.14	3.87	32.2	4.13	0.26	0.07	0.00	4.33
5H-5, 39–40	37.29	5.61	46.7	6.46	0.85	0.10	0.95	9.92
5H-7, 60–61	40.50	5.93	49.4	7.83	1.90	0.16	3.81	13.85
6H-1, 73–74	41.13	7.31	60.9	7.52	0.21	0.05	0.48	4.90
6H-2, 128–129	43.18	4.73	39.4	6.09	1.36	0.21	3.41	7.56
6H-3, 67–68	44.07	4.53	37.7	4.70	0.17	0.06	0.00	3.31
6H-4, 30–31	45.20	5.27	43.9	6.36	1.09	0.13	1.18	9.78
6H-5, 29–30	46.69	4.47	37.2	7.37	2.90	0.21	2.48	16.11
6H-5, 129–130	47.69	4.53	37.7	6.07	1.54	0.15	2.40	11.98
6H-5, 148–149	47.88	3.05	25.4	4.66	1.61	0.14		13.42
6H-6, 84–85	48.74	4.44	37.0	4.80	0.36	0.09	0.00	4.67
7H-1, 71–72	50.61	4.42	36.8	5.52	1.10	0.11	2.58	11.67
7H-1, 76–77	50.66	4.56	38.0	4.88	0.32	0.08	0.00	4.67
7H-3, 85–86	53.75	6.17	51.4	6.34	0.17	0.07	0.00	2.83
7H-5, 107–108	56.97	5.01	41.7	5.77	0.76	0.10	1.00	8.87
7H-6, 77–78	58.17	4.50	37.5	4.64	0.14	0.08	0.00	2.04
8H-5, 65–66	66.05	4.47	37.2	4.60	0.13	0.07	1.08	2.17
8H-5, 142–143	66.82	3.87	32.2	4.12	0.25	0.07	2.42	4.17

Table 11 (continued).

Core, section, interval (cm)	Depth (mbsf)	Inorg. C (wt%)	$CaCO_3$ (wt%)	TC (wt%)	TOC (wt%)	TN (wt%)	TS (wt%)	C/N
8H-6, 92–93	67.82	5.89	49.1	6.02	0.13	0.08	0.47	1.90
9H-3, 10–12	72.00	3.38	28.2	4.38	1.00	0.12	2.48	9.72
9H-6, 70–71	77.10	4.83	40.2	5.51	0.68	0.11	1.83	7.21
10H-2, 80–81	80.70	3.80	31.7	3.97	0.17	0.05	0.00	3.97
10H-3, 23–24	81.63	5.25	43.7	5.36	0.11	0.08	0.00	1.60
10H-4, 23–24	83.13	6.82	56.8	7.49	0.67	0.03	4.30	26.06
11H-2, 48–49	89.88	3.72	31.0	3.89	0.17	0.05	0.70	3.97
12H-3, 74–75	101.14	6.32	52.6	6.56	0.24	0.07	1.64	4.00
13H-5, 45–46	113.35	5.63	46.9	5.72	0.09	0.08	0.00	1.31
13H-5, 48–49	113.38	6.96	58.0	7.11	0.15	0.06	0.00	2.92
13H-5, 102–103	113.92	7.48	62.3	7.54	0.06	0.06	0.00	1.17
13H-6, 34–36	114.74	5.04	42.0	5.16	0.12	0.06	0.00	2.33
13H-6, 54–55	114.94	8.98	74.8	9.04	0.06	0.04	1.29	1.75
14H-3, 120–121	119.20	4.66	38.8	4.75	0.09	0.07	3.02	1.50
14H-5, 63–64	121.63	6.67	55.6	6.77	0.10	0.07	0.00	1.67
15H-2, 122–124	128.62	5.07	42.2	5.18	0.11	0.07	0.40	1.83
15H-4, 93–94	131.33	6.60	55.0	6.76	0.16	0.06	0.00	3.11
16H-1, 52–53	135.92	7.67	63.9	7.83	0.16	0.07	0.00	2.67
16H-4, 12–13	140.02	4.33	36.1	4.45	0.12	0.07	2.70	2.00
17X-2, 64–65	147.04	7.14	59.5	7.27	0.13	0.06	0.32	2.53
17X-3, 64–65	148.54	4.52	37.7	4.71	0.19	0.08	0.00	2.77
17X-5, 72–73	151.62	9.42	78.5	8.72	0.00	0.04	0.74	0.00
18X-2, 100–101	156.90	6.46	53.8	6.53	0.07	0.06	0.00	1.36
19X-2, 67–68	166.27	5.98	49.8	6.03	0.05	0.09	0.00	0.65
19X-4, 65–66	169.25	5.73	47.7	5.93	0.20	0.08	0.00	2.92
20X-4, 59–60	178.79	6.82	56.8	6.82	0.00	0.07	0.00	0.00
20X-6, 109–110	182.29	7.49	62.4	7.53	0.04	0.07	0.00	0.67
21X-3, 44–45	186.84	5.82	48.5	5.90	0.08	0.08	0.00	1.17
21X-5, 69–70	190.09	5.43	45.2	5.48	0.05	0.08	0.00	0.73
22X-3, 75–76	196.65	4.81	40.1	5.11	0.30	0.08	1.06	4.38
23X-5, 52–53	209.02	5.82	48.5	5.81	0.00	0.07	0.00	0.00
24X-3, 67–68	215.87	6.35	52.9	6.39	0.04	0.06	0.14	0.78
25X-4, 73–74	226.93	6.68	55.6	6.74	0.06	0.08	0.00	0.88
25X-5, 90–91	228.60	4.13	34.4	4.35	0.22	0.08	1.08	3.21
26X-1, 80–82	232.20	7.36	61.3	7.31	0.00	0.06	0.00	0.00
26X-6, 60–62	239.50	6.47	53.9	6.40	0.00	0.06	0.00	0.00
27X-6, 96–97	249.46	6.38	53.1	6.68	0.30	0.07	0.00	5.00
28X-2, 46–47	252.96	7.02	58.5	7.10	0.08	0.07	0.00	1.33
28X-3, 72–73	254.72	6.81	56.7	6.83	0.02	0.06	0.00	0.39
30X-5, 72–73	277.62	8.00	66.6	7.89	0.00	0.05	0.00	0.00
30X-6, 72–73	279.12	7.30	60.8	7.43	0.13	0.06	0.00	2.53
31X-1, 77–79	281.57	7.67	63.9	7.79	0.12	0.07	0.00	2.00
31X-5, 78–79	287.58	8.78	73.1	8.84	0.06	0.05	0.00	1.40
32X-1, 134–135	292.14	7.24	60.3	7.33	0.09	0.06	0.00	1.75
32X-2, 120–121	293.50	7.23	60.2	7.23	0.00	0.06	0.00	0.00
32X-3, 17–18	293.97	4.64	38.7	4.99	0.35	0.07	1.11	5.83
32X-5, 83–85	297.63	8.76	73.0	8.88	0.12	0.05	0.00	2.80
33X-1, 55–56	301.25	6.07	50.6	6.10	0.03	0.06	0.00	0.58
33X-2, 148–149	303.68	8.11	67.6	8.20	0.09	0.04	0.00	2.63
33X-3, 10–11	303.80	7.65	63.7	7.75	0.10	0.05	0.00	2.33
33X-3, 145–146	305.15	8.49	70.7	8.46	0.00	0.05	0.00	0.00
33X-4, 97–98	306.17	6.97	58.1	6.98	0.01	0.05	1.18	0.23
33X-4, 109–110	306.29	5.94	49.5	6.06	0.12	0.04	0.00	3.50
Unit 2: Miocene–Pliocene calcareous clays and silty clays with dolomite								
161-975B-								
33X-2, 130–131	305.2	3.75	31.2	4.13	0.38	0.09	0.00	4.93
33X-2, 132–133	305.22	6.54	54.5	6.75	0.21	0.06	0.00	4.08
33X-2, 135–136	305.25	4.06	33.8	4.14	0.08	0.06	0.00	1.56
33X-2, 139–140	305.29	6.75	56.2	6.80	0.05	0.06	0.00	0.97
33X-3, 68–69	306.08	10.99	91.5	11.40	0.41	0.03	0.00	15.94
33X-3, 86–87	306.26	3.98	33.2	4.06	0.08	0.05	0.00	1.79
33X-3, 143–144	306.83	5.51	45.9	5.53	0.02	0.03	0.00	0.78
33X-CC, 7–8	306.93	3.07	25.6	3.58	0.51	0.00	0.00	
161-975C-								
33X-CC, 26–26	306.80	9.88	82.3	10.10	0.22	0.03	0.00	8.56
Unit 3: Pliocene gypsum, micritic gypsum								
161-975B-								
33X-CC, 21–22	307.07	0.59	4.9	0.60	0.01	0.05	0.00	0.23
34X-2, 26–27	311.76	0.17	1.4	0.11	0.00	0.00	0.00	
34X-3, 28–29	313.25	2.92	24.3	2.94	0.02	0.03	0.00	0.78
34X-CC, 1–2	313.74	5.18	43.1	5.19	0.01	0.00	0.00	
34X-CC, 4–5	313.77	1.75	14.6	1.78	0.03	0.00	0.00	

Notes: Total organic carbon (TOC) concentrations are calculated from the difference between inorganic carbon and TC concentrations. TS = total sulfur concentrations. C/N ratios are calculated from TOC and total nitrogen (TN) concentrations and are given as atom/atom ratios.

The interstitial silica profile increases rapidly from 62 μM at the sediment-water interface to 213 μM at 37.05 mbsf, and remains at 200 to 300 μM to the base of the cored section. Such low silica concentrations would make the interstitial waters corrosive toward siliceous microfossils, which are indeed very rare at Site 975 (see "Lithostratigraphy" and "Biostratigraphy" sections, this chapter).

In conclusion, the interstitial water profiles at Site 975 are strongly influenced by the presence of the evaporitic sequence at the depth of maximum coring penetration. The interstitial fluxes indicate the evaporites are dominated by gypsum; the relatively low chlorinity and sodium concentrations toward the base of the cored interval suggest only a limited halite presence in the evaporitic sequence. The decrease in potassium with depth indicates an absence of potassium-bearing salts at this location. The presence of anhydrite in the evaporites at this site cannot be ruled out because of the low solubility of anhydrite in water. The interaction of brines, from dissolution of the evaporites, with biogenic carbonate results in extensive carbonate recrystallization, plus a degree of dolomitization in the lower Pliocene

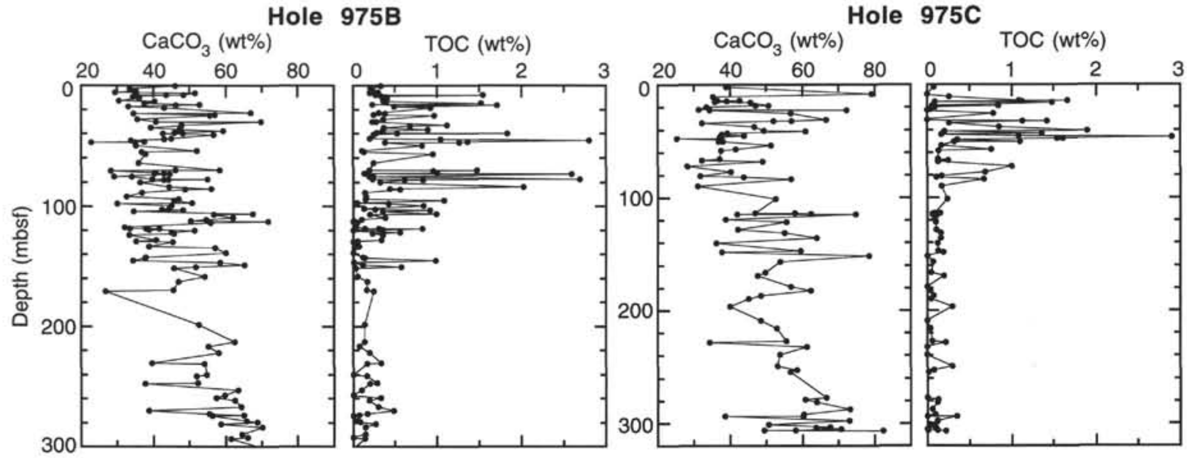

Figure 47. Downcore variations in organic carbon and $CaCO_3$ concentrations in sediment samples from Hole 975B and Hole 975C.

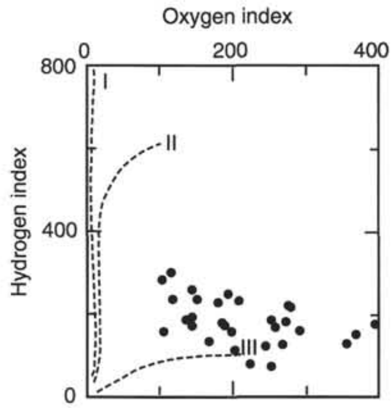

Figure 48. Rock-Eval van Krevelen-type diagram of Pleistocene sapropels from Holes 975B and 975C. Organic matter appears to be originally Type II algal material that has been variably oxidized to Type III continental or detrital organic matter. Hydrogen index = mg hydrocarbons/g organic carbon; oxygen index = mg CO_2/g organic carbon.

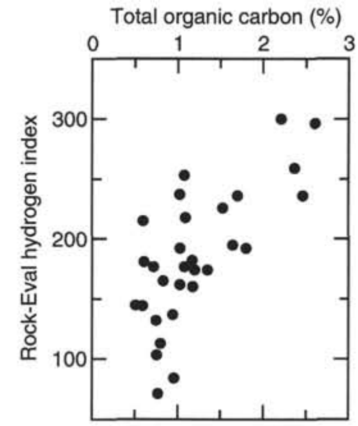

Figure 49. Comparison of Rock-Eval hydrogen index values and total organic carbon concentrations of sapropels from Holes 975B and 975C. The correspondence between increases in both parameters indicates that diminished oxidation of algal organic matter is important to enhancing the organic-carbon richness of sapropels on the Menorca Rise.

sediments. This carbonate recrystallization is evidenced in the strontium profile.

PHYSICAL PROPERTIES

Introduction

Physical property measurements were made on whole-core sections (MST and thermal conductivity), split cores (sonic velocity), and discrete samples (index properties) for all holes at Site 975. Natural gamma ray was measured at 10-cm intervals on all Site 975 cores as part of the MST. Index properties and thermal conductivity were measured once per section on cores from Holes 975A and 975B. Index properties were measured on one or two samples per core for Hole 975C. Thermal conductivities were measured three times per core for Holes 975C and 975D.

Multisensor Track

The multisensor track measurements for Holes 975A, 975B, 975C, and 975D are presented in Figures 55–58. To facilitate comparison, the presentation is done in a format similar to that used for the downhole logging data in this volume.

Thermal Conductivity

Thermal conductivity results for Holes 975A, 975B, 975C, and 975D are shown in Figure 59 and listed in Table 15 (on CD-ROM, back pocket, this volume). There is only a very slight increase in conductivity vs. depth, with mean values of 1.25 W/(m·K) at the surface increasing to 1.5 W/(m·K) at 300 mbsf.

P-wave Velocity

P-wave velocity measurements (Fig. 60; Table 16 on CD-ROM, back pocket, this volume) show an increase downhole. Velocity increases with depth from 1.5 km/s to 1.8 km/s at 300 mbsf. A break in this trend occurs between about 150 to 250 mbsf. This coincides with the switch from APC to XCB coring and is the same depth interval as that of the larger and more irregular hole diameter found by downhole caliper measurements (see "Downhole Logging" section, this chapter). The trend seen above 150 mbsf is resumed in the harder sed-

Table 12. Results of Rock-Eval pyrolysis analyses of sapropels selected from Holes 975B and 975C.

Core, section, interval (cm)	Depth (mbsf)	TOC (%)	T_{max} (°C)	S_1	S_2	S_3	PI	S_2/S_3	PC	HI	OI
161-975B-											
2H-3, 84–85	7.94	1.17	413	0.36	2.14	3.19	0.14	0.67	0.20	182	272
3H-1, 131–132	14.91	0.96	391	0.40	0.81	2.49	0.33	0.32	0.10	84	259
3H-2, 113–114	16.23	1.09	414	0.41	2.38	3.06	0.15	0.77	0.23	218	280
4H-CC, 9–10	32.62	0.83	415	0.22	1.37	2.46	0.14	0.55	0.13	165	296
5H-5, 119–120	39.79	1.53	415	0.43	3.46	2.77	0.11	1.24	0.32	226	181
6H-3, 81–82	45.91	2.37	420	0.54	6.15	3.54	0.08	1.73	0.55	259	149
6H-4, 30–31	46.90	1.03	419	0.25	1.98	2.61	0.11	0.75	0.18	192	253
6H-4, 49–50	47.09	1.35	416	0.28	2.35	2.13	0.11	1.10	0.21	174	149
6H-6, 22–23	49.82	0.77	408	0.08	0.55	1.80	0.13	0.30	0.05	71	233
7H-4, 67–68	56.77	0.61	418	0.15	1.11	2.45	0.12	0.45	0.10	181	401
8H-7, 28–29	70.38	1.08	419	0.26	2.74	2.18	0.09	1.25	0.25	253	201
9H-1, 22–23	70.82	0.80	409	0.14	0.91	1.95	0.13	0.45	0.08	113	247
9H-1, 142–143	72.02	0.75	418	0.15	0.99	2.09	0.13	0.47	0.09	132	278
9H-2, 122–123	73.32	2.21	419	0.63	6.65	2.88	0.09	2.30	0.60	300	130
9H-5, 89–90	77.49	2.47	420	0.51	5.84	3.32	0.08	1.75	0.52	236	134
10H-3, 76–77	83.86	1.70	424	0.39	4.02	2.69	0.09	1.49	0.36	236	158
11H-4, 88–89	94.98	0.72	419	0.14	1.28	1.91	0.10	0.67	0.11	177	265
12H-5, 113–114	106.23	0.60	420	0.51	1.29	1.69	0.28	0.76	0.15	215	281
161-975C-											
3H-2, 76–77	14.16	1.64	408	0.47	3.21	2.51	0.13	1.27	0.30	195	153
3H-2, 103–104	14.43	1.03	405	0.32	1.67	2.12	0.16	0.78	0.16	162	205
5H-1,149–150	32.39	1.20	406	0.30	2.09	2.36	0.13	0.88	0.19	174	196
5H-7, 60–61	40.50	1.80	412	0.48	3.47	2.59	0.12	1.33	0.32	192	143
6H-2, 128–129	43.18	1.08	409	0.30	1.92	2.09	0.14	0.91	0.18	177	193
6H-4, 30–31	45.20	0.59	417	0.15	0.85	2.21	0.15	0.38	0.08	144	374
6H-5, 29–30	46.69	2.61	413	0.77	7.73	2.89	0.09	2.67	0.70	296	110
6H-5, 129–130	47.69	1.03	419	0.29	2.45	2.22	0.11	1.10	0.22	237	215
6H-5, 148–149	47.88	1.18	410	0.36	2.38	1.58	0.13	1.50	0.22	160	106
7H-1, 71–72	50.61	0.94	412	0.19	1.29	1.63	0.13	0.79	0.12	137	173
7H-5, 107–108	56.97	0.51	417	0.15	0.74	1.83	0.17	0.40	0.07	145	358
9H-3, 10–12	72.00	0.76	405	0.13	0.79	1.56	0.14	0.50	0.07	103	205

Notes: Total organic carbon (TOC) concentrations are derived from Rock-Eval parameters and therefore differ somewhat from the TOC values of the same samples in Table 11. Units of the various Rock-Eval parameters are given in the "Explanatory Notes" chapter (this volume).

Table 13. $U^{k'}_{37}$ values and sea-surface paleotemperature estimates obtained from biomarker extracts of sapropels from Hole 975B.

Core, section, interval (cm)	Depth (mbsf)	TOC (wt%)	$U^{k'}_{37}$	SST (°C)
161-975B-				
2H-3, 84–85	7.95	1.54	0.731	23.0
3H-1, 131–132	14.92	1.52	0.474	16.7
3H-2, 113–114	16.24	1.71	0.732	23.0
4H-CC, 9–10	32.63	1.12	0.572	19.1
5H-5, 119–120	39.80	1.83	0.564	18.9
6H-2, 100–101	44.65	1.04	0.501	17.3
6H-3, 81–82	45.92	2.80	0.483	16.9
6H-4, 30–31	46.91	1.36	0.555	18.7
6H-4, 49–50	47.10	1.26	0.685	21.6
8H-7, 28–29	70.39	1.97	0.740	23.2
9H-1, 142–143	72.03	1.00	0.749	23.4
9H-2, 122–123	73.33	2.59	0.691	22.0
9H-5, 89–90	77.50	2.69	0.632	20.5
10H-3, 76–77	83.87	2.02	0.694	22.0
11H-4, 88–89	94.99	1.08	0.599	19.7

Notes: The calibration curve of Ternois et al. (unpubl. data) which is based on Mediterranean populations of *Emiliania huxleyi,* was used. This calibration yields temperatures ~2.9°C cooler than the more commonly used calibration curve of Prahl and Wakeham (1987).

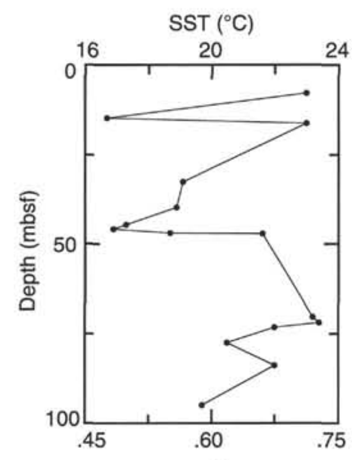

Figure 50. Sea-surface paleotemperatures calculated from $U^{k'}_{37}$ values obtained from biomarker extracts of sapropels from Hole 975B. The calibration curve of Ternois et al. (unpubl. data), which is based on Mediterranean populations of *Emiliania huxleyi,* was used. This calibration yields temperatures ~2.9°C cooler than the more commonly used calibration curve of Prahl and Wakeham (1987).

iments found below 260 mbsf. There is an abrupt increase in velocity to 4.8 km/s at 310 mbsf in the evaporitic sequence (Fig. 60B). A comparison of the MST velocity data with the discrete measurements in the upper 160 m of core (Fig. 60C) shows good agreement down to 60 mbsf. Below 160 mbsf the MST velocities are consistently lower than the discrete measurements.

Index Properties

Grain densities (Fig. 61A; Table 17 on the CD-ROM, back pocket, this volume) show little change with depth in each individual hole or between the different holes. Virtually all values are in the 2.7–2.8 g/cm^3 range.

Bulk density (Fig.61B) increases from 1.7 g/cm^3 at the seafloor to 1.9 g/cm^3 at 150 mbsf. There is then a slight decrease in the values from 150 to 250 mbsf. This occurs in the same interval as the changes in the sonic velocities mentioned above.

Table 14. Interstitial water data from Site 975.

Core, section, interval (cm)	Depth (mbsf)	pH	Alkalinity (mM)	Salinity (‰)	Cl (mM)	Ca (mM)	Mg (mM)	Mn (μM)	Sr (μM)	SO_4 (mM)	NH_4 (μM)	H_4SiO_4 (μM)	Li (μM)	Na (mM)	K (mM)	PO_4 (μM)
161-975B-																
1H-1, 145–150	1.45	7.32	3.331	38.0	609	11.58	57.65	23.5	109	30.7	68	63	n.d.	530	11.43	<2.5
2H-1, 145–150	5.55	7.22	4.160	38.0	608	10.97	56.59	27.0	126	28.6	158	65	n.d.	527	11.46	<2.5
2H-4, 145–150	10.05	7.29	4.320	38.0	604	10.65	56.40	21.5	136	27.9	238	104	17	531	10.97	<2.5
3H-3, 145–150	18.05	7.29	4.363	38.5	606	10.00	55.22	13.0	152	26.3	212	122	17	529	10.69	<2.5
4H-3, 145–150	27.55	7.29	4.315	38.0	609	10.04	54.69	8.0	177	25.1	234	89	18	523	10.26	<2.5
5H-3, 145–150	37.05	7.44	4.464	37.5	604	9.79	54.60	8.5	201	25.4	291	214	20	521	9.38	<2.5
6H-3, 145–150	46.55	7.30	4.291	37.5	603	10.00	54.73	11.0	224	24.6	271	266	20	529	9.22	<2.5
7H-3, 145–150	56.05	7.26	4.312	37.0	603	10.27	54.56	6.5	248	25.7	303	208	21	534	8.76	<2.5
8H-3, 135–140	65.45	7.24	4.707	37.5	605	10.63	54.95	7.5	282	21.9	271	221	24	538	8.15	<2.5
9H-3, 145–150	75.05	7.27	3.874	37.5	615	10.72	54.96	10.0	293	24.6	331	208	25	545	8.17	<2.5
10H-3, 145–150	84.55	7.25	3.807	37.5	614	11.16	55.28	8.0	324	24.5	323	216	26	534	7.92	<2.5
11H-3, 145–150	94.05	7.15	3.668	37.5	623	11.69	55.76	9.5	355	25.7	334	229	27	536	7.43	<2.5
14H-3, 145–150	122.55	7.29	3.569	38.0	619	14.36	56.38	11.0	457	29.8	344	224	32	545	7.08	<2.5
17X-2, 145–150	149.55	7.21	3.167	38.5	614	17.53	56.93	11.0	538	28.6	319	266	37	547	6.82	<2.5
21X-3, 145–150	190.85	7.21	2.560	38.0	640	23.81	57.19	18.0	632	35.1	321	294	41	553	6.06	<2.5
24X-3, 145–151	220.35	7.17	2.248	41.0	636	29.95	55.23	14.5	654	38.7	357	234	42	543	5.87	<2.5
27X-3, 145–151	249.25	7.14	1.955	42.0	648	36.52	54.40	14.5	652	43.2	339	240	42	581	6.07	<2.5
30X-3, 145–151	278.05	7.10	1.467	42.0	642	43.36	53.09	10.0	582	48.9	348	247	41	578	5.85	<2.5
33X-3, 145–151	306.85	7.28	1.357	44.0	654	50.29	52.67	6.5	521	51.3	319	261	40	559	5.51	<2.5
161-975C-																
1H-1, 145–150	1.45	7.26	3.637	38.0	603	11.61	57.14	22.0	106	30.2	79	146	15	536	11.3	<2.5
5H-3, 145–150	35.35	7.26	4.282	37.0	600	9.81	53.93	8.5	197	25.0	270	214	20	550	9.51	<2.5
9H-3, 145–150	73.35	7.35	3.782	37.5	614	10.68	54.67	8.5	303	24.9	308	221	26	525	7.93	<2.5
13H-3, 145–150	111.35	7.29	3.641	38.0	621	13.40	55.88	10.0	413	27.6	146	221	32	545	7.21	<2.5
16H-3, 145–150	139.85	7.31	3.353	38.0	629	16.45	55.81	9.0	503	27.6	328	232	36	535	6.37	<2.5
21X-3, 145–150	187.85	7.15	2.599	40.0	634	23.68	57.72	17.0	650	34.3	339	279	40	534	5.99	<2.5
25X-3, 145–150	226.15	7.09	2.127	41.0	642	30.66	56.19	15.0	334	38.8	345	214	41	552	6.07	<2.5

Note: n.d. = not determined.

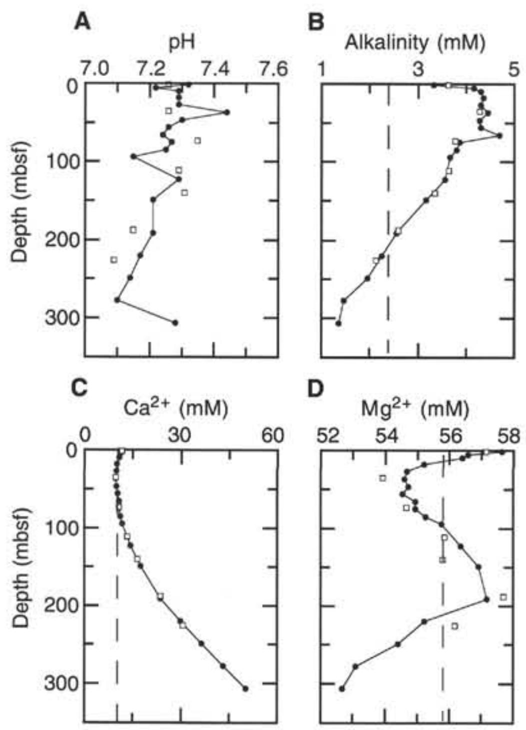

Figure 51. Concentration profiles of (**A**) pH, (**B**) alkalinity, (**C**) calcium, and (**D**) magnesium in Holes 975B and 975C. Solid circles are from Hole 975B, open squares from Hole 975C. The dashed lines indicate standard seawater (International Association for the Physical Sciences of the Ocean [IAPSO]) composition.

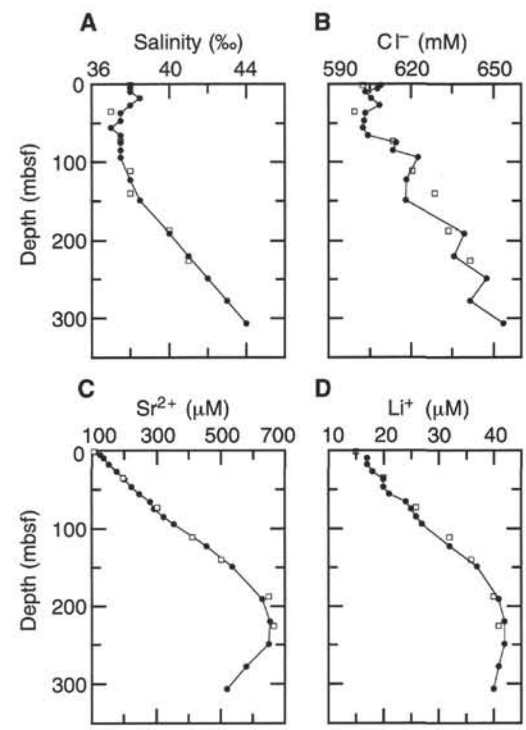

Figure 52. Concentration profiles of (**A**) salinity, (**B**) chloride, (**C**) strontium, and (**D**) lithium in Holes 975B and 975C. Solid circles are from Hole 975B, open squares from Hole 975C.

Porosity (Fig. 61C) decreases with depth from about 65% at the sea floor to 50% at 150 mbsf. At this depth there is a step increase in porosity of about 5%, which is also associated with the change from APC to XCB coring mentioned above. The trend of decreasing porosity with depth continues below this depth. The porosity data do not show the disturbances in the 150 to 250 mbsf interval that were observed in the velocity and bulk density data.

Coring Disturbance Effects on Measurements

The effects of coring disturbances on physical properties measurements is further illustrated in Figures 62A, B, showing data from

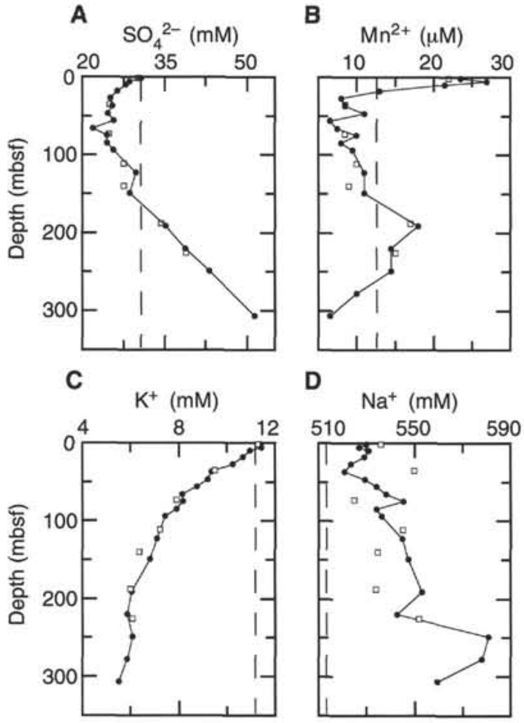

Figure 53. Concentration profiles of (**A**) sulfate, (**B**) manganese, (**C**) potassium, and (**D**) sodium in Holes 975B and 975C. Solid circles are from Hole 975B, open squares from Hole 975C. The dashed lines indicate standard seawater (IAPSO) composition.

Hole 975B. The bulk density measurements (Fig. 62A) in the APC cores show a similar trend in both types of measurements. The offset in values changes dramatically, with the MST values about 0.15 g/cm^3 lower than the index properties values in the APC cores, but 0.25 g/cm^3 lower in the XCB cores. The main cause for this extra offset is the variable air gap between the XCB core and the core liner, which is not readily correctable in the MST measurements.

The velocity measurements (Fig. 62B) in the upper, APC-cored sediments, show good agreement. The MST measurements begin to show lower values than the discrete measurements below 80 mbsf, as the stiffer cores begin to separate from the core liner, introducing air gaps. Air gaps in the XCB cores make MST velocity measurements difficult if not impossible.

DOWNHOLE LOGGING

Quad combination (quad combo), Formation MicroScanner (FMS), and geochemical logging tool (GLT) logging data were acquired in Hole 975C. The drill pipe was positioned at 2468.0 mbrf (41.9 mbsf). The hole was flushed with seawater and then logged between 42.0 and 309.0 mbsf with no significant operational or hole stability problems. A full repeat of the FMS log run and a short repeat section of the quad combo and the GLT logging runs were made. The intervals logged with each tool string are summarized in Table 18.

The log data are generally of good quality (Fig. 63). Variations of the borehole diameter occur mainly in the upper part of the XCB-cored interval. The APC-cored part of the hole and the lower part of the XCB-cored interval showed much less variability in borehole diameter. One of the FMS tool pads shows quite different microresistivity records compared with the three other pads, indicating an imperfect contact with the borehole wall.

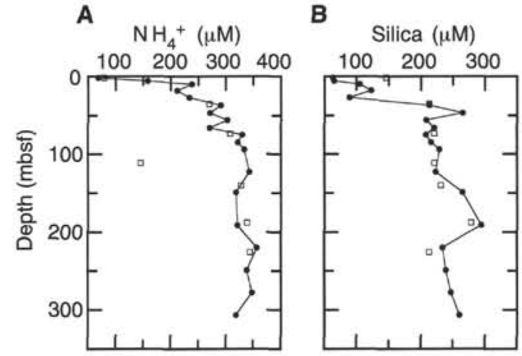

Figure 54. Concentration profiles of (**A**) ammonium and (**B**) silica in Holes 975B and 975C. Solid circles are from Hole 975B, open squares from Hole 975C.

Borehole deviation was near 0° in the upper 150 m, but it changed to 3.5° at the base of the logged interval.

Preliminary analysis of the log data show the following results:

1. The resistivity profile is quite uniform over the entire logged section. Resistivity values increase slightly from 0.7 Ωm at the top of the hole to 1.0 Ωm at the bottom.
2. The caliper data from both the quad combo and the FMS clearly show the change from APC (Cores 975C-1 to 975C-16H) to XCB coring (Cores 975C-17X to 309 mbsf). The XCB coring appears to generate variations in hole diameter, but these variations are reduced when XCB coring in harder sediments at the bottom of the hole.
3. The calipers also detect local increases in the borehole diameter every 9.0 or 9.5 m, throughout the interval from 120.0 to 170.0 mbsf. The depth of these diameter variations corresponds to the pipe break intervals. Figure 64 shows a close-up of this phenomenon. There is a small discrepancy between the FMS and quad combo depth data in this preliminary analysis, but the main application of this may be to provide a precise comparison of cores and logs, which will be aided by the high core recovery in this hole.
4. Figure 65 shows original data concerning interval transit times picked in real-time by the Schlumberger logging unit and reprocessed slowness data. The *P*-wave velocity determined from the reprocessed transit times is also shown. Note the near 9.5-m depth periodicity (length of each core interval) of low transit time values shown in the original data.
5. Preliminary examination of the geochemical logs suggests a change in the rock chemistry at 184.0 mbsf. The aluminum values increase sharply below this depth, as well as Si and gamma-ray values. This probably indicates a higher clay content in this interval, which has not been clearly identified in the cores.

IN SITU TEMPERATURE MEASUREMENTS

Downhole temperature measurements were made with the ADARA temperature tool at five depths in Hole 975C. The instrument worked well on all runs.

The ADARA temperature data were reduced to in situ values (Table 19). The individual temperature measurement runs are shown in Figure 66A–E. Temperature and thermal conductivity measurement data were combined to determine the heat flow (see "Physical Properties" section, this chapter). The thermal conductivity shows a general downhole increase, and the temperature data were plotted vs. the

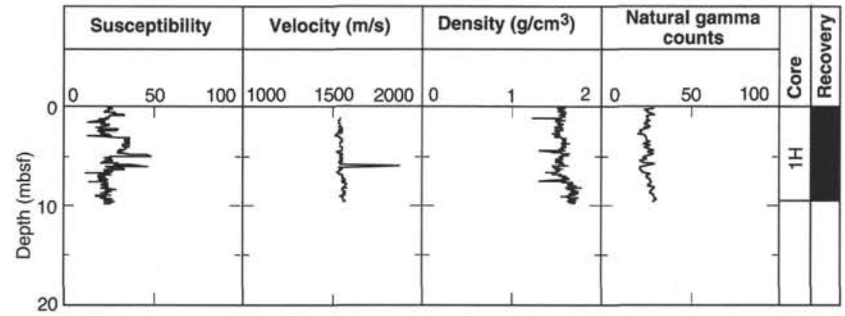

Figure 55. MST data (susceptibility, velocity, density, and natural gamma) for Hole 975A. Cored intervals and recovery are shown on the right.

integrated thermal resistivity (Fig. 67). The best fitting linear regression to the data is shown in Figure 67 and is an excellent fit. The slope of the line is the heat flow, 81 mW/m^2. This value is significantly lower than the values measured to the northeast at DSDP Site 372 on the East Menorca Rise (Erickson and Von Herzen, 1978) and in the adjacent Balearic Basin (Hutchison et al., 1985). It is, however, still a high value and in accord with the generally high heat-flow values in the western Mediterranean basin (Erickson et al., 1977).

SITE GEOPHYSICS

Two intersecting seismic reflection profiles were collected over Site 975 (Figs. 68, 69) with an 80-in^3 water gun. Six main seismic facies (SF) are observed in the seismic lines (Table 20). Holes 975B and 975C penetrated the top three SF, and velocity analyses of the cores from Hole 975B (see "Physical Properties" section, this chapter) allow approximate correlation of the seismic facies to the cored interval (Table 21).

From 3.60 to 3.73 s (two-way traveltime; 0.34 to 0.47 s below seafloor), an extremely high amplitude and continuous series of reflectors is observed. The top of these strong reflections is inferred to originate from the contact of lithostratigraphic Unit II calcareous clays with the Unit III gypsum ("M"-reflector). A large impedance contrast occurs at the contact between the unconsolidated calcareous clays at the base of Unit II (average velocity of 1.70) and the consolidated Unit III gypsum (average velocity of 4.76 km/s). The laboratory velocities predict that this contact should be at 3.63 s two-way traveltime (0.37 s below seafloor), presumably a result of not measuring the core velocities at in situ pressures (higher velocities would result in shorter two-way traveltime).

Below these strong reflectors, sub-parallel, discontinuous, and relatively low-amplitude reflectors extend from 3.73 to 3.90 s (0.47 to ~0.64 s below seafloor) that are similar in character to those from 3.39 to 3.60 s. The layering in these two SF is partially masked by automatic gain control (AGC) caused by the extremely strong reflections above these two SF (3.26 to 3.39 s and 3.60 to 3.73 s).

Discontinuous, sub-parallel to partially chaotic reflections extend from about 3.90 to about 4.18 s. Below this, irregular slightly-hyperbolic, relatively high-amplitude reflections may mark acoustic basement.

REFERENCES

Baker, P.A., and Bloomer, S.H., 1988. The origin of celestite in deep-sea carbonate sediments. *Geochim. Cosmochim. Acta,* 52:335–340.

Baker, P.A., Gieskes, J.M., and Elderfield, H., 1982. Diagenesis of carbonates in deep-sea sediments: evidence from Sr^{2+}/Ca^{2+} ratios and interstitial dissolved Sr^{2+} data. *J. Sediment. Petrol.,* 52:71–82.

Carozzi, A.V., 1993. *Sedimentary Petrography:* Englewood Cliffs, NJ (Prentice Hall).

Cheddadi, R., and Rossignol-Strick, M., 1995. Improved preservation of organic matter and pollen in Eastern Mediterranean sapropels. *Paleoceanography,* 10:301–309.

Cita, M.B., Wright, R.C., Ryan, W.B.F., and Longinelli, A., 1978. Messinian paleoenvironments. *In* Hsü, K.J., Montadert, L., et al., *Init. Repts. DSDP,* 42 (Pt. 1): Washington (U.S. Govt. Printing Office), 1003–1035.

Claypool, G.E., and Kvenvolden, K.A., 1983. Methane and other hydrocarbon gases in marine sediment. *Annu. Rev. Earth Planet. Sci.,* 11:299–327.

Curzi, P.V., Fornos, J., Mauffret, A., Sartori, R., Serra, J., Zitellini, N., Borsetti, A.M., Canals, M., Castellarin, A., Pomar, L., Rossi, P.L., and Sabat, F., 1985. The South-Balearic Margin (Menorca Rise): objectives and preliminary results of the cruise Bal-84. *Rend. Soc. Geol. Ital.,* 8 (Suppl.):91–96.

Dean, W.E., 1982. Trace and minor elements in evaporites. *In* Dean, W.E., and Schreiber, B.C. (Eds.), *Marine Evaporites.* SEPM Short Course, 4:86–104.

Deer, W.A., Howie, R.A., and Zussman, J., 1966. *An Introduction to the Rock-Forming Minerals:* London (Longman Group).

Emeis, K.-C., Robertson, A.H.F., Richter, C., et al., 1996. *Proc. ODP, Init. Repts.,* 160: College Station TX (Ocean Drilling Program).

Emerson, S., and Hedges, J.I., 1988. Processes controlling the organic carbon content of open ocean sediments. *Paleoceanography,* 3:621–634.

Erickson, A.J., Simmons, G., and Ryan, W.B.F., 1977. Review of heat flow data from the Mediterranean and Aegean seas. *In* Biju-Duval, B., and Montadert, L. (Eds.), *International Symposium on the Structural History of the Mediterranean Basins:* Paris (Technip), 263–279.

Erickson, A.J., and Von Herzen, R.P., 1978. Down-hole temperature measurements, Deep Sea Drilling Project, Leg 42A. *In* Hsü, K.J., Montadert, L., et al., *Init. Repts. DSDP,* 42 (Pt. 1): Washington (U.S. Govt. Printing Office), 857–871.

Espitalié, J., Laporte, J.L., Leplat, P., Madec, M., Marquis, F., Paulet, J., and Boutefeu, A., 1977. Méthode rapide de caractérisation des roches mères, de leur potentiel pétrolier et de leur degré d'évolution. *Rev. Inst. Fr. Pet.,* 32:23–42.

Friedman, G.M., 1973. Petrographic data and comments on the depositional environment of the Miocene sulfates and dolomites at Sites 124, 132 and 134, western Mediterranean Sea. *In* Ryan, W.B.F., Hsü, K.J., et al., *Init. Repts. DSDP,* 13 (Pt. 2): Washington (U.S. Govt. Printing Office), 695–708.

Garrison, R.E., Schreiber, B.C., Bernoulli, D., Fabricius, F.H., Kidd, R.B., and Mélières, F., 1978. Sedimentary petrology and structures of Messinian evaporitic sediments in the Mediterranean Sea, Leg 42A, Deep Sea Drilling Project. *In* Hsü, K.J., Montadert, L., et al., *Init. Repts. DSDP,* 42 (Pt. 1): Washington (U.S. Govt. Printing Office), 571–611.

Heider, F.D., Dunlop, D.J., and Soffel, H.C., 1992. Low-temperature and alternating field demagnetization of saturation remanence and thermoremanence in magnetite grains (0.037 mm to 5 mm). *J. Geophys. Res.,* 97:9371–9381.

Hill, P.R., 1984. Facies and sequence analysis of Nova Scotian slope muds: turbidite vs 'hemipelagic' deposition. *In* Stow, D.A.V., and Piper, D.J.W. (Eds.), *Fine-Grained Sediments: Deep-Water Processes and Facies.* Geol. Soc. Spec. Publ. London, 15:311–318.

Hsü, K.J., Montadert, L., et al., 1978. *Init. Repts. DSDP,* 42 (Pt. 1): Washington (U.S. Govt. Printing Office).

Hsü, K.J., Montadert, L., Bernoulli, D., Cita, M.B., Erickson, A., Garrison, R.E., Kidd, R.B., Melières, F., Müller, C., and Wright, R., 1978. History of the Mediterranean salinity crisis. *In* Hsü, K.J., Montadert, L., et al., *Init. Repts. DSDP,* 42 (Pt. 1): Washington (U.S. Govt. Printing Office), 1053–1078.

Hutchison, I., Von Herzen, R.P., Louden, K.E., Sclater, J.G., and Jemsek, J., 1985. Heat flow in the Balearic and Tyrrhenian Basins, Western Mediterranean. *J. Geophys. Res.,* 90:685–701.

Johnson, H.P., Lowrie, W., and Kent, D.V., 1975. Stability of anhysteretic remanent magnetization in fine and coarse magnetite and maghemite particles. *Geophys. J. R. Astron. Soc.,* 41:1–10.

Kastens, K.A., Mascle, J., Auroux, C., et al., 1987. *Proc. ODP, Init. Repts.,* 107: College Station, TX (Ocean Drilling Program).

Mauffret, A., Montadert, L., Lavergne, M., and Willm, C., 1978. Geological and geophysical setting of DSDP Site 372 (Western Mediterranean). *In* Hsü, K.J., Montadert, L., et al., *Init. Repts. DSDP,* 42 (Pt. 1): Washington (U.S. Govt. Printing Office), 889–897.

Meyers, P.A., 1994. Preservation of elemental and isotopic source identification of sedimentary organic matter. *Chem. Geol.,* 144:289–302.

Morse, J.W., and Mackenzie, F.T., 1990. *Geochemistry of Sedimentary Carbonates.* Dev. in Sedimentology, 48: Amsterdam (Elsevier).

Müller, C., 1978. Neogene calcareous nannofossils from the Mediterranean—Leg 42A of the Deep Sea Drilling Project. *In* Hsü, K.J., Montadert, L., et al., *Init. Repts DSDP,* 42 (Pt. 1): Washington (U.S. Govt. Printing Office), 727–751.

————, 1990. Nannoplankton biostratigraphy and paleoenvironmental interpretations from the Tyrrhenian Sea, ODP Leg 107 (Western Mediterranean.) *In* Kastens, K.A., Mascle, J., et al., *Proc. ODP, Sci. Results,* 107: College Station, TX (Ocean Drilling Program), 495–511.

Müller, P.J., 1977. C/N ratios in Pacific deep sea sediments: effect of inorganic ammonium and organic nitrogen compounds sorbed by clays. *Geochim. Cosmochim. Acta,* 41:765–776.

Murat, A., 1991. Enrégistrement sédimentaire des paléoenvironnements Quaternaires en Mediterranée Orientale [Ph.D. dissert.]. University of Perpignan, France.

Pickering, K.T., Hiscott, R.N., and Hein, F.J., 1989. *Deep Marine Environments: Clastic Sedimentation and Tectonics:* London (Unwin Hyman).

Prahl, F.G., and Wakeham, S.G., 1987. Calibration of unsaturation patterns in long-chain ketone compositions for paleotemperature assessment. *Nature,* 330:367–369.

Ryan, W.B.F., Hsü, K.J., et al., 1973. *Init. Repts. DSDP,* 13 (Pts. 1 and 2): Washington (U.S. Govt. Printing Office).

Schreiber, B.C., Friedman, G.M., Decima, A., and Schreiber, E., 1976. Depositional environments of Upper Miocene (Messinian) evaporite deposits of the Sicilian basin. *Sedimentology,* 23:729–760.

Shipboard Scientific Party, 1973. Balearic Rise—Site 124. *In* Ryan, W.B.F., Hsü, K.J., et al., *Init. Repts. DSDP,* 13 (Pt. 1): Washington (U.S. Govt. Printing Office), 133–174.

————, 1995. Site 926. *In* Curry, W.B., Shackleton, N.J., Richter, C., et al., *Proc. ODP, Init. Repts.,* 154: College Station, TX (Ocean Drilling Program), 153–232.

Siesser, W.G., Bralower, T.J., and De Carlo, E.H., 1992. Mid-Tertiary *Braarudosphaera*-rich sediments on the Exmouth Plateau. *In* von Rad, U., Haq, B.U., et al., *Proc. ODP, Sci. Results,* 122: College Station, TX (Ocean Drilling Program), 653–663.

Ms 161IR-105

NOTE: For all sites drilled, core-description forms ("barrel sheets") and core photographs can be found in Section 3, beginning on page 429. Smear-slide data can be found in Section 4, beginning on page 949 . See Table of Contents for material contained on CD-ROM.

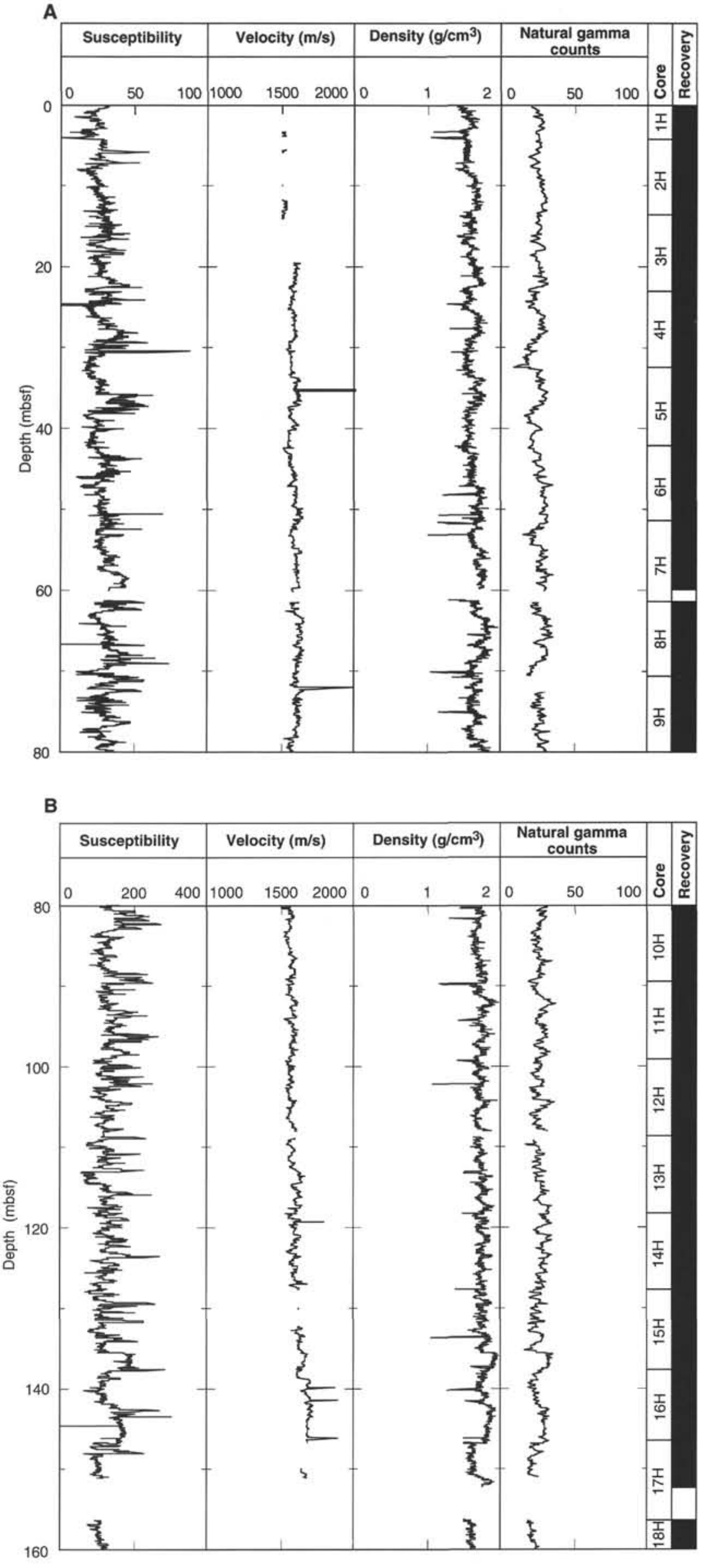

Figure 56. MST data (susceptibility, velocity, density, and natural gamma) for Hole 975B: (**A**) 0–80 mbsf, (**B**) 80–160 mbsf, (**C**) 160–240 mbsf, (**D**) 240–320 mbsf. Cored intervals and recovery are shown on the right.

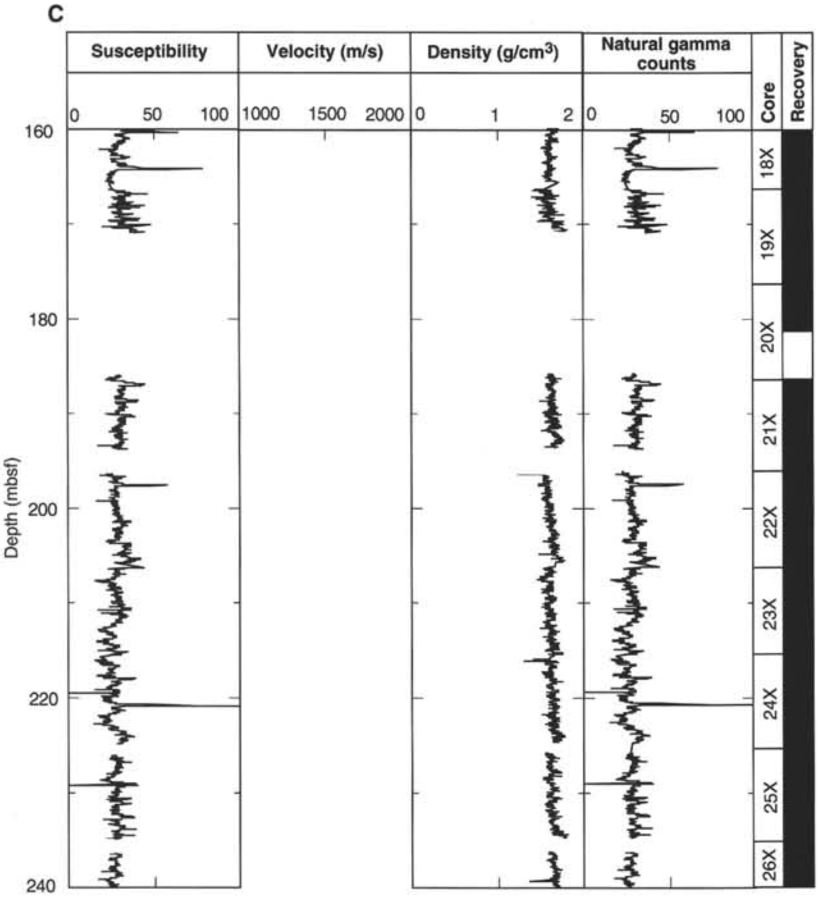

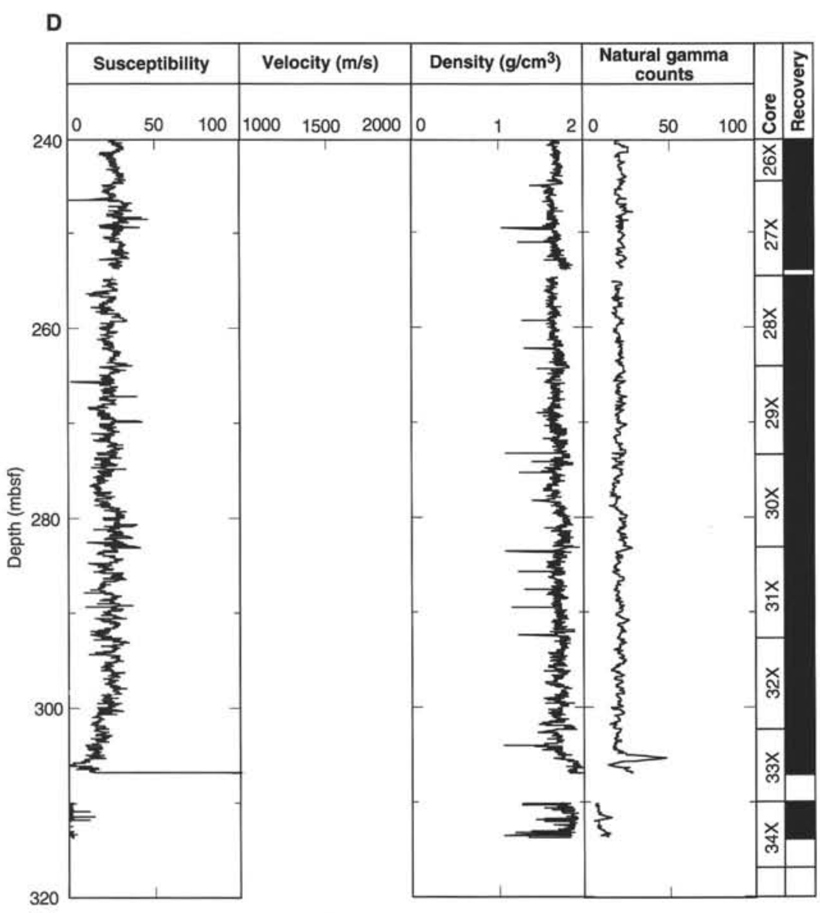

Figure 56 (continued).

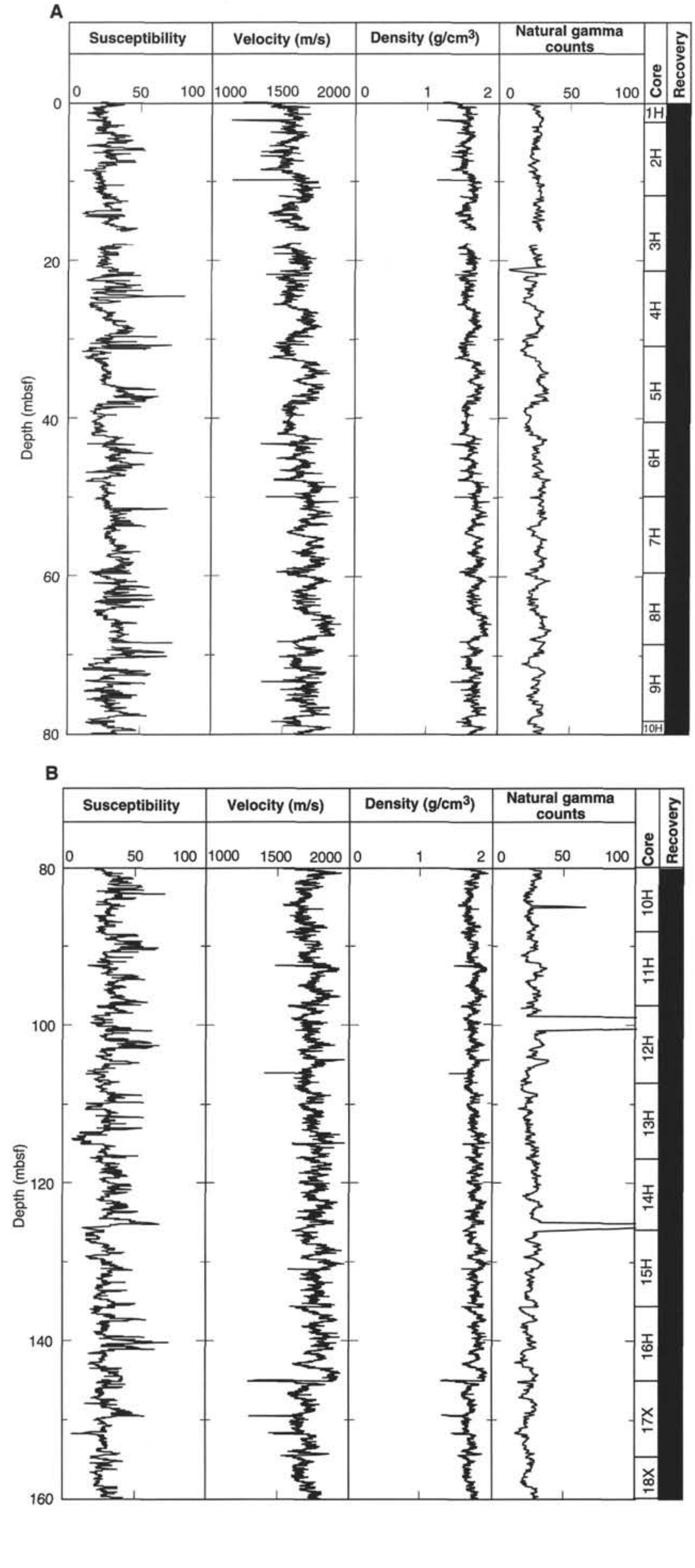

Figure 57. MST data (susceptibility, velocity, density, and natural gamma) for Hole 975C: (**A**) 0–80 mbsf, (**B**) 80–160 mbsf, (**C**) 160–240 mbsf, (**D**) 240–320 mbsf.

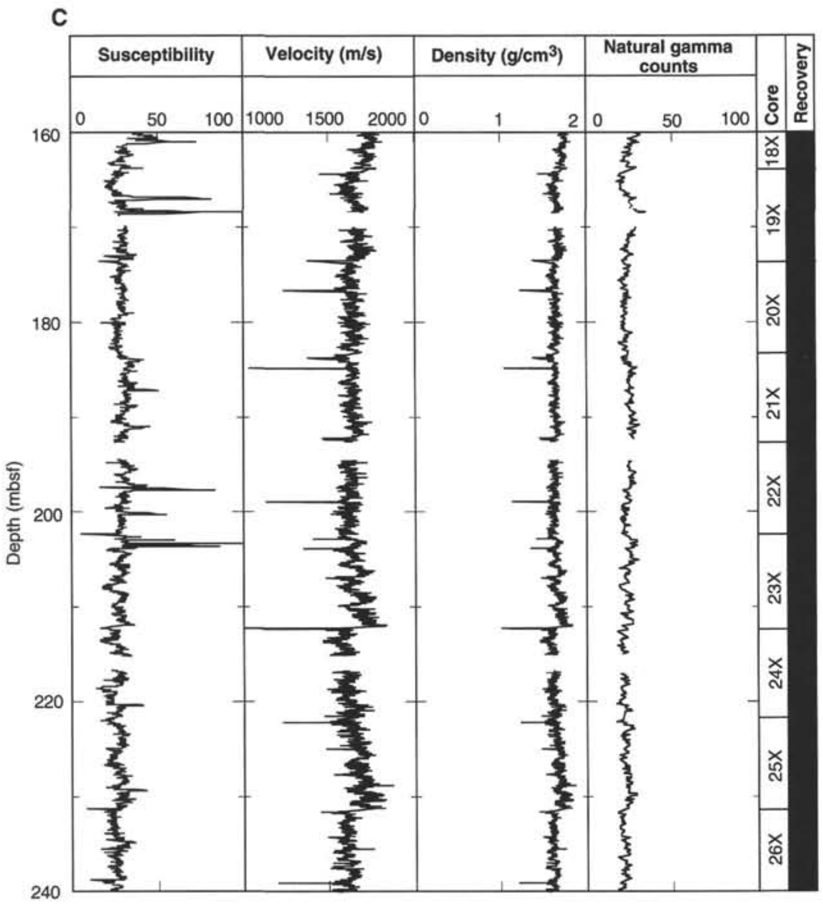

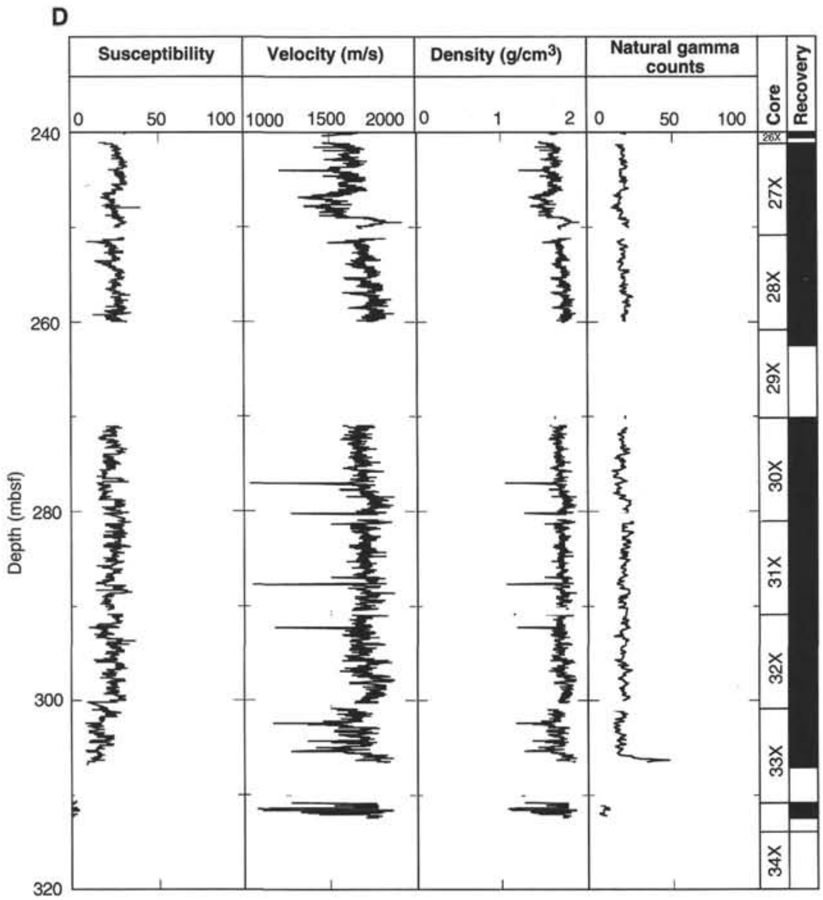

Figure 57 (continued).

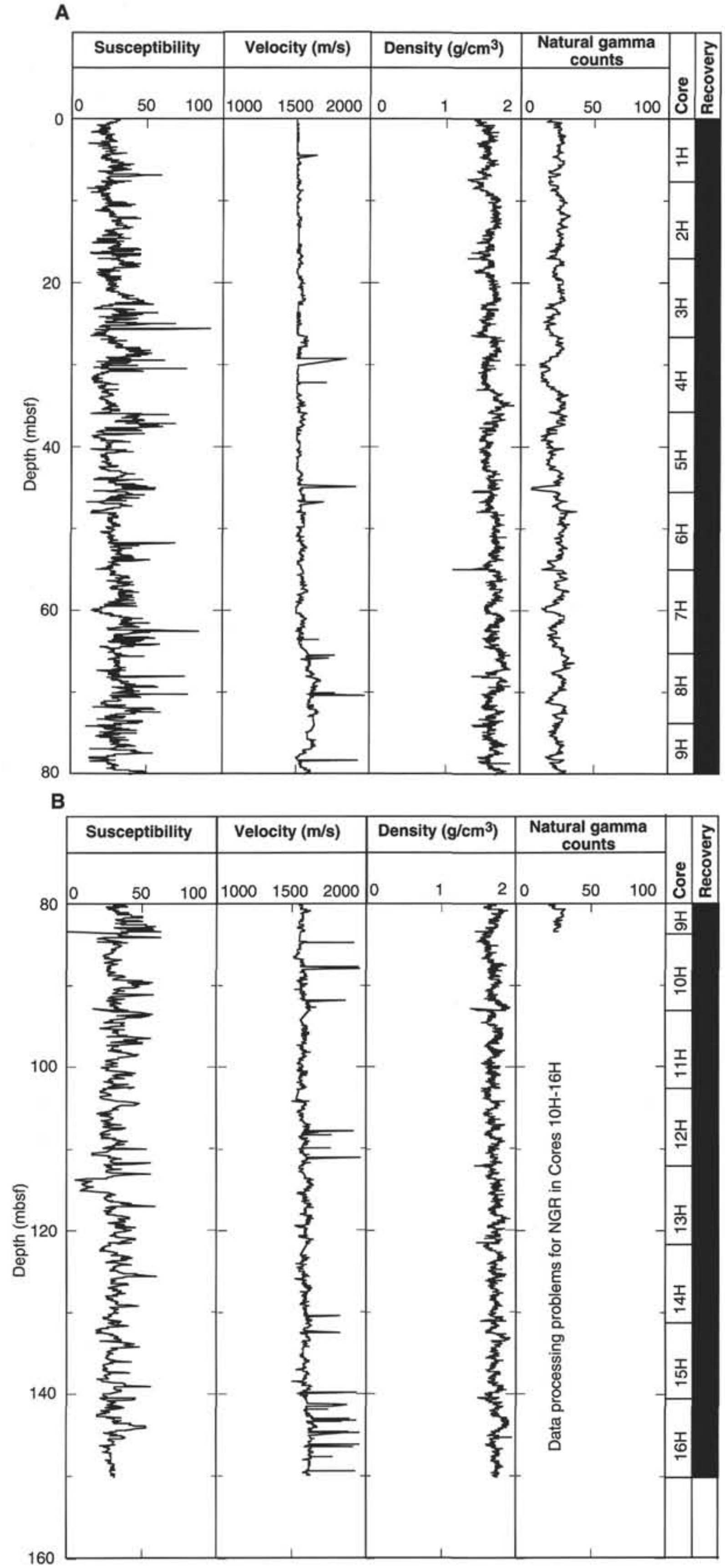

Figure 58. MST data (susceptibility, velocity, density, and natural gamma) for Hole 975D: (**A**) 0–80 mbsf, (**B**) 80–160 mbsf.

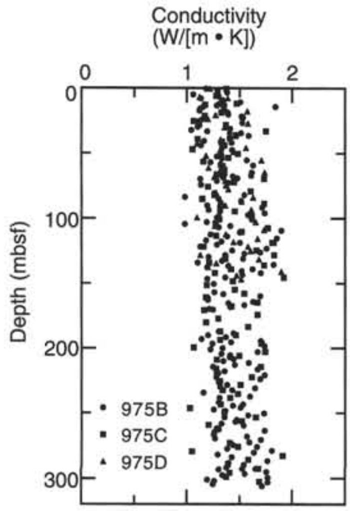

Figure 59. Thermal conductivity for Holes 975B, 975C, and 975D.

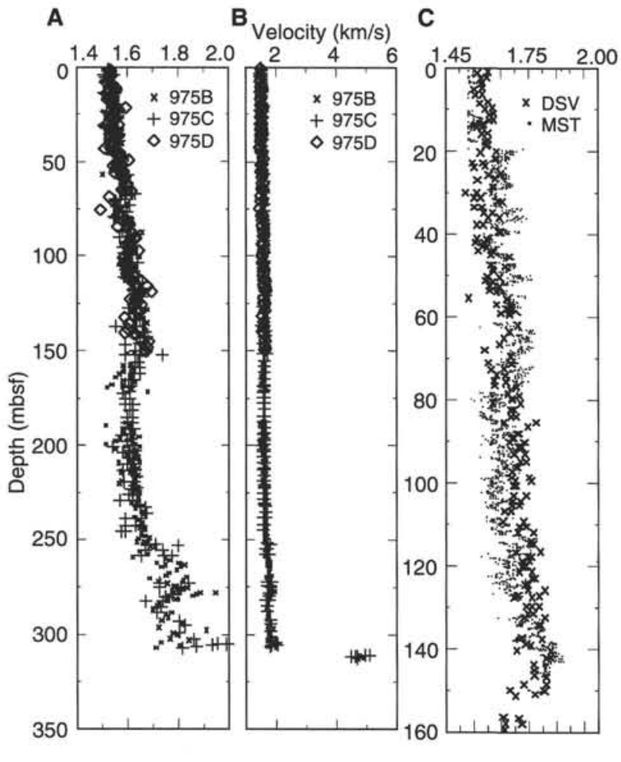

Figure 60. Seismic velocity for Holes 975B, 975C, and 975D. **A, B.** Same data shown, but B is at a smaller scale to show the magnitude of the velocity contrast between the sediments and the evaporites. **C.** Comparison between MST and DSV measurements in the upper cores. Note depth scale change.

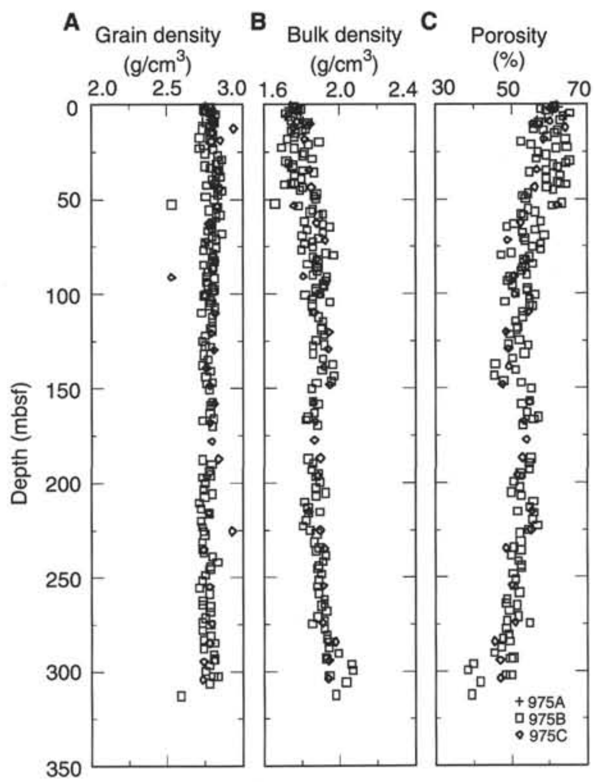

Figure 61. Index properties for Holes 975A, 975B, and 975C. **A.** Grain density. **B.** Bulk density. **C.** Porosity.

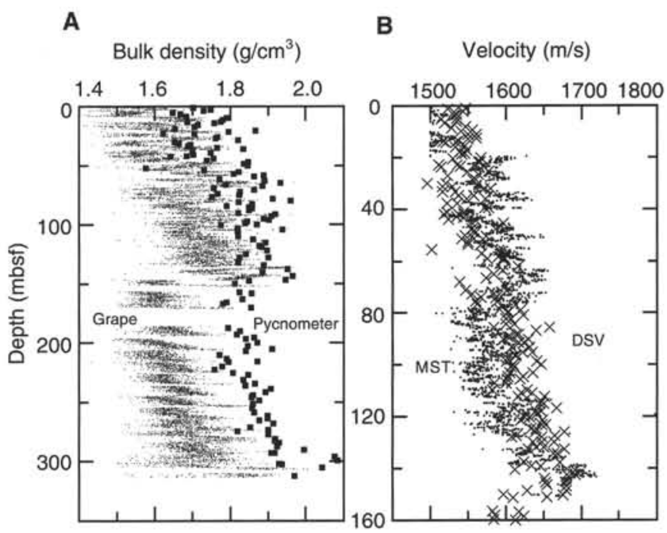

Figure 62. The effects of coring disturbances on MST and index properties measurements, Hole 975B. **A.** The increased offset in bulk densities caused by the switch to XCB coring at 150 mbsf. **B.** The gradual divergence of MST and DSV velocities with depth caused by stiffer sediments losing contact with the core liner walls.

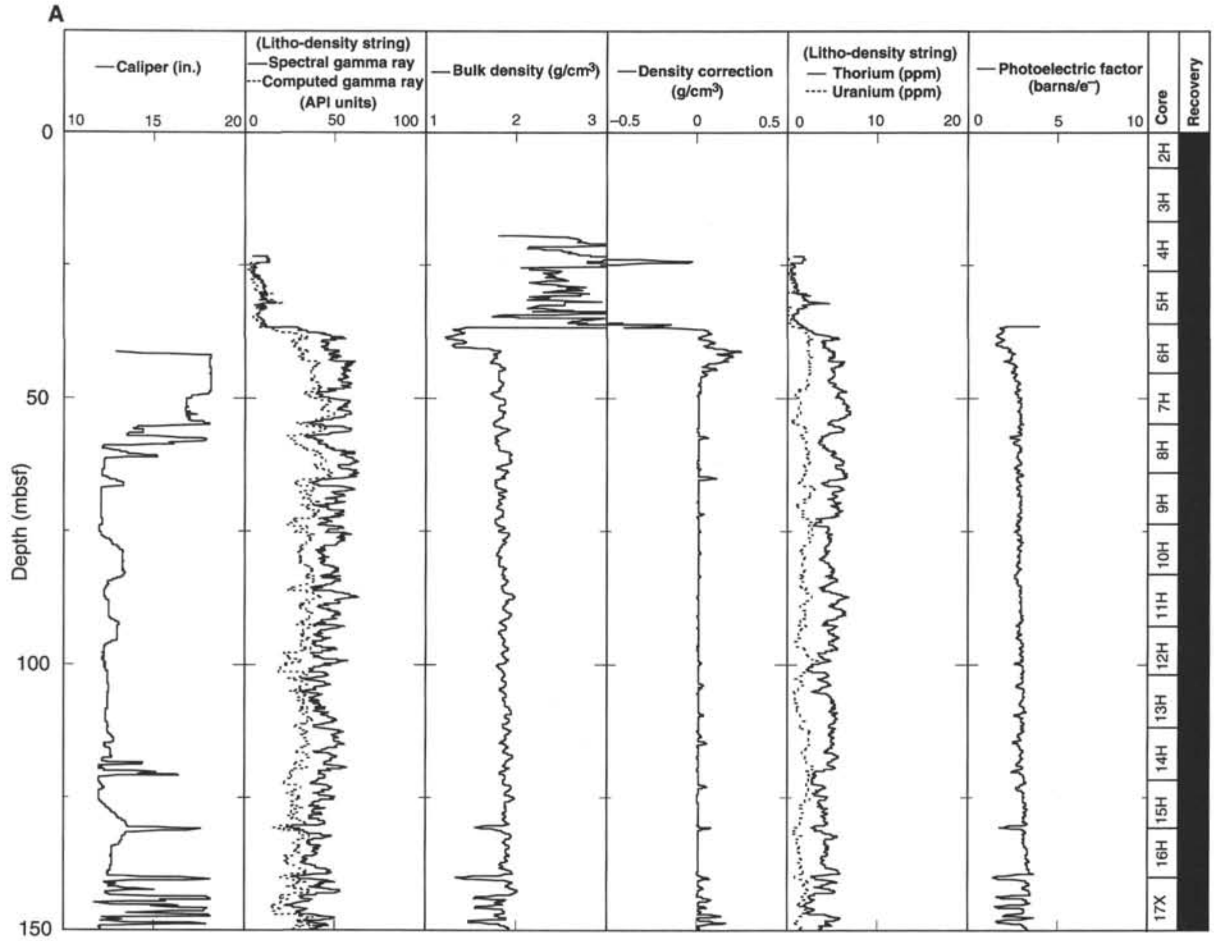

Figure 63. Quad combo tool results (**A**: 0–150 mbsf; **B**: 150–300 mbsf) and FMS (4-arms) calipers (**C**: 0–150 mbsf; **D**: 150–300 mbsf) for Hole 975C.

Table 18. Logged depth intervals for the three tool strings used in Hole 975C.

String	Run	Depth (mbsf)	Depth (mbrf)	Tools
Quad combo	Up 1	309.9–41.9	2736.0–2468.0	NGT/SDT/CNT-G/HLDT/DIT-E
	Up 2	213.9–91.9	2640.0–2518.0	NGT/SDT/CNT-G/HLDT/DIT-E
FMS	Up 1	296.3–44.1	2722.0–2470.2	NGT/FMS/GPIT
	Up 2	299.9–44.3	2726.0–2470.4	NGT/FMS/GPIT
GLT	Up 1	296.9–43.9	2723.0–2470.0	GSTA/ACTC/CNTG/NGTC/TCCB
	Up 2	242.6–124.9	2674.0–2551.0	GSTA/ACTC/CNTG/NGTC/TCCB

Note: mbsf = meters below seafloor, mbrf = meters below rig floor.

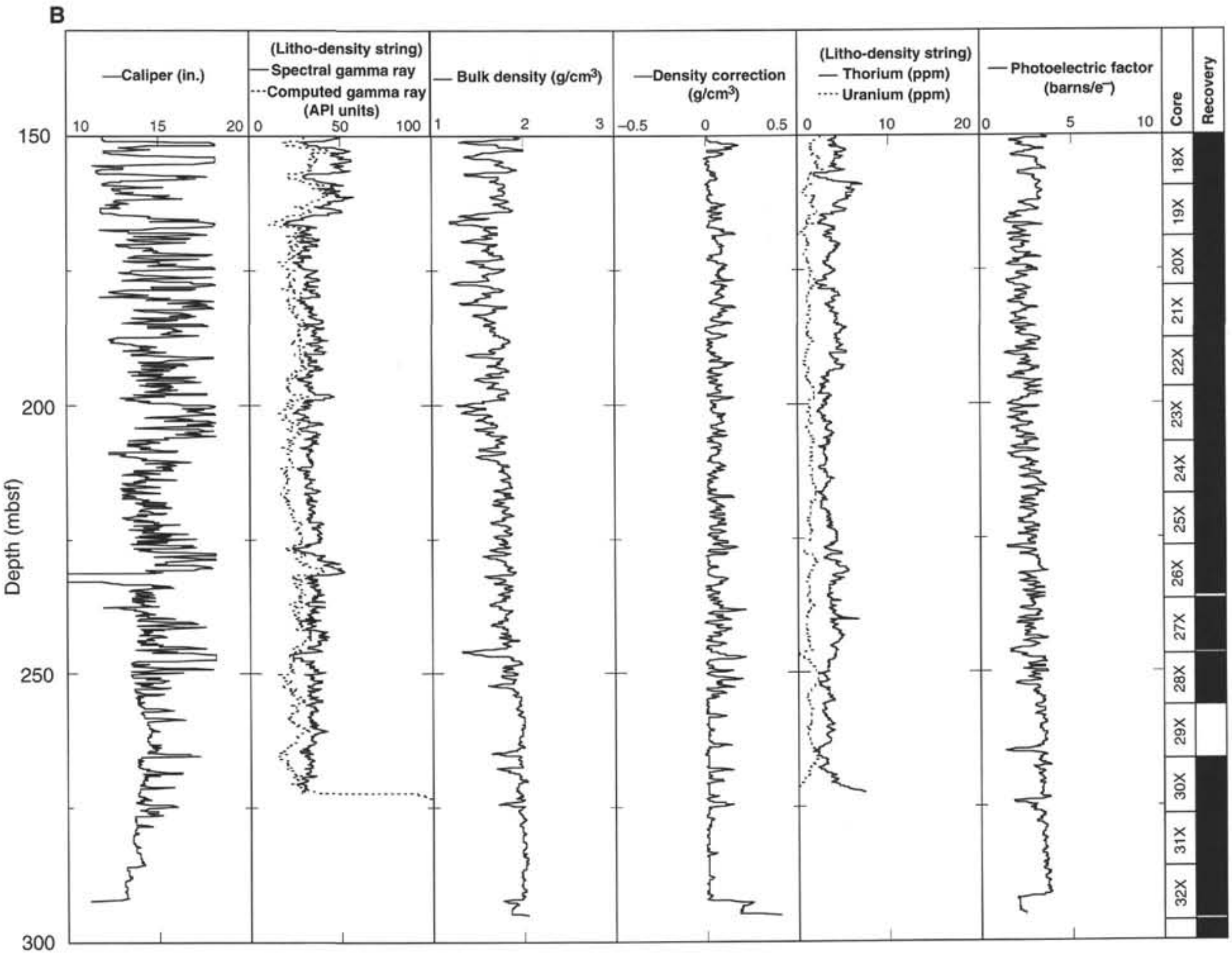

Figure 63 (continued).

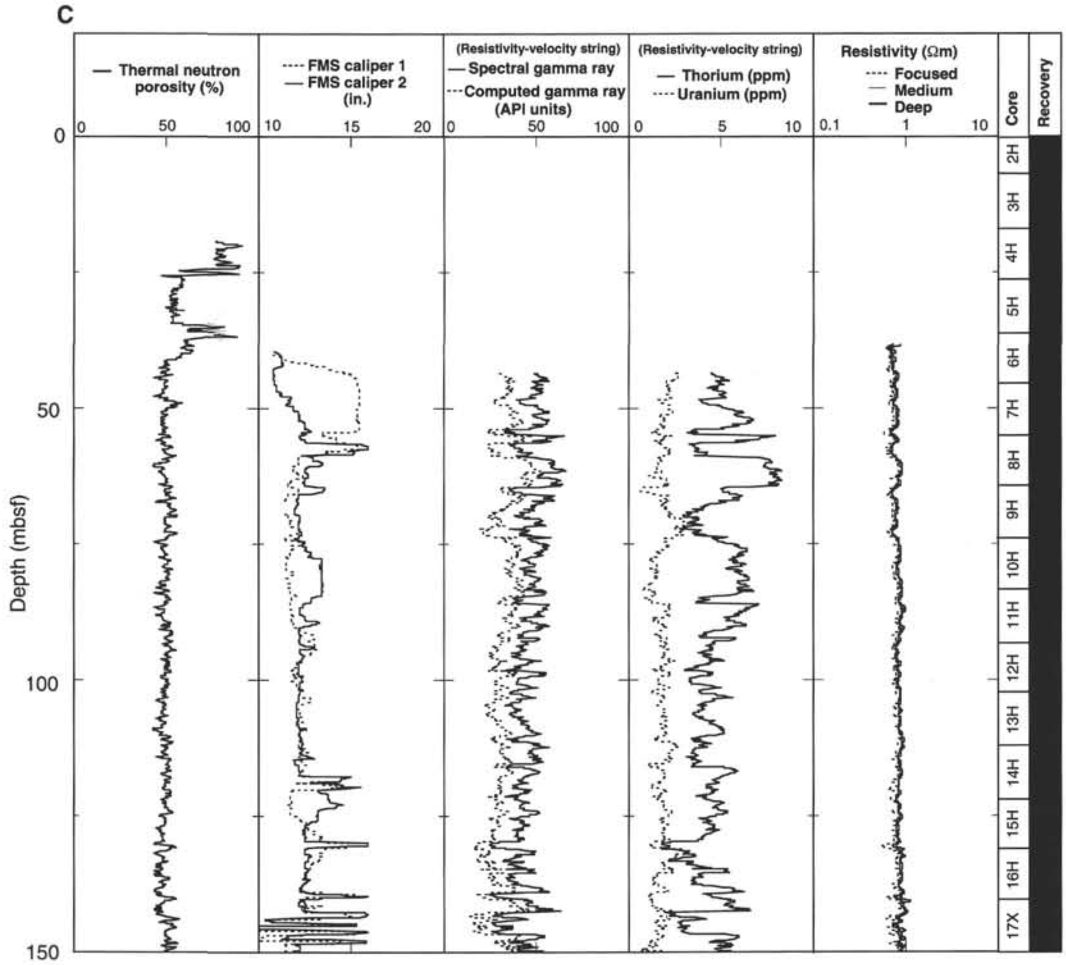

Figure 63 (continued).

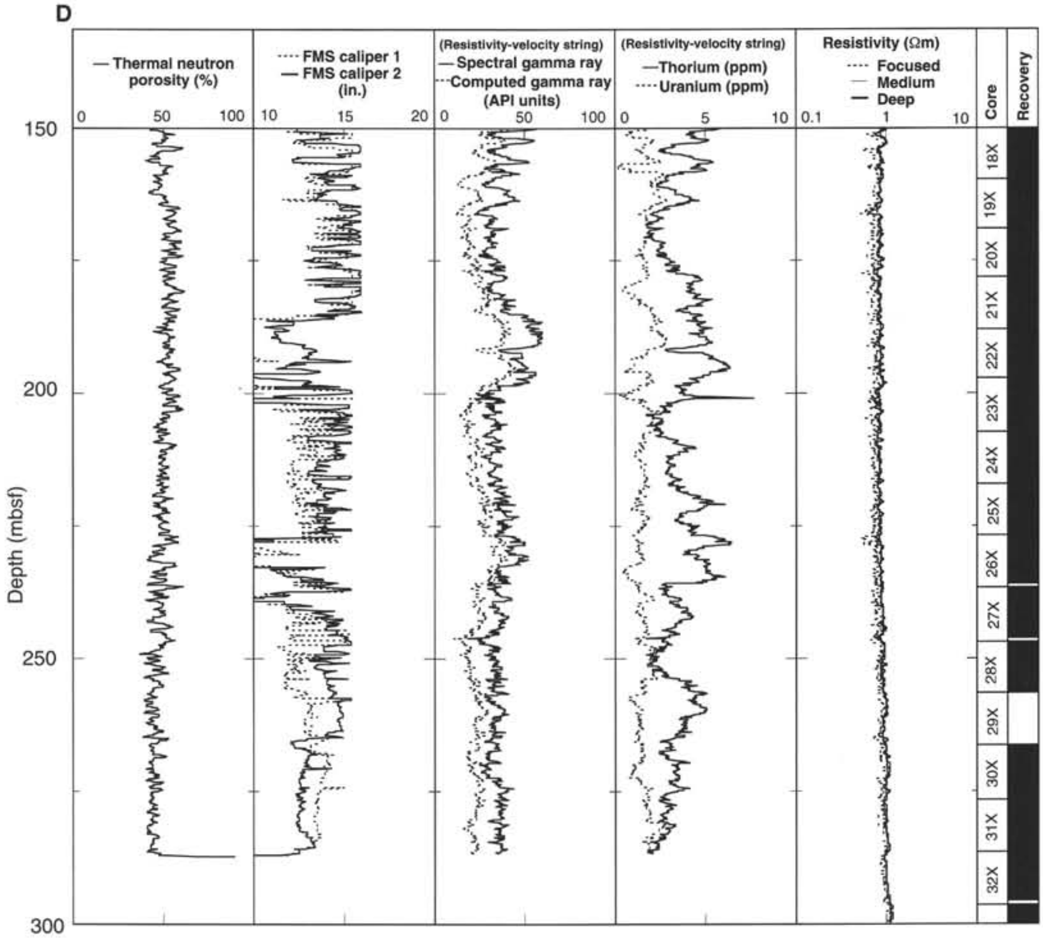

Figure 63 (continued).

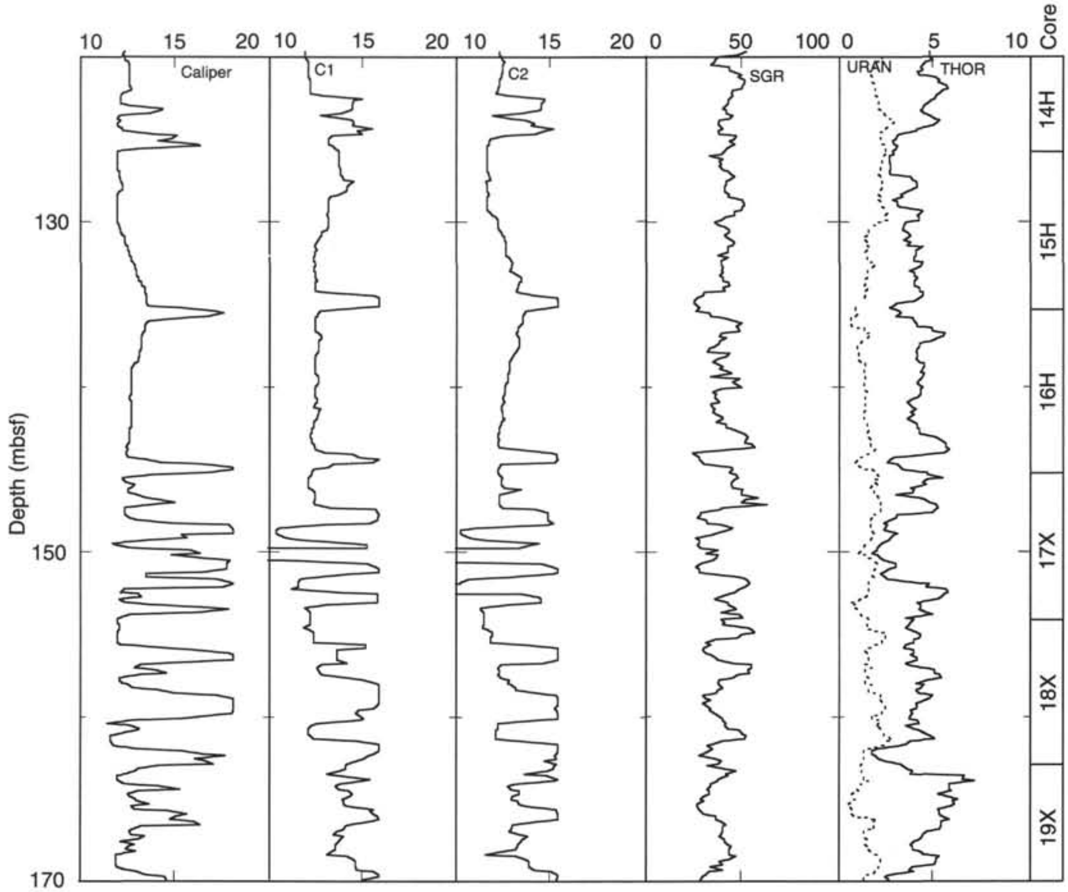

Figure 64. Correlation of cored intervals and log data in Hole 975C.

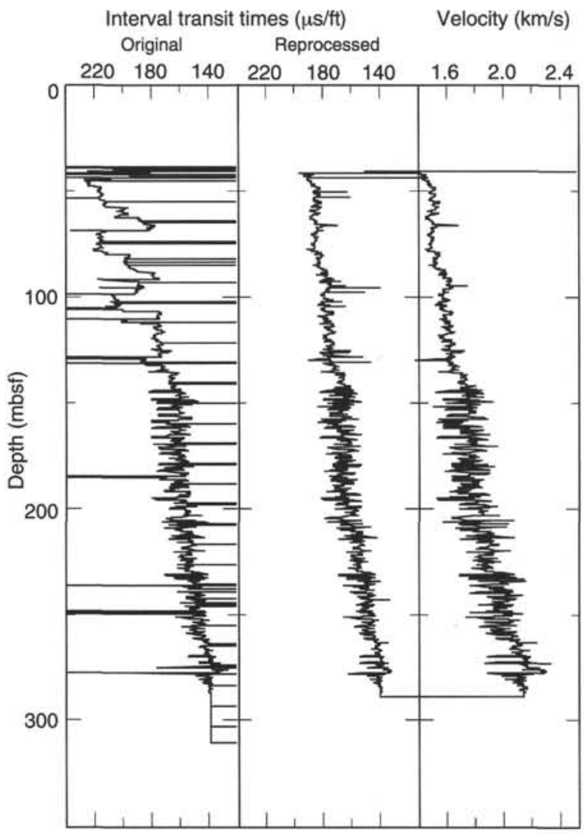

Figure 65. Sonic log results for Hole 975C. Interval transit times for raw data and reprocessed seismic velocity. Reprocessing of the real-time sonic logs significantly improves their value.

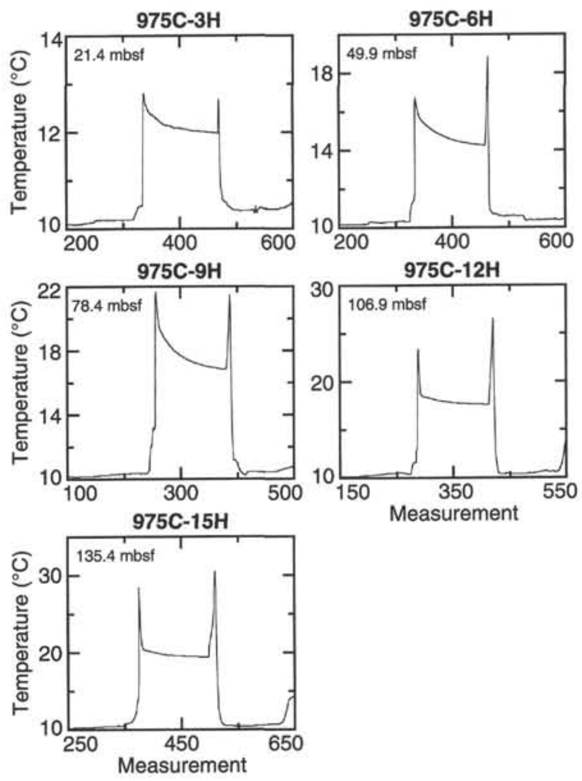

Figure 66. Temperature vs. time for the individual ADARA temperature tool runs at Hole 975C.

Table 19. Depths and equilibrium temperatures for the ADARA temperature tool runs at Hole 975C.

Depth (mbsf)	Temperature (°C)
21.4	11.771
49.9	13.089
78.4	15.376
106.9	16.876
135.4	18.810

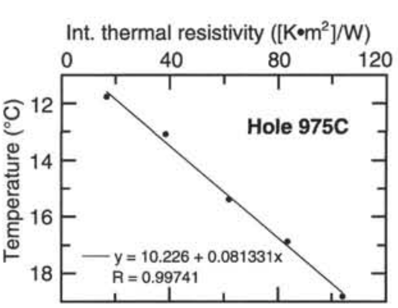

Figure 67. Temperature vs. integrated thermal resistivity for Hole 975C. The best-fitting linear regression to the data is shown by the straight line.

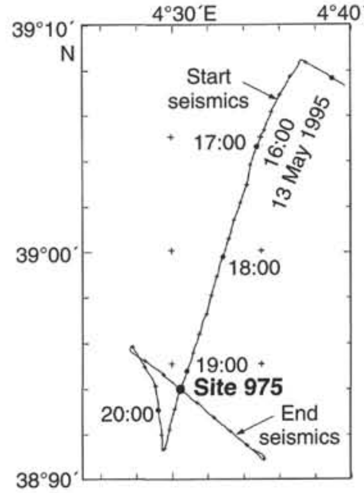

Figure 68. Ship track showing location of *JOIDES Resolution* single-channel seismic data collected over Site 975. These data are shown in Figure 69.

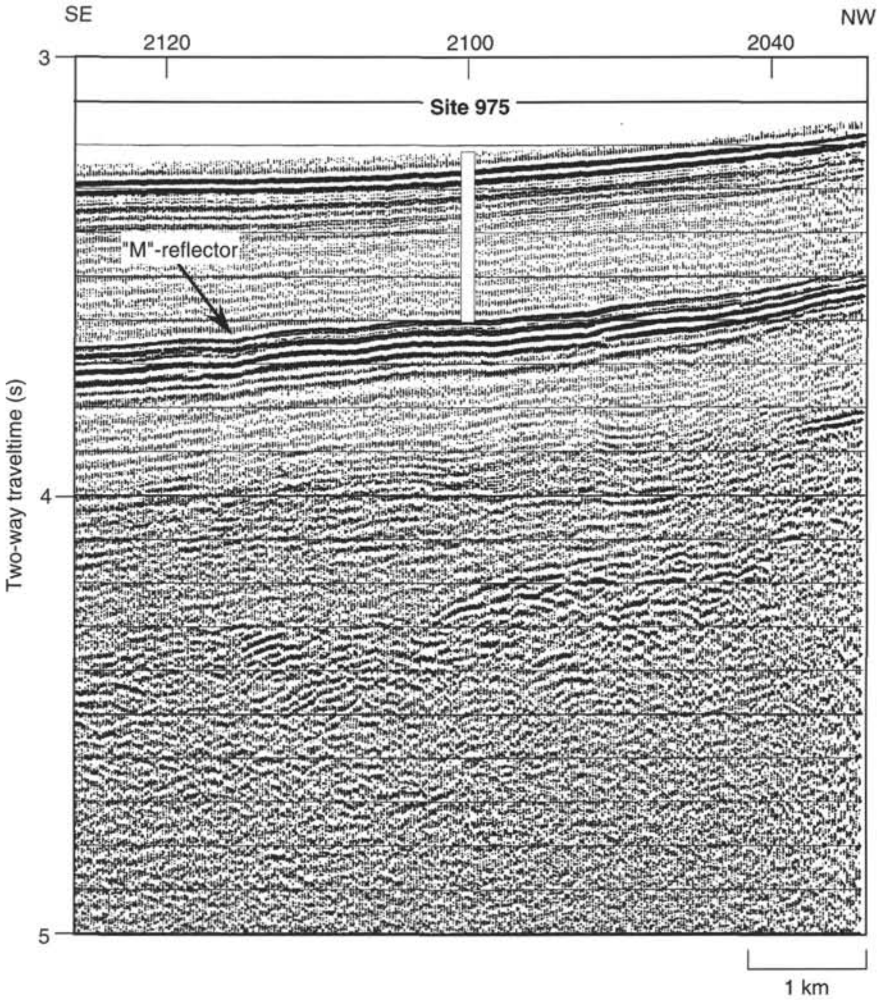

Figure 69. Northwest-southeast single-channel seismic profile across Site 975. The location of this profile is shown in Figure 68.

Table 20. Two-way traveltime to boundaries of seismic facies observed in the single-channel seismic data shown in Figures 3 and 69.

Seismic facies description	Seismic facies interval two-way traveltime below seafloor (s)	Seismic facies interval two-way traveltime from sea surface (s)
Parallel, continuous, high to moderate amplitude	0 to 0.13	3.26 to 3.39
Subparallel, discontinuous, low amplitude	0.13 to 0.34	3.39 to 3.60
Subparallel, continuous, high amplitude	0.34 to 0.47	3.60 to 3.73
Subparallel, discontinuous, low amplitude	0.47 to ~0.64	3.73 to 3.90
Discontinuous, subparallel/undulating to chaotic, variable amplitude	~0.64 to ~0.92/1.0	~3.90 to ~4.18/4.26
Discontinuous, chaotic to hyperbolic, high amplitude	> ~0.92/1.0	> ~4.18/4.26

Note: Two-way traveltimes to 100, 200, and 308 mbsf are calculated using laboratory velocities (see "Physical Properties" section, this chapter).

Table 21. Two-way traveltime to several sub-seafloor depths calculated using shipboard laboratory velocity determinations.*

Depth interval (mbsf)	Average velocity in interval (m/s)	Calculated two-way traveltime in interval (s)	Calculated cumulative two-way traveltime below seafloor to bottom of interval (s)	Calculated cumulative two-way traveltime to bottom of interval (s)
0 to 100	1567	0.128	0.128	3.388
100 to 200	1623	0.123	0.251	3.511
200 to 308	1697	0.118	0.369	3.629

Note: *see "Physical Properties" section, this chapter.

SHORE-BASED LOG PROCESSING

Hole 975C

Bottom felt: 2426.1 mbrf (used for depth shift to seafloor)
Total penetration: 313.7 mbsf
Total core recovered: 307.66 m (98.1%)

Logging Runs

Logging String 1: DIT/SDT/HLDT/CNTG/NGT
Logging String 2: FMS/GPIT/NGT
Logging String 3: ACT/GST/NGT
Wireline heave compensator was used to counter ship heave.

Bottom-Hole Assembly

The following bottom-hole assembly depths are as they appear on the logs after differential depth shift (see "Depth shift" section) and depth shift to the seafloor. As such, there might be a discrepancy with the original depths given by the drillers onboard. Possible reasons for depth discrepancies are ship heave, use of wireline heave compensator, and drill string and/or wireline stretch.

DIT/SDT/HLDT/CNTG/NGT: Bottom-hole assembly at ~41.5 mbsf.

FMS/GPIT/NGT: Did not reach the bottom-hole assembly.

ACT/GST/NGT: Bottom-hole assembly at ~45 mbsf.

Processing

Depth shift: Reference run for depth shift: DIT/SDT/HLDT/CNTG/NGT. All original logs have been interactively depth shifted with reference to NGT from DIT/SDT/HLDT/CNTG/NGT and to the sea floor (–2426.1 m).

Gamma-ray processing: NGT data have been processed to correct for borehole size and type of drilling fluid.

Acoustic data processing: The array sonic tool was operated in two modes: linear array mode, with the 8 receivers providing full waveform analysis (compressional and shear) and standard depth-derived borehole compensated mode, including long-spacing (8-10-10-12 ft) and short-spacing (3-5-5-7 ft) logs. The long-spacing logs have been processed in order to eliminate some of the noise and cycle skipping experienced during the recording.

Geochemical processing: (For detailed explanation of the processing please refer to the "Explanatory Notes" chapter, this volume, or to the geochem.doc file on the CD-ROM, back pocket, this volume). The elemental yields recorded by the GST tool represent the relative contribution of only some of the rock-forming elements (iron, calcium, chlorine, silica, sulfur, hydrogen, gadolinium, and titanium—the last two were computed during geochemical processing) to the total spectrum. Because other rock-forming elements are present in the formation (such as aluminum, potassium, etc.), caution is recommended in using the yields to infer lithologic changes. Instead, ratios (see acronyms.doc on CD-ROM) are more appropriate to determine changes in the macroscopic properties of the formation. A list of oxide factors used in geochemical processing includes the following:

SiO_2 = 2.139
$CaCO_3$ = 2.497
FeO* = 1.358
TiO_2 = 1.668
K_2O = 1.205
Al_2O_3 = 1.889

FeO* = computed using an oxide factor which assumes a 50:50 combination of Fe_2O_3 and FeO factors. The results of the processing are presented along with the calcium carbonate measurements performed on board.

Quality Control

Data recorded through bottom-hole assembly, such as the gamma ray and neutron porosity data above 41.5 mbsf, should be used qualitatively only because of the attenuation on the incoming signal.

Hole diameter was recorded by the hydraulic caliper on the HLDT tool (CALI) and the caliper on the FMS string (C1 and C2).

FACT = *quality control curve in geochemical processing*. Accuracy of the estimates is inversely proportional to the magnitude of the curve.

Note: Details of standard shore-based processing procedures are found in the "Explanatory Notes" chapter, this volume. For further information about the logs, please contact:

Cristina Broglia
Phone: 914-365-8343
Fax: 914-365-3182
E-mail: chris@ldeo.columbia.edu

Elizabeth Pratson
Phone: 914-365-8313
Fax: 914-365-3182
E-mail: beth@ldeo.columbia.edu

Hole 975C: Natural Gamma Ray-Resistivity-Sonic Logging Data

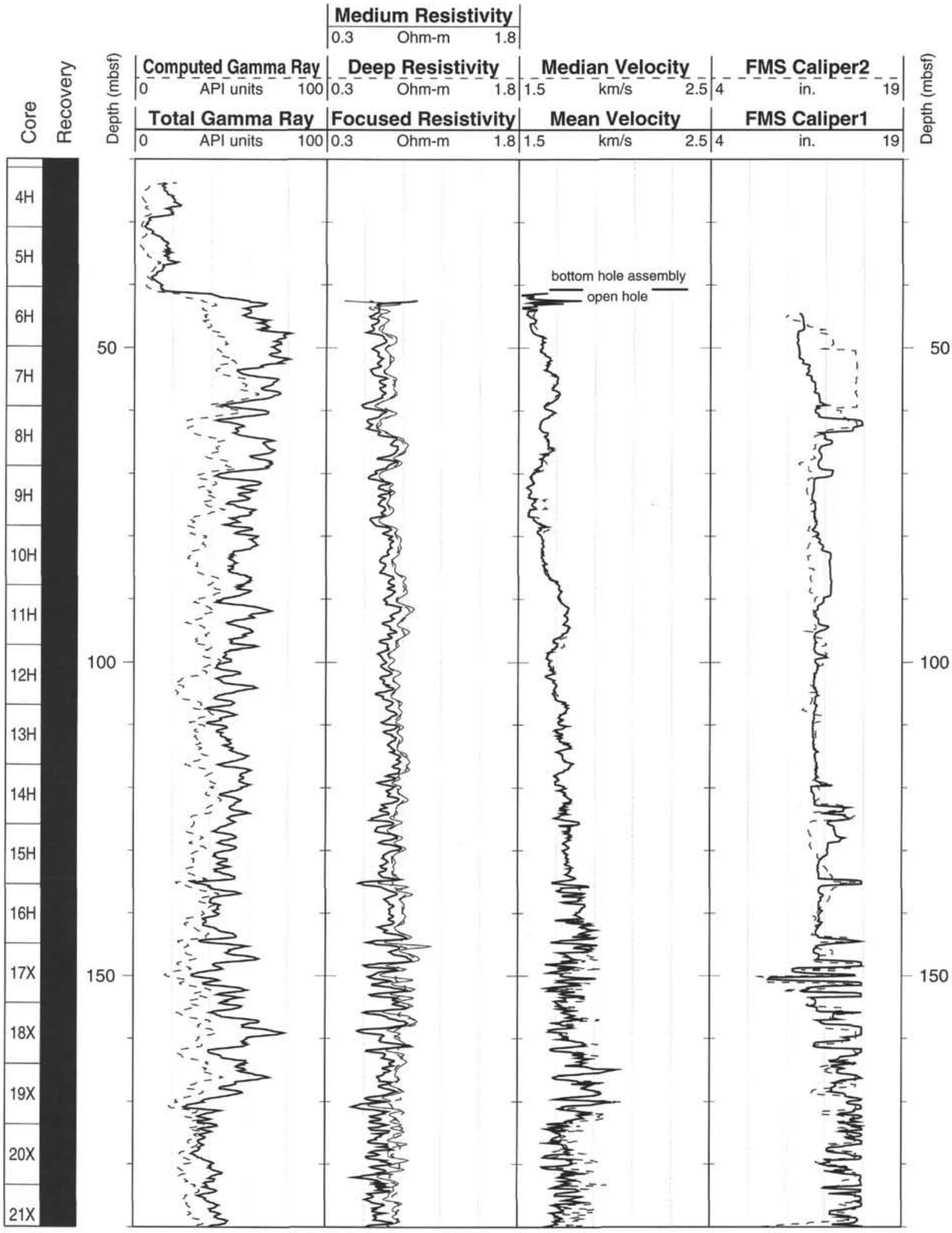

Hole 975C: Natural Gamma Ray-Resistivity-Sonic Logging Data (cont.)

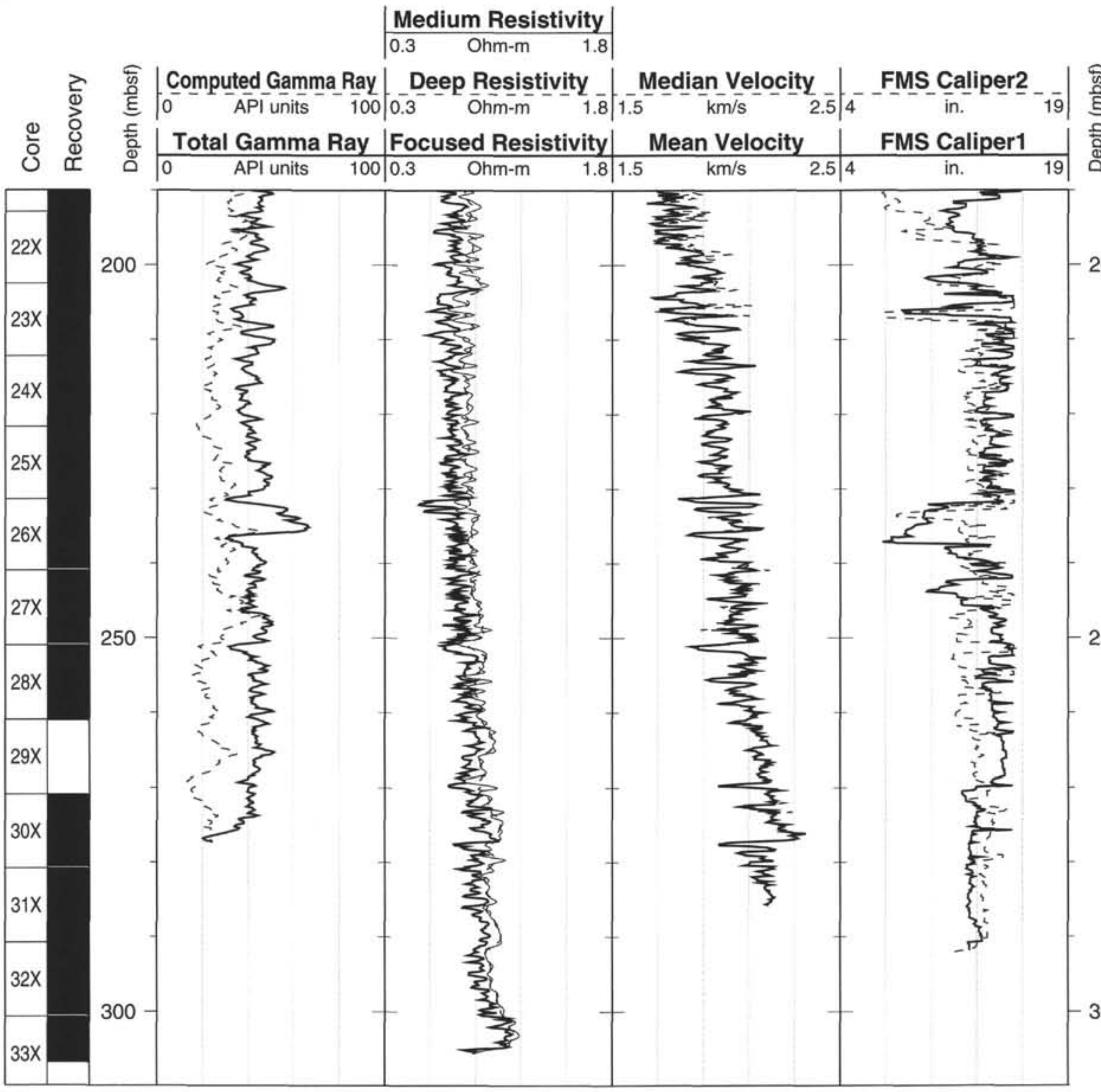

Hole 975C: Natural Gamma Ray-Density-Porosity Logging Data

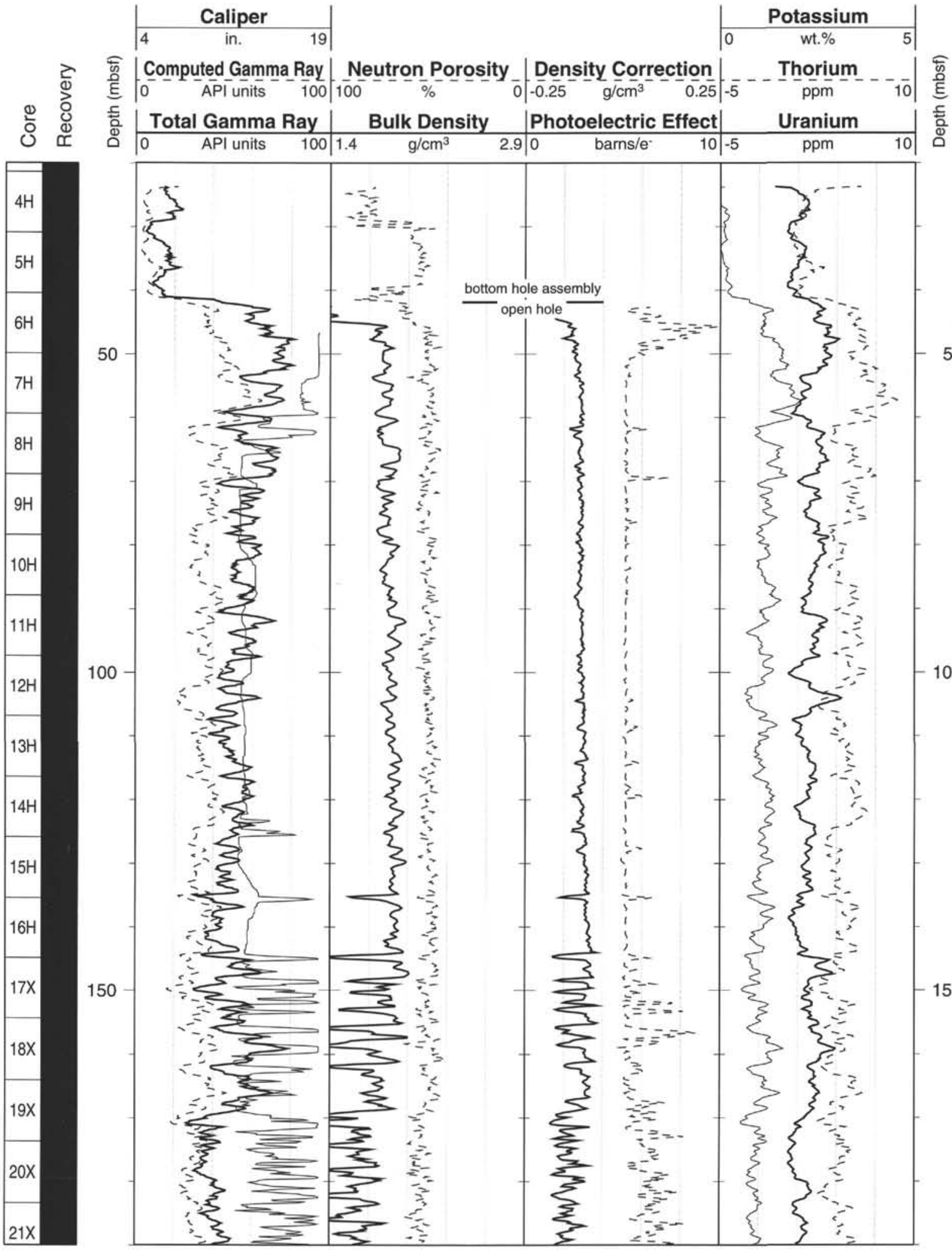

Hole 975C: Natural Gamma Ray-Density-Porosity Logging Data (cont.)

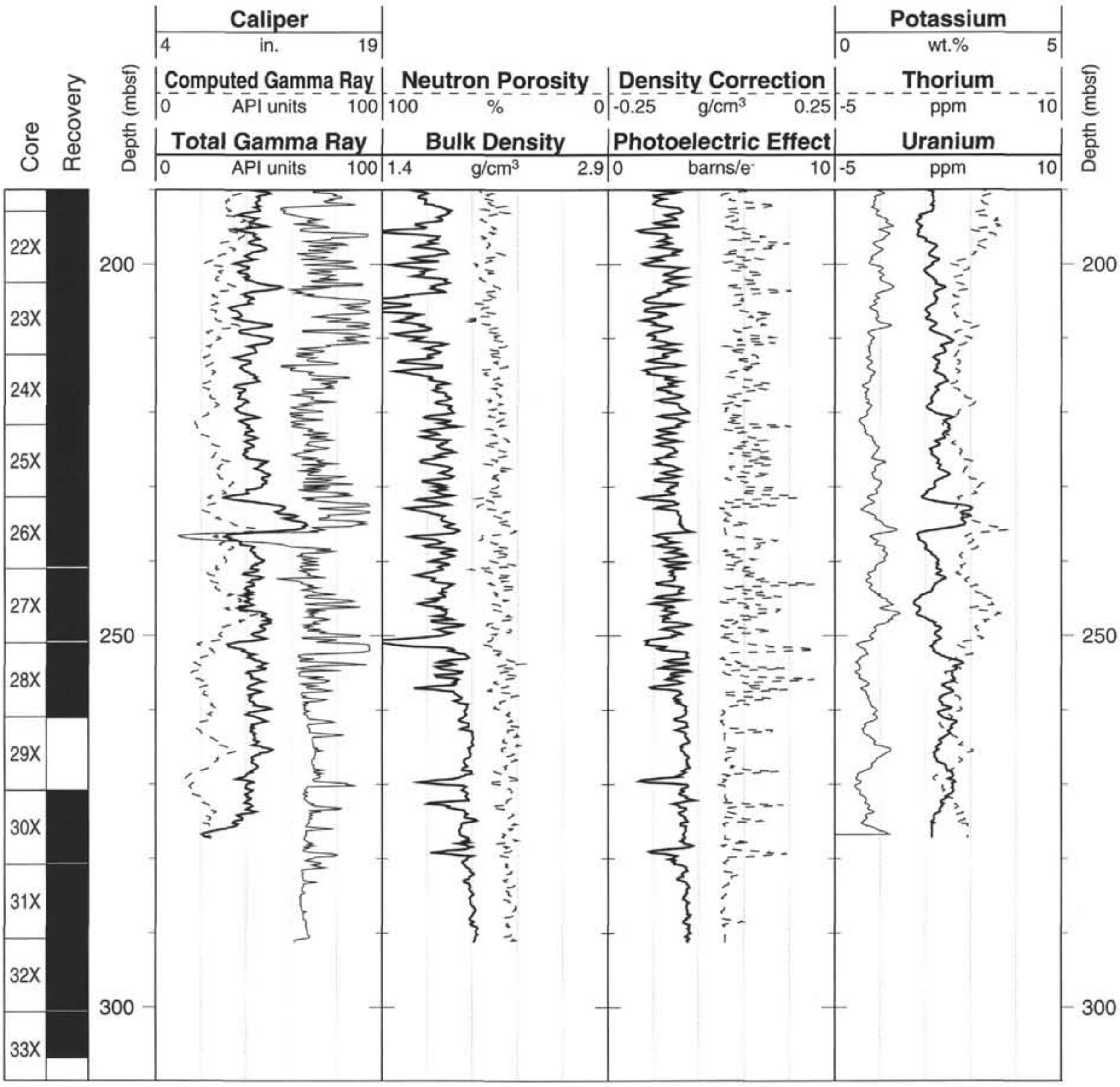

Hole 975C: Natural Gamma Ray Logging Data

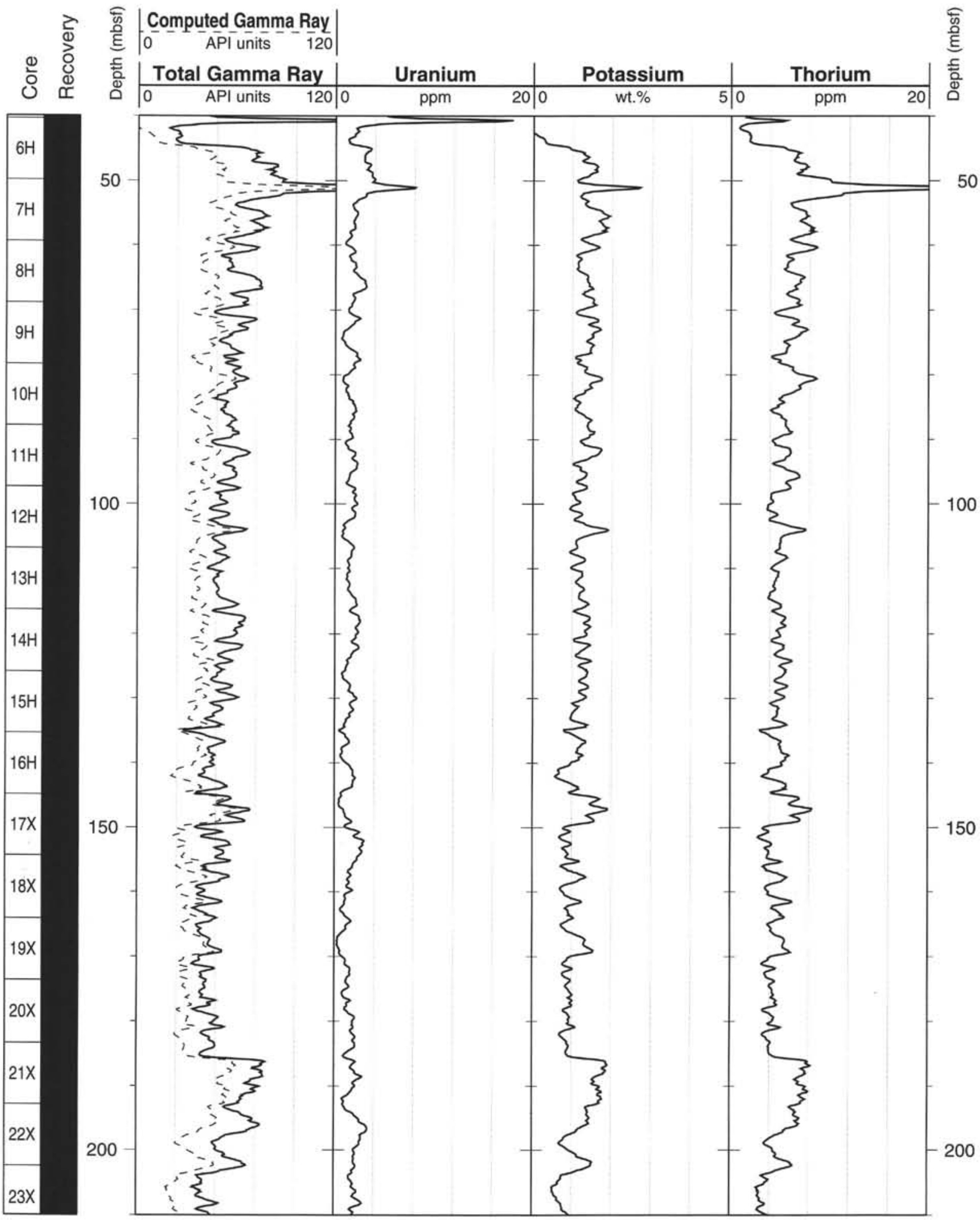

Hole 975C: Natural Gamma Ray Logging Data (cont.)

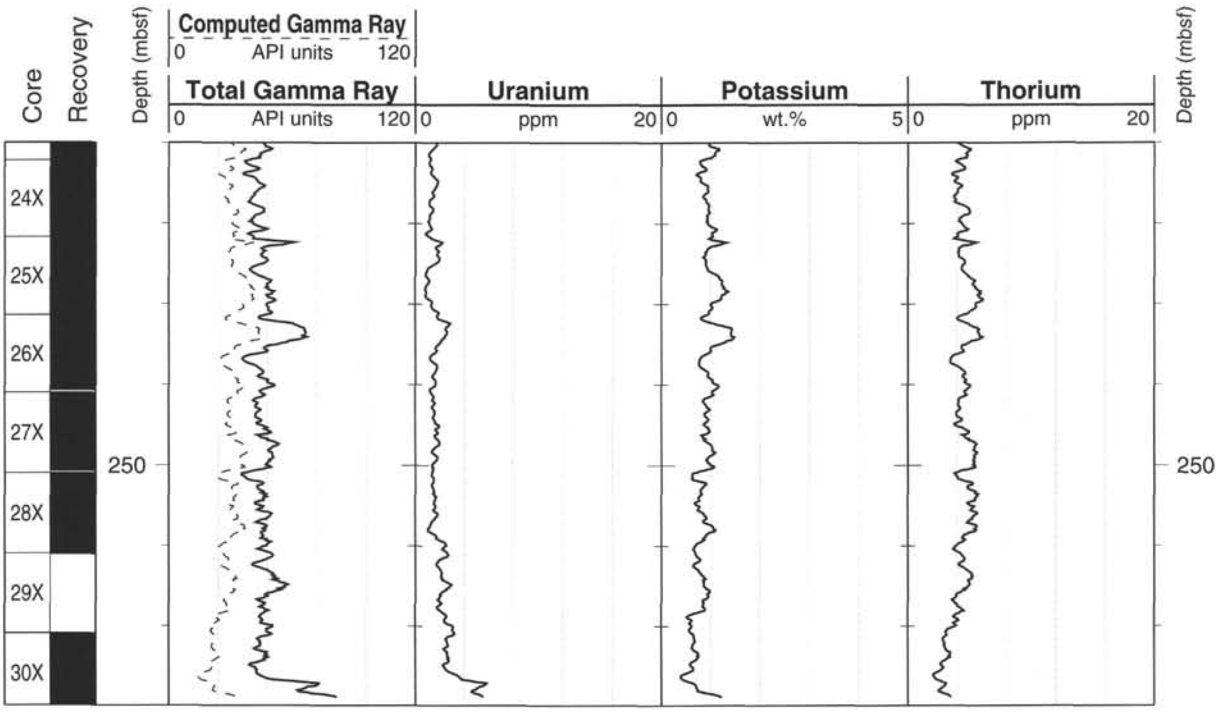

Hole 975C: Geochemical Logging Data

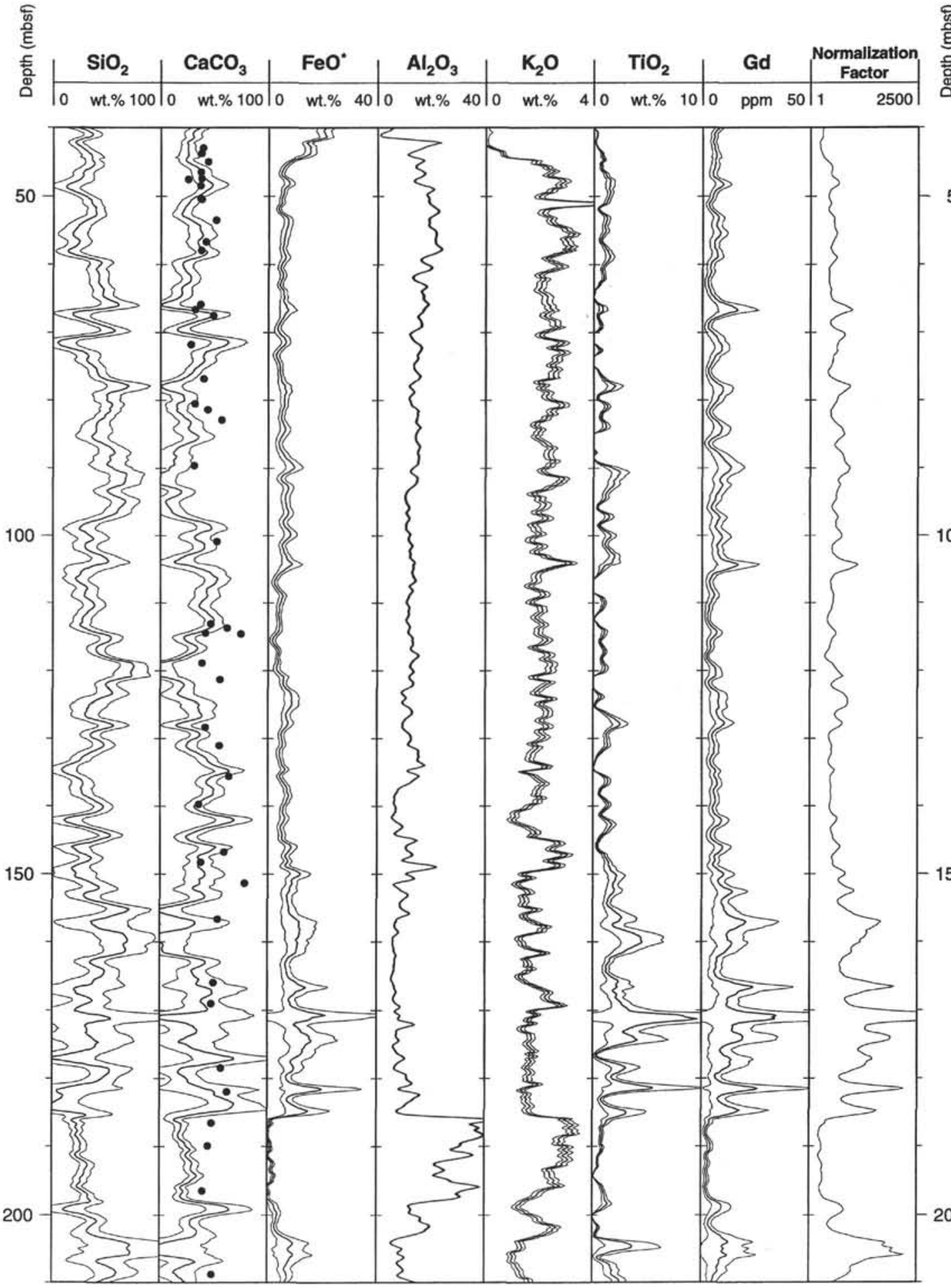

Hole 975C: Geochemical Logging Data (cont.)